University of New Mexico
UNM Digital Repository

Biomedical Sciences ETDs | Electronic Theses and Dissertations

5-1-2012

Multifunctional iron platinum stealth immunomicelles : targeted imaging and therapy of prostate cancer.

Robert Taylor

Follow this and additional works at: https://digitalrepository.unm.edu/biom_etds

 Part of the Medicine and Health Sciences Commons

Recommended Citation
Taylor, Robert. "Multifunctional iron platinum stealth immunomicelles : targeted imaging and therapy of prostate cancer.." (2012).
https://digitalrepository.unm.edu/biom_etds/58

This Dissertation is brought to you for free and open access by the Electronic Theses and Dissertations at UNM Digital Repository. It has been accepted for inclusion in Biomedical Sciences ETDs by an authorized administrator of UNM Digital Repository. For more information, please contact disc@unm.edu.

www.manaraa.com

Robert M. Taylor
Candidate

Biomedical Sciences
Department

This dissertation is approved, and it is acceptable in quality and form for publication:

Approved by the Dissertation Committee:

Dr. Laurel O. Sillerud , Chairperson

Dr. Marco Bisoffi

Dr. Todd Thompson

Dr. William Anderson

www.manaraa.com

MULTIFUNCTIONAL IRON PLATINUM STEALTH IMMUNOMICELLES: TARGETED IMAGING AND THERAPY OF PROSTATE CANCER

by

ROBERT M. TAYLOR

B.A. Biochemistry, University of New Mexico, 2007

DISSERTATION

Submitted in Partial Fulfillment of the
Requirements for the Degree of

Doctor of Philosophy

Biomedical Sciences

The University of New Mexico
Albuquerque, New Mexico

May 2012

www.manaraa.com

DEDICATION

I dedicate my dissertation to my supportive family and friends. A special feeling of gratitude to my loving mother, Kathryn Taylor whose words of encouragement and push for tenacity have always rang in my ears. My sister, Laura, and my brothers, Andrew and Lee, have never left my side and are very special. Additionally, I dedicate this work to my grandmother and grandfather, Curt and Chris, who taught me patience, strength, honesty, compassion, persistence, and resolve; each an important quality in achieving my goals over the past decade. I also dedicate my research to my father, Randy Taylor, who lost a long battle with colorectal cancer in 2010. As I move through the next stages of my research, working to reduce death and suffering form cancer, I will always remember the obstacles my father faced in his battle and work to find solutions to these obstacles, keeping the patient's needs always in mind and always holding true to my convictions. Importantly, I dedicate this work to my children, Abigail and Ryne, who provided me with the day-to-day strength to push forward to make the world a better place for them to live in. Each day that I worked to see this research to fruition was well worth it, knowing that each day I would come home to their smiling faces and that I was working towards providing them with better lives. Last, but not least, I dedicate my dissertation research to my friends, too many to name here, who have stood by me over the years and given me the strength to press on. I thank each of you from the depths of my heart.

www.manaraa.com

ACKNOWLEDGMENTS

I foremost acknowledge Dr. Laurel Sillerud, my advisor, dissertation chair, and confidant for always encouraging me, trusting me, and pressing me to find the important questions and answers for myself. Not only has Dr. Sillerud given me the skills to be an expert teacher and scientist, but he has also instilled in me the importance of conviction, patience, persistence, and resolve. Through all of my professional and personal strife, Laurel has become a confidant in whom I owe great respect and appreciation.

I thank my committee members for their valuable recommendations pertaining to this study and assistance in my professional development. First, I thank Dr. Marco Bisoffi for his co-mentoring role in my education, for always having an open door, and for his persistent encouragement. I thank Dr. Thompson for always asking the difficult questions and remaining critical, as this has played a huge role in helping me to develop into an independent scientist. I also thank Dr. Anderson, who has been part of my education since my undergraduate days in the department. Dr. Anderson's wisdom, years of experience, and open ear have been a tremendous encouragement to me over the years. I truly appreciate what I have gained from each of you.

I would also like to acknowledge my scientific roots. I thank Dr. Arnold Crelier, who taught my first general chemistry course and ignited my curiosity and passion for science. Additionally, I thank Dr. John Engen for my first undergraduate laboratory experiences; a solid foundation has served me well.

www.manaraa.com

Multifunctional iron platinum stealth immunomicelles: Targeted imaging and therapy of prostate cancer.

By

Robert M. Taylor

B.A. Biochemistry, University of New Mexico, 2007

Doctor of Philosophy, Biomedical Sciences, University of New Mexico, 2012

Abstract

In the United States, prostate cancer is the second most common reason for cancer death in men. No imaging methods currently exist which are specific for detecting, imaging, and treating extracapsular or metastatic prostate cancer. The goal of this research was to develop novel nanoparticles that would specifically target human prostate cancer cells and simultaneously deliver a chemotherapeutic agent and superior magnetic resonance imaging (MRI) contrast agent to the prostate cancer cells for both therapy and MRI detection. This dissertation describes the synthesis and comprehensive characterization of superparamagnetic iron-platinum nanoparticles (SIPPs) and their subsequent encapsulation with the drug Paclitaxel, using a mixture of functionalized phospholipids, to create SIPP and Paclitaxel-loaded micelles (SPMs) conjugated to an antibody against prostate specific membrane antigen (PSMA), which is specifically over-expressed in human prostate cancer cells and tumors. Taken together the data suggest that SPMs specifically target human prostate cancer cells, are superior contrast agents in T_2-weighted MRI, and prevent prostate tumor growth in a PSMA-dependent manner.

www.manaraa.com

Table of Contents

www.manaraa.com

www.manaraa.com

List of figures

www.manaraa.com

www.manaraa.com

List of Tables

www.manaraa.com

Chapter 1

Introduction

Prostate Cancer

Prostate cancer is the most common non-skin cancer and the second leading cause of cancer death in men in the United States (1). Prominent, unresolved problems with the clinical management of prostate cancer include the lack of highly specific detection methods and efficient therapeutic interventions. Serum prostate specific antigen (PSA) measurements are widely used to infer the presence of disease, yet elevated PSA concentrations can also result from benign prostatic hyperplasia (BPH) suggesting that these measurements lack specificity (2). Elevated serum PSA concentrations are often followed by invasive biopsies in an attempt to discover, grade and stage prostate cancer, however, the results from the European Randomized Study of Screening for Prostate Cancer showed that 75% of PSA-driven biopsies are negative (3,4). These results are congruent with previous studies that reported false-negative biopsy rates of 30-50% in patients with subsequently-confirmed small and inconspicuous malignant lesions (5). Twenty to forty percent of patients initially responding to treatment by androgen ablation, prostatectomy or radiation, relapse and ultimately progress to castration resistant disease (6). After relapse, subsequent chemotherapeutic options are limited, inefficient, and plagued by side effects due to lack of specificity (7). Even patients treated by surgical resection, with clean margins, of organ-confined prostate cancer carry a 25 %

www.manaraa.com

lifetime risk of mortality from metastases, while 40 % of the surgically-resected prostate tumors are restaged upwards by the pathologist, indicating that the initial staging was inaccurate. Although sophisticated nuclear magnetic resonance (NMR) spectroscopic imaging methods can aid tumor detection for organ-confined disease (8) the vast majority (>90%) of prostate cancer mortality involves disseminated, metastatic disease. No imaging method currently exists which is specific for detecting and staging extracapsular or metastatic prostate cancer.

Prostate cancer targets

The specific targeting of cancer cells has become a unifying theme driving the development of novel imaging and therapy modes (9). Targeting motifs are often antibodies or peptides directed against antigens specifically expressed on malignant cells and not expressed on healthy cells. The targeting of over-expressed membrane proteins on prostate cancer cells, using innovative therapeutic and diagnostic methods, promises to increase the specificity of prostate tumor diagnosis and treatment (10,11) while potentially increasing the efficacy and decreasing the side-effects (12,13). The most promising prostate cancer target antigen is prostate specific membrane antigen (PSMA), whose expression is mainly limited to the prostate and has been found to increase as tumor grade increases (14). Thus, antibodies against PSMA are an appealing choice for use as targeting motifs specific for prostate cancer. In addition to over-expression on the cell surface of both primary and metastatic prostate cancer

www.manaraa.com

cells, high PSMA expression has been reported in the neovasculature of most solid tumors, but not in healthy vasculature (15), suggesting that PSMA may also be a general tumor antigen that could be used to detect numerous types of cancer. Prior research by ourselves and others (16-18) has demonstrated the successful targeting of cancer. We have shown, for example, that agents conjugated to a monoclonal antibody against PSMA, specifically bind to PSMA-positive prostate cancer cells *in vitro* (19). Although PSMA is a prime target for prostate cancer, there are other possible targets. Three other membrane-bound proteins that are over-expressed in prostate cancer and implicated in cancer progression include the integrin $\alpha_v\beta_3$, the neurotensin receptor 1 (NTSR1), and prostate stem cell antigen (PSCA) (2, 20-23).

Nanoparticles for cancer imaging and therapy

Superparamagnetic nanoparticles are superior platforms for both the detection and delivery of therapeutics to tumors because they can simultaneously carry drugs and be observed using magnetic resonance imaging (MRI) (24). Exciting early developments in nanoparticle research (25-29) supported the possibility of producing magnetic imaging agents which were exquisitely specific for prostate cancer cell surface markers and could be used for the detection of both primary and metastatic disease. For example, Artemov et al. (30,31) successfully targeted superparamagnetic iron oxide nanoparticles (SPIONs) to the Her-2 receptor in breast cancer cells and detected the SPIONs by MRI. Although SPIONs have been most commonly used in contrast agent-

www.manaraa.com

enhanced MRI to date, they are not necessarily optimal. Nanoparticles with increased MR relaxivities would increase the contrast enhancement in MRI for various medical conditions including cancer. Towards this goal, our work has focused on the development of novel, superior, targeted nanoparticles as MRI and drug delivery agents for improved imaging and therapy of prostate cancer.

We chose to investigate the production of iron platinum (FePt) nanoparticles due to their higher magnetic anisotropy and stability compared with iron oxide (32-36). Much of the research on FePt has been directed towards producing ferromagnetic face-centered tetragonal (fct) particles, for use in magnetic storage devices, by annealing superparamagnetic face-centered cubic (fcc) nanoparticles at temperatures exceeding 500 °C (36-39). However, fcc **S**uperparamagnetic **I**ron **P**latinum nano**P**articles (SIPPs) are of interest by themselves due to their potential as contrast agents in MRI (40-42). For superparamagnetic MRI contrast agents, a higher magnetic moment at a given magnetic field causes larger perturbations in the magnetic relaxation times of nearby water protons and, thus, higher moment particles generate increased image contrast. SIPPs have previously been reported with volume magnetizations approaching 1,140 emu/cm^3 (1 x 10^6 A/m), the saturation magnetization of bulk FePt (43-46). These high reported magnetic moments suggested that SIPPs would be superior MRI contrast agents.

SIPPs offer significant advantages over other potential contrast agents in that they have very large magnetic effects, which are propagated over long distances, due to their extremely large induced magnetic moments. The

www.manaraa.com

surrounding water molecules, in the case of MRI, act as signal amplifiers and detectors for the magnetic field gradients induced by the nanoparticles. Alternatively, direct detection of the nanoparticles can be accomplished with the extremely sensitive superconducting quantum interference devices (SQUIDs) now available (5, 6).

Currently, clinically approved MRI contrast agents are limited to gadolinium chelates or liver-targeted iron oxide contrast agents (7). The gadolinium-based MR agents can discriminate between diseased and healthy tissues to some extent (8) but their specificity can be improved through targeting (9-12) using ligands with specific binding capabilities, such as prostate specific antibodies. Injected intravenously, SPIONs slowly extravasate from the vascular into the interstitial space, where they travel through the interstitial-lymphatic fluid to target small nodal metastases (13). A dextran coating on the iron oxide core prolongs their lifetime in the circulation, an advantage over gadolinium chelates, which generally undergo rapid renal elimination (14). Additionally, polyethylene glycol (PEG) groups on nanoparticles have been shown to increase solubility and circulation times and decrease immunogenicity (47, 48). This decrease in immunogenicity imparts the nanoparticles a stealth capability *in vivo*. A plethora of methods for biocompatibly-encapsulating drugs and hydrophobic imaging agents have been reported and include encapsulation using hydrophilic or amphiphilic components such as monomers and phospholipids (47). Furthermore, biocompatible contrast agents that also incorporate a fluorescent component offer the advantage of *in vivo* and *ex vivo* imaging using small animal

www.manaraa.com

fluorescence imagers and/or fluorescence microscopy for *in vivo* biodistribution studies and *in vitro* binding assays.

Hypothesis

In 2011, more than 200,000 men were newly diagnosed with and over 30,000 men died due to prostate cancer in the United States, making carcinoma of the prostate the second most lethal cancer in men in the United States (49). New detection methods are critically needed to achieve earlier diagnosis and better staging of the disease. SPION contrast agents have been used to enhance the contrast of tumors in MRI, but novel contrast agents with increased relaxivities would be useful in detecting smaller tumors earlier and with lower doses of the contrast agents. Additionally, the specific targeting of contrast agents and therapeutics to cells of interest is now widely accepted as a cornerstone to the development of individualized diagnosis and treatment. *Therefore, the hypothesis of this dissertation is that SIPPs and a hydrophobic chemotherapeutic drug, Paclitaxel (PTX), encapsulated in a mixture of polyethylene glycol (PEG)-, fluorescent-, and biotin-functionalized phospholipids and conjugated to a monoclonal antibody against PSMA would specifically target prostate cancer cells, be superior MRI contrast agents for prostate cancer detection (compared to SPIONs), and have increased therapeutic efficacy in vivo compared to Paclitaxel alone.*

www.manaraa.com

Specific Aims

Specific Aim 1: Previous studies, including our own, demonstrated that PSMA-targeting can be successfully used to direct SPIONs to human prostate cancer cells *in vitro*. Although these studies provided strong evidence that PSMA was a good target to use, they did not address the possibility that other membrane receptors might be equally useful and highly expressed on prostate cancer cells. More importantly, the prior studies did not address the expression of PSMA or other membrane receptors *in vivo.* From the translational standpoint, it is of vital importance to ensure that *in vitro* successes can also be achieved in an *in vivo* model to allow for the highest possible probability of clinical success. It is not uncommon to encounter difficulties either when translating *in vitro* applications to pre-clinical models or when moving such applications to clinical usage. *Therefore, specific aim one (addressed in Chapter 2) was to measure, in vitro and in vivo, mRNA and protein expression of several different membrane receptors, including PSMA, in multiple human prostate cancer cell lines and xenografts to determine the best cell line to use for testing targeted nanoparticles both in vitro and in vivo.*

Specific Aim 2: One drawback to the synthesis of various types of nanoparticles is that toxic precursors are generally used to produce the particles (35, 36, 50). Often, iron pentacarbonyl, $Fe(CO)_5$, a very hazardous reagent (51), has been used as the iron precursor in FePt syntheses (36). A number of different FePt syntheses are described by Sun (35). Recently, Zhao et al. (44) described a

www.manaraa.com

method for producing ~11 nm SIPPs using the hydrophobic surface ligand 1-octadecylamine (ODA) along with iron and platinum salts that were much less hazardous than $Fe(CO)_5$. Although the authors used this synthetic method to synthesize SIPPs using these "greener" methods, they did not optimize these particles for MRI and did not fully characterize the structural and magnetic properties of their particles. *Therefore, specific aim two (addressed in Chapter 3 and 4) was to synthesize SIPPs and characterize their structural and magnetic properties, compared to SPIONs.*

Specific Aim 3: Typical syntheses of superparamagnetic nanoparticles are performed at high temperatures in organic solvents to produce very hydrophobic nanoparticles that are stored in solvents such as hexane or chloroform. In order to use these particles for biological applications, the hydrophobic core particles must be made biocompatible (hydrophilic) so that they can be injected into the blood. Additionally, the particles must be modified in such a way so that longer circulation times and decreased immunogenicity can be achieved. Moreover, the particles must be functionalized so that antibodies and/or peptides can be conjugated to their surface to specifically target the particles to the cell of choice. *Therefore, specific aim three (addressed in Chapter 4 and 5) was to encapsulate SIPP cores and PTX in a mixture of fluorescent- and biotin-functionalized PEGylated phospholipids, to conjugate a monoclonal antibody against the best single membrane receptor determined in Aim 1, and to measure their structural and magnetic properties, drug loading, drug release rates, in vitro cytotoxicity,*

www.manaraa.com

and specific binding to human prostate cancer cell lines.

Specific Aim 4: As stated earlier, it is not uncommon for promising *in vitro* success with novel nanoparticles or treatments to fail in animals or humans. *Therefore, specific aim 4 (addressed in Chapter 5) was to quantify the therapeutic response to the particles, biodistribution, and MRI contrast enhancement in athymic nude mice bearing human prostate cancer xenografts.*

References

1. Jemal A, Bray F, Center MM, Ferlay J, Ward E, Forman D. Global cancer statistics. CA Cancer J Clin 2011.

2. Sardana G, Dowell B, Diamandis EP. Emerging biomarkers for the diagnosis and prognosis of prostate cancer. Clin Chem 2008;54(12):1951-1960.

3. Gupta A, Roobol MJ, Savage CJ, Peltola M, Pettersson K, Scardino PT, Vickers AJ, Schroder FH, Lilja H. A four-kallikrein panel for the prediction of repeat prostate biopsy: data from the European Randomized Study of Prostate Cancer Screening in Rotterdam, Netherlands. Br J Cancer 2010;103(5):708-714.

4. Studer UE, Collette L. What can be concluded from the ERSPC and PLCO trial data? Urol Oncol 2010;28(6):668-669.

5. Rabbani F, Stroumbakis N, Kava BR, Cookson MS, Fair WR. Incidence and clinical significance of false-negative sextant prostate biopsies. J Urol 1998;159(4):1247-1250.

6. Zarour L, Alumkal J. Emerging therapies in castrate-resistant prostate cancer. Curr Urol Rep 2010;11(3):152-158.

7. Di Lorenzo G, Buonerba C, Autorino R, De Placido S, Sternberg CN. Castration-resistant prostate cancer: current and emerging treatment strategies. Drugs 2010;70(8):983-1000.

8. Kurhanewicz J, Swanson MG, Nelson SJ, Vigneron DB. Combined magnetic resonance imaging and spectroscopic imaging approach to

www.manaraa.com

molecular imaging of prostate cancer. J Magn Reson Imaging 2002;16(4):451-463.

9. Peng XH, Qian X, Mao H, Wang AY, Chen ZG, Nie S, Shin DM. Targeted magnetic iron oxide nanoparticles for tumor imaging and therapy. Int J Nanomedicine 2008;3(3):311-321.

10. Afnan J, Tempany CM. Update on prostate imaging. Urol Clin North Am 2010;37(1):23-25, Table of Contents.

11. Jadvar H. Molecular imaging of prostate cancer: a concise synopsis. Mol Imaging 2009;8(2):56-64.

12. Chellat F, Merhi Y, Moreau A, Yahia L. Therapeutic potential of nanoparticulate systems for macrophage targeting. Biomaterials 2005;26(35):7260-7275.

13. Adair JH, Parette MP, Altinoglu EI, Kester M. Nanoparticulate alternatives for drug delivery. ACS Nano 2010;4(9):4967-4970.

14. Rajasekaran AK, Anilkumar G, Christiansen JJ. Is prostate-specific membrane antigen a multifunctional protein? Am J Physiol Cell Physiol 2005;288(5):C975-981.

15. Chang SS, Gaudin PB, Reuter VE, O'Keefe DS, Bacich DJ, Heston WD. Prostate-Specific Membrane Antigen: Much More Than a Prostate Cancer Marker. Mol Urol 1999;3(3):313-320.

16. Kularatne SA, Wang K, Santhapuram HK, Low PS. Prostate-specific membrane antigen targeted imaging and therapy of prostate cancer using a PSMA inhibitor as a homing ligand. Mol Pharm 2009;6(3):780-789.

17. Farokhzad OC, Karp JM, Langer R. Nanoparticle-aptamer bioconjugates for cancer targeting. Expert Opin Drug Deliv 2006;3(3):311-324.

18. Farokhzad OC, Jon S, Khademhosseini A, Tran TN, Lavan DA, Langer R. Nanoparticle-aptamer bioconjugates: a new approach for targeting prostate cancer cells. Cancer Res 2004;64(21):7668-7672.

19. Serda RE, Adolphi NL, Bisoffi M, Sillerud LO. Targeting and cellular trafficking of magnetic nanoparticles for prostate cancer imaging. Mol Imaging 2007;6(4):277-288.

20. Emonds KM, Swinnen JV, Mortelmans L, Mottaghy FM. Molecular imaging of prostate cancer. Methods 2009;48(2):193-199.

www.manaraa.com

21. McCabe NP, De S, Vasanji A, Brainard J, Byzova TV. Prostate cancer specific integrin alphavbeta3 modulates bone metastatic growth and tissue remodeling. Oncogene 2007;26(42):6238-6243.

22. Swift SL, Burns JE, Maitland NJ. Altered expression of neurotensin receptors is associated with the differentiation state of prostate cancer. Cancer Res 2010;70(1):347-356.

23. Saeki N, Gu J, Yoshida T, Wu X. Prostate stem cell antigen: a Jekyll and Hyde molecule? Clin Cancer Res 2010;16(14):3533-3538.

24. Shubayev VI, Pisanic TR, 2nd, Jin S. Magnetic nanoparticles for theragnostics. Adv Drug Deliv Rev 2009;61(6):467-477.

25. Artemov D. Molecular magnetic resonance imaging with targeted contrast agents. J Cell Biochem 2003;90(3):518-524.

26. Artemov D, Bhujwalla ZM, Bulte JW. Magnetic resonance imaging of cell surface receptors using targeted contrast agents. Curr Pharm Biotechnol 2004;5(6):485-494.

27. Johansson LO, Bjornerud A, Ahlstrom HK, Ladd DL, Fujii DK. A targeted contrast agent for magnetic resonance imaging of thrombus: implications of spatial resolution. J Magn Reson Imaging 2001;13(4):615-618.

28. Reimer P. Tumor-targeted MR contrast agents: hype or future hope? Radiology 2004;231(1):1-2.

29. Winter PM, Morawski AM, Caruthers SD, Fuhrhop RW, Zhang H, Williams TA, Allen JS, Lacy EK, Robertson JD, Lanza GM, Wickline SA. Molecular imaging of angiogenesis in early-stage atherosclerosis with alpha(v)beta3-integrin-targeted nanoparticles. Circulation 2003;108(18):2270-2274.

30. Artemov D, Mori N, Ravi R, Bhujwalla ZM. Magnetic resonance molecular imaging of the HER-2/neu receptor. Cancer Res 2003;63(11):2723-2727.

31. Artemov D, Mori N, Okollie B, Bhujwalla ZM. MR molecular imaging of the Her-2/neu receptor in breast cancer cells using targeted iron oxide nanoparticles. Magn Reson Med 2003;49(3):403-408.

32. Han L, Wiedwald U, Kuerbanjiang B, Ziemann P. Fe oxidation versus Pt segregation in FePt nanoparticles and thin films. Nanotechnology 2009;20(28):285706.

33. Kim JR, C.; Liu, P.; Sun, S. Dispersible Ferromagnetic FePt Nanoparticles. Adv Mater 2009;21:906-909.

www.manaraa.com

34. Antoniak C, Lindner J, Spasova M, Sudfeld D, Acet M, Farle M, Fauth K, Wiedwald U, Boyen HG, Ziemann P, Wilhelm F, Rogalev A, Sun S. Enhanced orbital magnetism in Fe(50)Pt(50) nanoparticles. Phys Rev Lett 2006;97(11):117201-117201 to 117201-117204.

35. Sun S. Recent Advances in Chemical Synthesis, Self-Assembly, and Applications of FePt Nanoparticles. Adv Mater 2006;18:403.

36. Sun S, Murray CB, Weller D, Folks L, Moser A. Monodisperse FePt nanoparticles and ferromagnetic FePt nanocrystal superlattices. Science 2000;287(5460):1989-1992.

37. Basit L, Nepijko SA, Shukoor I, Ksenofontov V, Klimenkov M, Fecher GH, Schonhense G, Tremel W, Felser C. Structure and magnetic properties of iron-platinum particles with y-ferric-oxide shell. Appl Phys A 2009;94:619-625.

38. Varanda LC, Jafelicci M, Jr. Self-assembled FePt nanocrystals with large coercivity: reduction of the fcc-to-L1(0) ordering temperature. J Am Chem Soc 2006;128(34):11062-11066.

39. Boyen HG, Fauth K, Branko S, Ziemann P, Kastle G, Weigl F, Banhart F, Hessler M, Schutz G, Gajbhiye NS, Ellrich J, Hahn H, Buttner M, Garnier MG, Oelhafen P. Electronic and Magnetic Properties of Ligand-Free FePt Nanoparticles. Adv Mater 2005;17(5):574-578.

40. Chen S, Wang L, Duce SL, Brown S, Lee S, Melzer A, Cuschieri A, Andre P. Engineered biocompatible nanoparticles for in vivo imaging applications. J Am Chem Soc 2010;132(42):15022-15029.

41. Morales MP, Bedard MF, Roca AG, Presa P, Hernando A, Zhang F, Zanella M, Zahoor AA, Sukhorukov GB, del Mercato LL, Parak WJ. Relaxation times of colloidal iron platinum in polymer matrixes. J Mater Chem 2009;19:6381-6386.

42. Maenosono S, Suzukia T, Saita S. Superparamagnetic FePt nanoparticles as excellent MRI contrast agents. J Magn Magn Mater 2008;320:L79-L83.

43. Xu C, Yuan Z, Kohler N, Kim J, Chung MA, Sun S. FePt nanoparticles as an Fe reservoir for controlled Fe release and tumor inhibition. J Am Chem Soc 2009;131(42):15346-15351.

44. Zhao F, Rutherford M, Grisham SY, Peng X. Formation of monodisperse FePt alloy nanocrystals using air-stable precursors: fatty acids as alloying mediator and reductant for Fe3+ precursors. J Am Chem Soc 2009;131(14):5350-5358.

www.manaraa.com

45. Barmak K, Kim J, Lewis LH, Coffey KR, Toney MF, Kellock AJ, Thiele JU. Stoichiometry - Anisotropy Connections in Epitaxial L10 FePt(001) Films. Magnetism and Magnetic Materials Conference. Anaheim, CA, USA; 2004.

46. Zeng H, Li J, Liu JP, Wang ZL, Sun S. Exchange-coupled nanocomposite magnets by nanoparticle self-assembly. Nature 2002;420(6914):395-398.

47. Serda RE, Godin B, Blanco E, Chiappini C, Ferrari M. Multi-stage delivery nano-particle systems for therapeutic applications. Biochim Biophys Acta 2010.

48. Pasut G, Veronese FM. PEGylation for improving the effectiveness of therapeutic biomolecules. Drugs Today (Barc) 2009;45(9):687-695.

49. Jemal A, Siegel R, Xu J, Ward E. Cancer statistics, 2010. CA Cancer J Clin 2010;60(5):277-300.

50. Inomata K, Sawa T, Hashimoto S. Effect of large boron additions to magnetically hard Fe-Pt alloys. J Appl Phys 1988;64(5):2537-2540.

51. Bhalerao GM, Sinha AK, Srivastava AK. Synthesis of monodispersed gamma-Fe2O3 nanoparticles using ferrocene as a novel precursor. J Nanosci Nanotechnol 2009;9(9):5502-5506.

www.manaraa.com

Chapter 2

Prostate Cancer Targeting Motifs: Expression of $\alpha_v\beta_3$, Neurotensin Receptor 1, Prostate Specific Membrane Antigen, and Prostate Stem Cell Antigen in Human Prostate Cancer Cell Lines and Xenografts

Robert M. Taylor*[1], Virginia Severns[1], David C. Brown[2], Marco Bisoffi[1,3], and Laurel O. Sillerud[1,3]

[1]Department of Biochemistry and Molecular Biology, [2]Department of Pathology, and [3]UNM Cancer Center, University of New Mexico School of Medicine, Albuquerque, NM 87131

Manuscript published in Prostate; 72:523-532, 2011

www.manaraa.com

Abstract

Background: Membrane receptors are frequent targets of cancer therapeutic and imaging agents. However, promising *in vitro* results often do not translate to *in vivo* clinical applications. To better understand this obstacle, we measured the expression differences in receptor signatures among several human prostate cancer cell lines and xenografts as a function of tumorigenicity.

Methods: Messenger RNA and protein expression levels for integrin $\alpha_v\beta_3$, neurotensin receptor 1 (NTSR1), prostate specific membrane antigen (PSMA), and prostate stem cell antigen (PSCA) were measured in LNCaP, C4-2, and PC-3 human prostate cancer cell lines and in murine xenografts using quantitative reverse transcriptase polymerase chain reaction, flow cytometry, and immunohistochemistry.

Results: Stable expression patterns were observed for integrin α_v and PSMA in all cells and corresponding xenografts. Integrin β_3 mRNA expression was greatly reduced in C4-2 xenografts and greatly elevated in PC-3 xenografts compared with the corresponding cultured cells. NTSR1 mRNA expression was greatly elevated in LNCaP and PC-3 xenografts. PSCA mRNA expression was elevated in C4-2 xenografts when compared with C4-2 cells cultured *in vitro*. Furthermore, at the protein level, PSCA was re-expressed in all xenografts compared with cells in culture.

Conclusions: The regulation of mRNA and protein expression of the cell-surface target proteins $\alpha_v\beta_3$, NTSR1, PSMA, and PSCA, in prostate cancer cells with different tumorigenic potential, was influenced by factors of the

www.manaraa.com

microenvironment, differing between cell cultures and murine xenotransplants. Integrin $\alpha_v\beta_3$, NTRS1 and PSCA mRNA expression increased with tumorigenic potential, but mRNA expression levels for these proteins do not translate directly to equivalent expression levels of membrane bound protein.

Keywords: $\alpha_v\beta_3$, NTSR1, PSCA, PSMA, tumorigenic potential, cells *versus* xenografts, membrane proteins

Introduction

Prostate cancer is the second most common cancer and the second leading cause of cancer death in men in the United States (1). Prominent and unresolved problems with the clinical management of prostate cancer include the lack of highly specific detection methods and efficient therapeutic interventions. Serum prostate specific antigen (PSA) measurements have been used as a measure of the presence of disease, yet abnormal PSA levels can also result from benign prostatic hyperplasia (BPH), and other non-malignant processes, indicating that PSA measurements lack specificity (2). Biopsies are recommended if abnormal PSA levels are found, but results from the European Randomized Study of Screening for Prostate Cancer imply that there is around a 75% negative biopsy rate using PSA as a diagnostic marker (3,4). These results confirm previous studies that reported a 30-50% false-negative biopsy rate in patients with subsequently confirmed malignancy due to small and inconspicuous lesions (5). Twenty to 40 per cent of prostate cancer patients initially responding to treatment by androgen ablation, prostatectomy or radiation, relapse and

www.manaraa.com

ultimately progress to castration resistant disease (6). Subsequent chemotherapeutic options are limited, often inefficient, and prone to side effects due to lack of specificity (7).

The specific targeting of cancer cells has become a unifying theme supporting the development of novel imaging and therapy modes (8). Often, the targeting molecules are antibodies, or peptides, which bind to cell-surface membrane proteins that are specifically-, or over-expressed on malignant cells but not expressed on healthy cells. These innovative targeted therapeutic and diagnostic methods promise to increase both the specificity and efficacy of prostate tumor diagnosis and treatment (9,10) while reducing the side-effects (11,12).

Monofunctional, targeted nanoparticles were developed as magnetic resonance imaging (MRI) and drug delivery agents for detection and therapy of prostate cancer (13). These superparamagnetic iron oxide nanoparticles (SPIONs) and superparamagnetic iron platinum particles (SIPPs), when conjugated to a monoclonal antibody against prostate specific membrane antigen (PSMA), specifically bound to PSMA-positive prostate cancer cells *in vitro* and generated contrast enhancement in MR images (13). While monofunctional nanoparticles performed well, it was reasonable to expect that the efficacy of imaging and therapeutic agents could be improved by using multiple targeting motifs on a single nanoparticle, because this would markedly increase the affinity of the nanoparticles for their targets. Furthermore, such a multifunctional approach might be required in order to detect and treat advanced tumors that are

www.manaraa.com

characterized by increased heterogeneity of target antigen expression (2). Imaging and therapeutic agents simultaneously directed to multiple targets expressed by cancer cells should show increased affinities, effectiveness, and specificities when compared with monofunctional agents. These targeting strategies can be tested in suitable prostate cancer cell models with well-characterized phenotypes, such as the human cell lines LNCaP, C4-2, and PC-3, which feature increasing tumorigenic potential and are widely-used in basic and pre-clinical research (13,14). The androgen dependent LNCaP cells were originally isolated from a lymph node metastasis, but are non-aggressive in *in vitro* assays and have low tumorigenicity *in vivo* (13). The C4-2 cells are derivatives of LNCaP cells that were passaged in castrated mice, a procedure rendering them androgen-independent, and more-invasive, characteristics associated with human progressive prostate cancer and moderate tumorigenicity (13). The androgen-independent PC-3 cells were isolated from a bone metastasis in a patient with castration-resistant prostate cancer (CRPC) and consequently display a high tumorigenic potential (13). In order to use these cells for the development of multi-targeted imaging or therapeutic agents, it was important to characterize their membrane antigen expression profiles (membrane receptor signatures) with respect to potential targeting motifs. In the present study, we measured the mRNA and cell-surface protein expression profiles for four membrane bound proteins that are over-expressed in prostate cancer and implicated in cancer progression (2,15-18). These cell-surface proteins included the integrin $\alpha_v\beta_3$, the neurotensin receptor 1 (NTSR1), PSMA, and prostate stem

www.manaraa.com

cell antigen (PSCA) in LNCaP, C4-2, and PC-3 cells. Furthermore, because promising *in vitro* results with cells often do not translate *in vivo* to similar results in tumors, we determined the differences in the expression of these receptors between cells cultured *in vitro* as opposed to cell deposits grown as xenografts in immunocompromised mice *in vivo*.

This study provides an, as yet unreported, overview of the expression signatures for membrane receptors with targeting potential in prostate cancer cells. Knowledge generated in this study should provide further guidance in assessing the utility of cell lines, animal models, and surface markers for targeting purposes in prostate cancer research. Caution should be exercised when it is assumed that the same cell-surface markers are present on cells and xenografts from these same cells.

Materials and Methods

Materials

The prostate cancer cell lines LNCaP and PC-3 were purchased from the American Tissue Type Collection (Manassas, VA, USA). The C4-2 prostate cancer cell line was a kind gift from Dr. G.N. Thalmann (University of Bern, Switzerland). Anti-PSMA, clone J591 antibody was purchased from Neil H. Bander, MD (Cornell College of Medicine, USA). FITC-labeled mouse IgG_1 control antibody was obtained from BD Biosciences (San Jose, CA, USA). FITC-labeled mouse anti-PSMA IgG_1, clone 107-1A4 antibody was obtained from

www.manaraa.com

Medical & Biological Laboratories Co., Ltd. (Woburn, MA, USA). FITC-labeled mouse anti-PSCA IgG_1, clone 7F5 and mouse anti-NTSR1 IgM antibodies were obtained from Santa Cruz Biotechnology, Inc. (Santa Cruz, CA, USA). FITC-labeled mouse anti-CD51/61 IgG_1, clone 23C6 and FITC-labeled rat anti-mouse, clone RMM-1 antibodies were obtained from Biolegend (San Diego, CA, USA). Quantum Simply Cellular anti-Mouse IgG-Medium Level epitope-density calibration beads were obtained from Bangs Laboratories, Inc. (Fishers, IN, USA). All other chemicals and supplies were purchased from common manufacturers.

Cell Culture

All cell lines were cultured on 75 mm plastic plates in T-medium with 10% FCS (19) at 37 °C in a humidified, 5% CO_2 atmosphere. Upon reaching 90% confluency, cells used for qRT-PCR were detached from the plates with the aid of a 0.5% trypsin solution containing 0.02% EDTA, collected with centrifugation at 700 rpm and stored at -80 °C in PBS. Cells used for flow cytometry were released using 5.0 mM EDTA and pipetted to form a monodisperse suspension. Cells were then washed with PBS, and immediately used.

Xenograft Production

The University of New Mexico Institutional Animal Care and Use Committee approved all experiments involving animals. Three million LNCaP, C4-2, or PC-3 cells in 1:1 (vol/vol) BD Matrigel™ (BD Biosciences, San Jose, CA,

www.manaraa.com

USA) were injected into the right flank of 5-8 week old athymic nude male mice (Harlan Sprague Dawley, Frederick, MD, USA). Once the tumors had reached a volume of ~100 mm^3, the mice were euthanized using CO_2 asphyxiation. For qRT-PCR, the tumors were excised, flash frozen in liquid nitrogen, and stored at -80 °C. For immunohistochemistry, tumors were excised and fixed in 10% buffered formalin.

Flow Cytometry

The Mean Channel Fluorescence (MCF) of cells stained with fluorescein-isothiocyante-, (FITC)-, labeled IgG_1 antibodies was compared with a standard curve generated using the appropriate IgG_1 corrected for the IgG_1 control fluorescence. The epitope-density calibration beads and 10^5 cells were stained separately by the addition of 15 µl of the appropriate antibody or control antibody in 100 µl Phosphate Buffered Saline (PBS). Cells and beads were incubated in the dark at room temperature for 15 minutes, washed once with PBS, and resuspended in 200 µl PBS. The calibration beads and cells were analyzed using FL1 on a FACSCalibur flow cytometer (BD Biosciences, San Jose, CA, USA). IgG_1 antibodies against all epitopes were available, except for those against NTSR1, which were only of the IgM class.

Since the epitope-density calibration beads were specific for IgG antibodies, and could not be used for the NTSR1-directed IgM antibodies, we compared the MCF of the cells stained for NTSR1 with that of the secondary antibody alone. One hundred thousand cells were stained by the addition of 15 µl

www.manaraa.com

of NTSR1 IgM antibody in 100 µl PBS. Cells were incubated in the dark at room temperature for 15 minutes, washed once with PBS, and resuspended in 100 µl PBS. Fluorescent staining was performed by adding 15 µl of FITC-labeled anti-mouse antibody to the labeled and control, unlabeled cells. These samples were incubated in the dark at room temperature for 15 minutes, washed once with PBS, and resuspended in 200 µl PBS. The calibration beads and cells were analyzed using FL1 on a FACSCalibur flow cytometer (BD Biosciences, San Jose, CA, USA).

Messenger RNA (mRNA) Expression Analysis by Quantitative Real Time Reverse Transcriptase Polymerase Chain Reaction (qRT-PCR)

Baseline expression of $\alpha_{v,}$ β_3, NTSR1, PSMA, and PSCA was determined by qRT-PCR. Cultured cells were recovered as explained above. Tissues (0.1-0.5 mg) were immediately frozen in liquid nitrogen upon resection from the animals and subjected to complete homogenization (15-100 seconds) in isothiocyante containing chaotropic buffer (Qiagen, Valencia, CA, USA) using a rotor-stator homogenizer. Total RNA was extracted using RNEasy kits from Qiagen (Valencia, CA, USA) according to the manufacturer's protocols, and analyzed for concentration and purity using a Nanodrop spectrophotometer (Thermo Scientific, Wilmington DE, USA). The integrity of the 5 S, 18 S, and 28 S ribosomal RNAs was examined using an Agilent 2100 Bioanalyzer (Agilent Technologies, Santa Clara, CA, USA). Complementary DNA (cDNA) was prepared using the RETROscript cDNA synthesis kit from Ambion (Austin, TX,

www.manaraa.com

USA) using random decamer primers in the presence of an RNase inhibitor (Promega, Madison, WI, USA). TaqMan qRT-PCR was performed using a Roche 480 Light Cycler (Roche, Indianapolis, IN, USA). Primers and probes were designed using sequence information from the National Center for Biotechnology Information (NCBI) and Primer Express Software (Applied Biosystems, Carlsbad, CA, USA). The sequences of the primers and probes are given in Table 2.1. Five hundred nanograms of cDNA were used per reaction in a total volume of 25 µl of Taq Plus PCR Master Mix (Qiagen, Valencia, CA, USA) containing 900 nM of the primers and 300 nM of the probes.

Table 2.1 Primers and probes used for qRT-PCR

Receptor	Primer Sequence (5' > 3')	Probe[1] (5' > 3')
α_v	**F-** TTCCCTTCCGGGTAGACG TA **R-** TGTGCAAAAATAATGCTCTTCGTAT	TGCTGGATAAACACAAGC AAAAGGGAGC
β_3	**F-** TTTACCACTGATGCCAAGACTCA **R-** CCGTCATTAGGCTGGACAAT	CATTGGACGGAAGGCTGG CAG
NTSR1	**F-** GGCGCCTCATGTTCTGCTA **R-** GTGCGTTGGTCACCATGTAGA	ATGAGCAGTGGACTCCGT TCCTCTATGACTTCT
PSCA	**F-** CAGGACTACTACGTG GGCAAGA **R-** CGCTGGCGTTGCACAA	AACATCACGTGCTGTGAC ACCGA
PSMA	**F-** GCTGATAAGCGAGGCATTAGT **R-** TGCGCGCCCTCCAA	AGACTTTACCCCGCCGTG GTG

[1] All probes had a 5'-56-FAM fluorophore and a 36-TAMSp-3' quencher

The cycling conditions were 95°C 10 min, 45x (95°C 15 sec, 60°C 1 min). No-template and non-reverse-transcribed RNAs were used as controls. All reactions were run in triplicate. Signals for α_v, β_3, NTSR1, PSMA, and PSCA were normalized to RNA input using the signals from TATA binding protein (TBP). The

www.manaraa.com

expression differences were calculated by the $2^{-\Delta\Delta Ct}$ method for assessing relative expression.

Immunohistochemistry

Formalin-fixed tumors were paraffin-embedded and stained by Tricore Reference Laboratory (Albuquerque, NM, USA) using an automated procedure with a Ventana BenchMark XT IHC/ISH Staining Module and polyclonal rabbit anti-human PSCA antibody (Invitrogen, Carlsbad, CA, USA).

Results

Messenger RNA and protein expression levels for integrin $\alpha_v\beta_3$, NTSR1, PSMA, and PSCA were measured in LNCaP, C4-2, and PC-3 human prostate cancer cell lines using quantitative reverse transcriptase polymerase chain reaction, flow cytometry, and immunohistochemistry. Of particular interest were the differences in the expression levels of these receptors observed between cells cultured *in vitro* as opposed to cell deposits grown as xenografts in immunocompromised mice *in vivo*.

Membrane Receptor mRNA Expression in Cells.

The baseline mRNA expression of α_v, β_3, NTSR1, PSMA, and PSCA, was measured using qRT-PCR, in LNCaP, C4-2, and PC-3 human prostate cancer

www.manaraa.com

cell lines; these cell types were chosen for their increasing tumorigenic potential (20) in the order LNCaP, C4-2, and PC-3. Figure 2.1 shows growth curves for

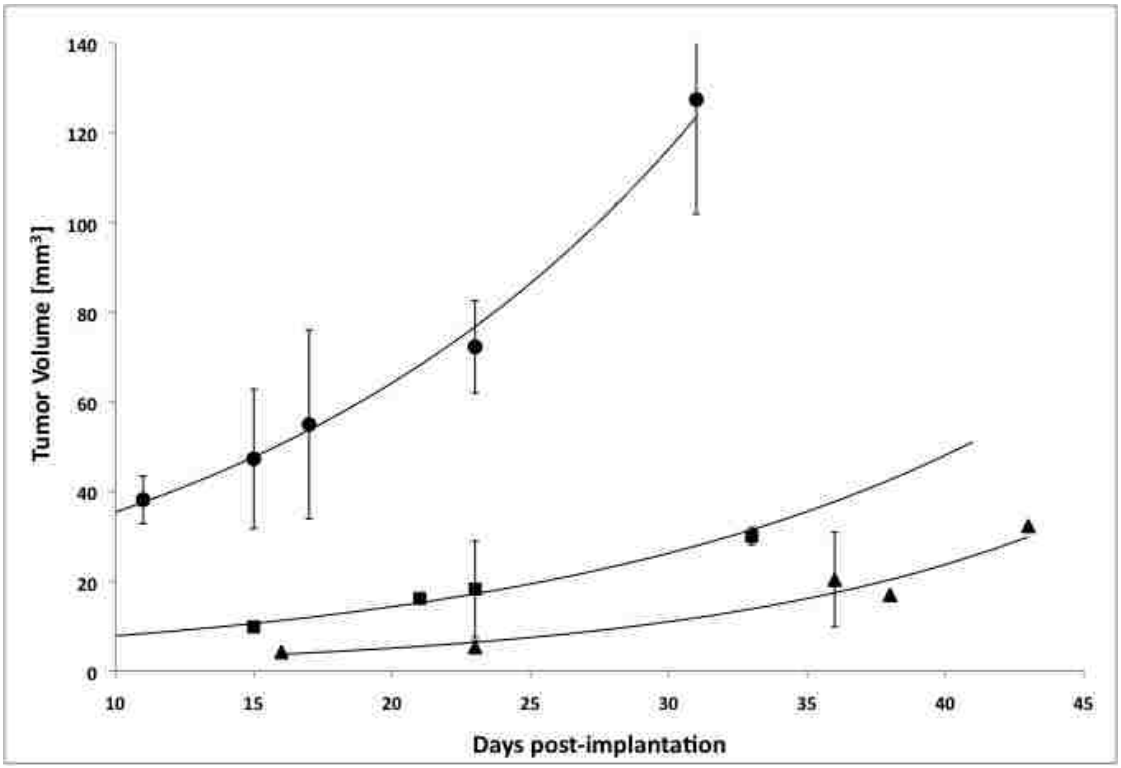

Figure 2.1 LNCaP, C4-2, and PC-3 xenograft growth curves. Increase in tumor volume versus days post-implantation of LNCaP, C4-2, or PC-3 cell deposits. Circle = PC-3, Square = C4-2, and Triangle = LNCaP with n = 5, 2, and 3 respectively.

www.manaraa.com

these three types of cell deposits grown as xenografts in the flanks of immunocompromised mice. The growth curves suggest that the PC-3 xenografts grow much more rapidly when implanted in the flanks of nude mice, compared to the LNCaP and C4-2 xenografts and, therefore, the PC-3 cell line is much more tumorigenic in this site of implantation. A summary of the mRNA expression is given in Table 2.2, where the data are reported relative to the least tumorigenic cell line, LNCaP.

Table 2.2 Receptor mRNA and Protein Expression in Cells and Tumors

Cell Line/ Xenograft	Cell mRNA Expression	Tissue mRNA Expression	Cell Epitope-Density
	PSMA[1]	PSMA[1]	PSMA[2]
LNCaP	1.00 ± 0.09	1.00 ± 0.08	105.00 ± 10.0 (10^4)
C4-2	0.51 ± 0.04	1.37 ± 0.11	167.00 ± 28.0 (10^4)
PC-3	0.01 ± 0.00	0.01 ± 0.00	1.42 ± 0.48 (10^4)
	PSCA[1]	PSCA[1]	PSCA[2]
LNCaP	1.00 ± 0.09	1.00 ± 0.07	0
C4-2	0.01 ± 0.00	3.81 ± 0.33	0
PC-3	1.57 ± 0.11	1.20 ± 0.10	0
	α_v[1]	α_v[1]	$\alpha_v\beta_3$[2]
LNCaP	1.00 ± 0.02	1.00 ± 0.64	1.12 ± 0.11 (10^4)
C4-2	2.09 ± 0.18	3.23 ± 0.05	1.17 ± 0.46 (10^4)
PC-3	18.61 ± 1.59	2.94 ± 0.20	0.77 ± 0.02 (10^4)
	β_3[1]	β_3[1]	NA
LNCaP	1.00 ± 0.08	1.00 ± 0.05	NA
C4-2	31.45 ± 2.25	1.21 ± 0.01	NA
PC-3	5.39 ± 0.17	316.60 ± 26.64	NA
	NTSR1[1]	NTSR1[1]	NTSR1[3]
LNCaP	1.00 ± 0.09	1.00 ± 0.03	67.9 ± 27.1
C4-2	2.92 ± 0.23	0.05 ± 0.01	79.3 ± 15.1
PC-3	9.77 ± 0.73	88.82 ± 7.61	15.9 ± 22.4

[1] Expression relative to LNCaP
[2] Receptors per cell
[3] Mean channel fluorescence
NA: not applicable

www.manaraa.com

The LNCaP cell line had the highest amount of PSMA mRNA expression *in vitro*, but had lower mRNA levels for all of the other receptors, compared to the other two cell lines. The PC-3 cell line, which has the highest tumorigenic potential (20) and was originally collected as a bone metastasis from a patient with CRPC (13) was almost devoid of PSMA mRNA, but showed the highest mRNA expression for α_v, NTSR1, and PSCA of all the cell lines. The PC-3 cells also made 5-fold more of the integrin β_3 mRNA than the LNCaP cells. These findings imply that an inverse relationship may exist between the tumorigenicity of these cell lines and their PSMA mRNA expression. Conversely, the cellular tumorigenicity appears to positively correlate with the mRNA expression levels of the other three membrane receptors. The C4-2 cell line, a moderately tumorigenic, androgen-independent progeny of LNCaP cells (13), had the highest level of β_3 integrin mRNA expression and a 2- to 3-fold greater mRNA expression of α_v and NTSR1 than that found for LNCaP cells.

Membrane Receptor mRNA Expression in Xenografts.

In order to determine if the murine microenvironment altered mRNA expression in xenografts as compared to cells, we next measured receptor mRNA levels in LNCaP, C4-2, and PC-3 human prostate cancer cell xenografts grown as subcutaneous tumors in immunocompromised mice. C4-2 and LNCaP xenografts displayed significant PSMA mRNA expression, while the PC-3 xenograft was essentially devoid of PSMA mRNA. The PC-3 xenograft, similar to the cultured PC-3 cells, showed the highest NTSR1 mRNA expression, an ~88-

www.manaraa.com

fold increase with respect to the LNCaP xenograft. The PC-3 xenograft also had ~316-fold higher β_3 mRNA expression and elevated mRNA expression of both α_v and PSCA, compared to the LNCaP xenograft. Unexpectedly, the C4-2 xenograft had almost 4-fold higher PSCA mRNA expression, compared to the LNCaP xenograft even though the C4-2 cells lacked PSCA mRNA expression *in vitro*. Additionally, the C4-2 cell line, which expressed the highest amount of β_3 expression, at a ratio of ~ 30:1 over LNCaP cells, and the second highest amount of NTSR1 mRNA expression, *in vitro*, lost virtually all of its NTSR1 mRNA expression in the xenograft and also had an ~ 50-fold reduction in β_3 mRNA *in vivo*.

Comparison of Membrane Receptor mRNA Expression in Cells and Xenografts

To determine the changes in α_v, β_3, NTSR1, PSMA, and PSCA mRNA expression that may occur when cells grown in a semi-defined medium *in vitro* are transferred to a more physiological and complex environment *in vivo*, the qRT-PCR data for the membrane receptors' mRNA expression in xenografts was compared to each corresponding cell line. The results (Table 2.3) shows that PSMA mRNA decreased by about 50 % in all of the xenografts compared to the same cells grown in culture. A similar decrease in mRNA expression *in vivo* was evident for PSCA in LNCaP and PC-3 xenografts. However, the C4-2 xenograft displayed PSCA mRNA expression that markedly increased by ~1450-fold in the

www.manaraa.com

Table 2.3 Comparison of mRNA Expression Between Cells and Xenografts

Cell Line/Xenograft	*Xenograft mRNA Expression Relative to Cells*
	PSMA[1]
LNCaP	0.30 ± 0.02
C4-2	0.63 ± 0.04
PC-3	0.55 ± 0.05
	PSCA[1]
LNCaP	0.48 ± 0.03
C4-2	1451.15 ± 96.37
PC-3	0.37 ± 0.03
	α_v[1]
LNCaP	1.69 ± 1.08
C4-2	2.61 ± 0.04
PC-3	0.27 ± 0.02
	β_3[1]
LNCaP	0.42 ± 0.02
C4-2	0.02 ± 0.00
PC-3	24.79 ± 2.09
	NTSR1[1]
LNCaP	67.66 ± 2.30
C4-2	1.16 ± 0.11
PC-3	615.35 ± 20.25

[1] mRNA expression relative to the corresponding cell line grown in culture

xenograft relative to C4-2 cells. The C4-2 xenograft also exhibited modest 1.2 to 2.6-fold increases in α_v and NTSR1 mRNA expression relative to C4-2 cells. Large increases in the NTSR1 (615 X) and β_3 (25 X) mRNA expression were also found in PC-3 xenografts compared to the expression in cells. These data suggested that mRNA expression changed in different environments (*in vitro versus in vivo*), and added support to the correlation mentioned above between tumorigenicity and expression of cellular mRNA for $\alpha_v\beta_3$, NTSR1, and PSCA.

www.manaraa.com

Membrane Receptor Protein Expression in Cells

It is well known that mRNA expression, as measured both *in vitro* and *in vivo*, may not always be representative of actual protein expression levels (21). Therefore, we measured the number of $\alpha_v\beta_3$, NTSR1, PSMA, and PSCA membrane receptors on the surface of each of the cell lines using flow cytometry and epitope-density calibration particles (See methods). Although the LNCaP cells were found (Table 2.2) to possess a great number (~ 1 million) of PSMA proteins per cell, the C4-2 cells displayed the highest PSMA protein expression with ~ 1.7 million PSMA receptors per cell. Interestingly, although the PC-3 cells were found to contain only low, essentially background, levels of PSMA mRNA, both *in vitro* and *in vivo*, a modest number (~14,000 per PC-3 cell) of PSMA proteins were found on the cell surface. Both C4-2 and LNCaP cell lines expressed ~11,500 $\alpha_v\beta_3$ integrins per cell, while the PC-3 cells showed less at ~7,700 $\alpha_v\beta_3$ integrins per cell. By measuring the Mean Channel Fluorescence for the NTSR1 protein we found that both LNCaP and C4-2 cells had high expression of NTSR1 on the surface of the cells. The PC-3 cells had ~ 4.5-fold less NTSR1 protein expression *in vitro*, compared to LNCaP and C4-2 cells, even though the PC-3 cells had the highest NTSR1 mRNA expression *in vitro*. The PSCA protein was not expressed on the surface of any of the three cell lines *in vitro*.

www.manaraa.com

Immunohistochemistry for PSCA in Xenografts

Even though the PSCA protein could not be detected (Table 2.2) on the surfaces of our cell lines, the mRNA expression data from the xenografts (Table 2.3) indicated that PSCA might be actually expressed *in vivo*, particularly for the C4-2 cell line where these xenografts made more than 1400 times as much mRNA as the cells. For this reason, PSCA protein expression was determined by immunohistochemistry (IHC) in LNCaP, C4-2, and PC-3 xenografts generated in immunocompromised mice. Although PSCA protein was undetectable on the surfaces of cells cultured *in vitro* by the flow cytometric technique (Table 2.2), punctate staining for PSCA was observed within the tissue cells by IHC in all xenografts (Figure 2.2A-C). The staining intensity for PSCA in these xenografts was comparable to the intensity found in human prostate cancer tissue used as a positive control (Figure 2.2F), while there was a complete absence of PSCA staining, either in the mouse splenic tissue (Figure 2.2E), or human prostate cancer tissue incubated in the absence of the primary antibody (Figure 2.2D), which were used as negative controls. The staining for PSCA observed in the IHC of the xenografts was the same type of punctate staining as reported by others in human tumors, and in LAPC-4 cells that are known to highly-express surface PSCA (22).

Taken together, the mRNA and protein data emphasize that regulation of mRNA expression of the membrane bound and potential target proteins $\alpha_v\beta_3$, NTSR1, PSMA, and PSCA in prostate cancer cells with different tumorigenic potential can be influenced by factors of the microenvironment, such as in murine

www.manaraa.com

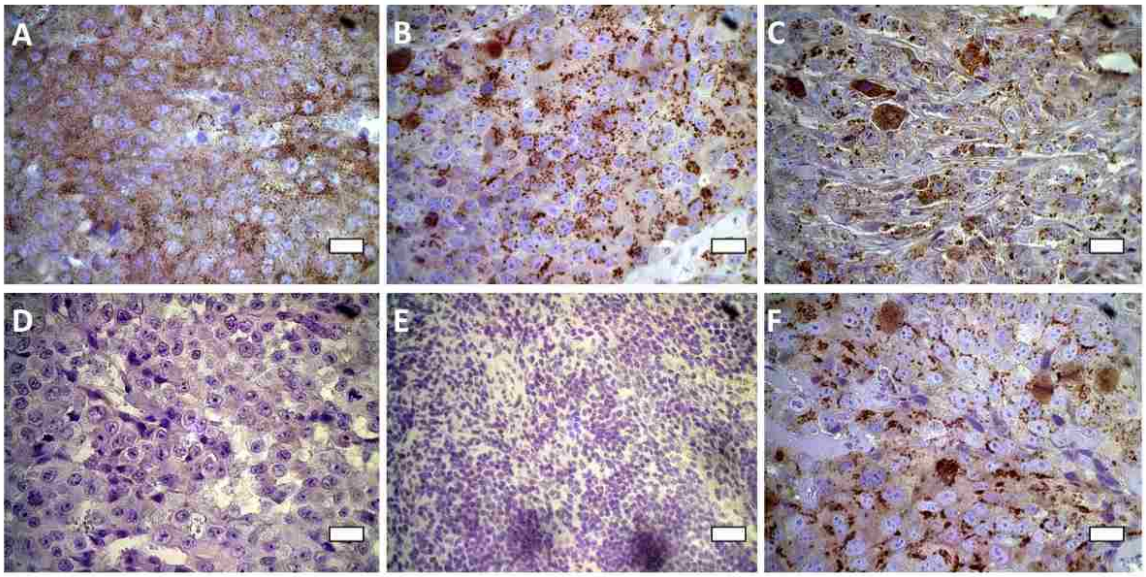

Figure 2.2 Immunohistochemical staining for PSCA in human prostate cancer xenografts in immunocompromised mice and in human prostate cancer tissue. (A) LNCaP xenograft; (B) C4-2 xenograft; (C) PC-3 xenograft; (D) human malignant prostate tissue in the absence of primary antibody [negative control]; (E) mouse spleen [negative control]; (F) human malignant prostate tissue in the presence of primary antibody [positive control]. Scale bars are 20 μm.

www.manaraa.com

xenotransplants. In addition, correlations appear to exist between membrane receptor expression signatures and tumorigenicity, but mRNA expression levels for these proteins do not translate directly to equivalent expression levels of membrane bound protein. These trends are graphically summarized in Figure 2.3.

Discussion

Three main findings are reported in this study that are of importance for research on improved prostate cancer imaging and therapeutic targeting agents, as exemplified by our previously reported functionalized iron oxide nanoparticles (23). First, our findings indicate the necessity of verifying the presence of target proteins at the cell surface, as the level of mRNA expression does not necessarily translate into protein expression levels. This discrepancy was evident for PSMA expression in PC-3 cells. We have confirmed that PC-3 cells express little or no PSMA (24), even though these cells represent the most tumorigenic and advanced prostate cancer cell line examined here. On the other hand, in advanced CRPC in humans, PSMA expression increased markedly with tumor grade, stage, and after androgen-deprivation therapy (25). Our data show a 100-fold decrease in the expression of PSMA mRNA in PC-3 cells and xenografts compared with the LNCaP and C4-2 lines. This decrease in mRNA corresponded to a similar ~100-fold decrease (to ~14,000 from more than 1 million) in the number of PSMA receptors per cell (Figure 2.3A and Table 2.2). Further discrepancies were observed for PSCA, for which even though mRNA

www.manaraa.com

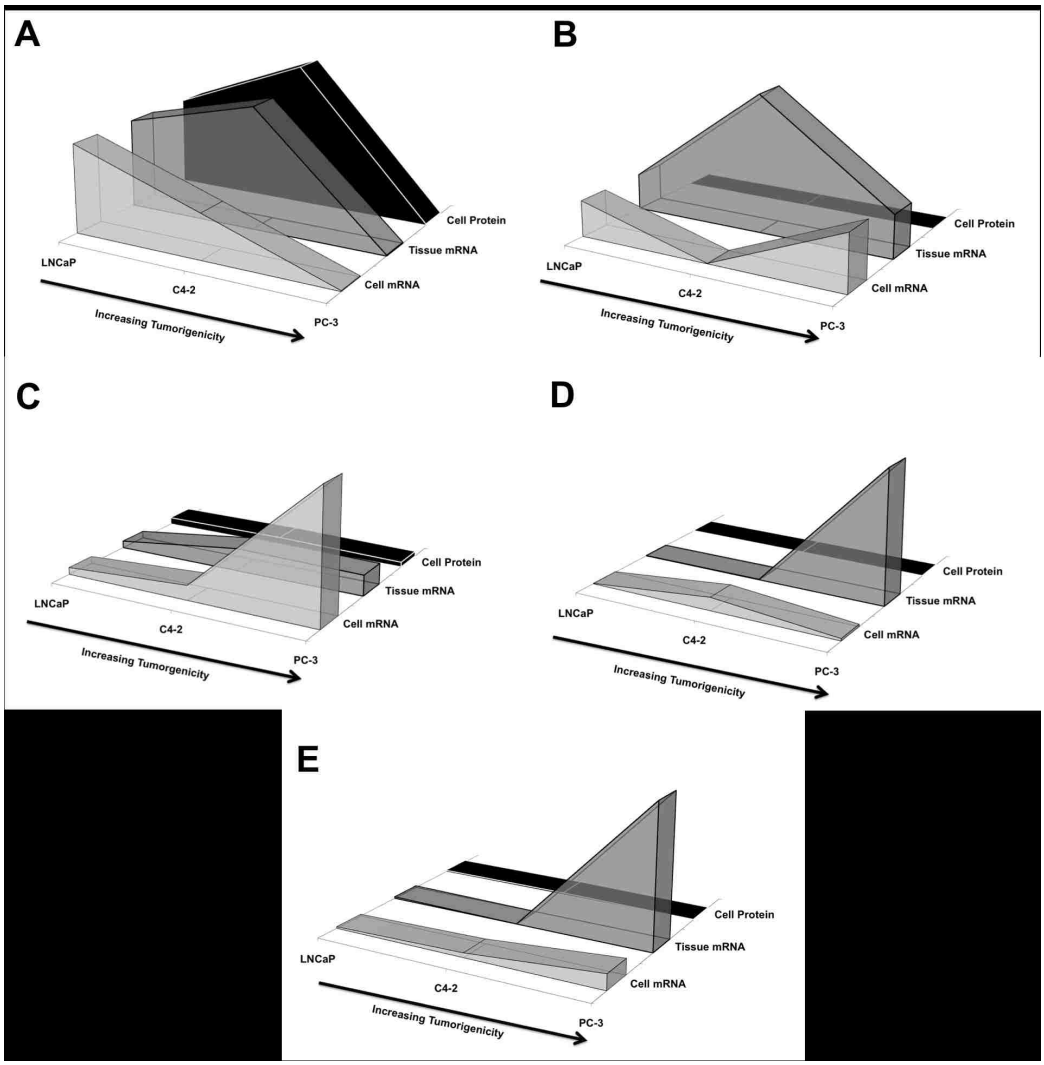

Figure 2.3 Trends of membrane receptor mRNA and protein expression in human prostate cancer cells and in murine xenografts. Expression of membrane receptors PSMA (A), PSCA (B), integrin α_U (C), integrin β_3 (D), and NTSR1 (E) for human prostate cancer cells of increasing tumorigenic potential, in the order: LNCaP, C4-2, and PC-3. Messenger RNA expression levels for cells cultured *in vitro* (front shapes) and as xenografts *in vivo* (middle shapes), and protein levels (back shapes) are shown normalized to LNCaP cells or xenografts.

www.manaraa.com

was expressed in all of the cells analyzed, and no protein could be detected on their cell surfaces (Figure 2.3B and Table 2.2), was yet expressed in xenografts (Figure 2.2A-C). We found that $\alpha_v\beta_3$ protein expression was comparable in all three of the cell lines, although both α_v and β_3 mRNA levels appeared to increase with tumorigenicity in the three different cell lines and xenografts. Similar trends were observed for NTSR1 in C4-2 and PC-3 cells (Figure 2.3E), indicating that the comparative rate of protein translation for these surface markers can greatly differ in prostate cancer cells of various origins.

A second important finding is the discordant expression of some of the surface markers under investigation between cells grown in culture and as xenografts in immunocompromised mice. Marked differences were found for integrin β_3, NTSR1, and PSCA (Figure 2.3 and Table 2.3). Most prominently, PSCA mRNA expression was dramatically enhanced in C4-2 xenografts (Figure 2.3B and Table 2.3) but the protein was not detectable on the surface of the parent cell line. The presence of the PSCA protein in C4-2 and other xenografts, verified by IHC, resembled PSCA expression in human tissues (Figure 2.2). PSCA is a glycosylphosphatidylinositol (GPI)-anchored membrane antigen that has been reported to be over-expressed in both primary and metastatic prostate cancer lesions (18,26,27). Since we measured PSCA mRNA expression both *in vitro* and *in vivo* in all cell lines, one possible explanation for the lack of PSCA protein *in vitro* could be that PSCA protein is not translated in the absence of the extracellular matrix (ECM). GPI-anchors are known to be added to the C-terminus of peptides as a post-translational modification (28), and thus, PSCA

www.manaraa.com

may not have the proper GPI-anchor attached *in vitro*. Although a detailed understanding of PSCA regulation is still elusive, our data suggest that PSCA expression is affected by cell type and ECM dependent contact.

Integrin $\alpha_v\beta_3$ has been proposed as a neovasculature-targeting motif for diagnostics and therapeutics due to its over-expression on newly formed vasculature within tumors (16,29-32). In this study, both integrin subunits experienced an induction of expression *in vivo* in the more tumorigenic cell types, i.e. C4-2 and PC-3, potentially as a consequence of cell-cell and cell-ECM interactions. Similarly, relative strong inductions in the *in vivo* setting were observed for NTSR1 in LNCaP and PC-3 cells (Figure 2.3E and Table 2.3). The NTSR1 receptor is over-expressed in numerous types of solid tumors and NTSR1 receptor binding to neurotensin (NT) has been reported to increase proliferation of several types of cancer cells, including prostate cancer cells (17,33). Further, NT functions via autocrine, paracrine, and endocrine actions in prostate cancer tissues (34,35). Consequently, a plausible explanation for the observed induction of NTSR1 in xenografts could be due to autocrine NT stimulation.

A final important finding is that a relationship appears to exist between membrane receptor signatures and tumorigenicity. We found that PSMA mRNA and protein expression levels tended to be inversely related to tumorigenic potential, both *in vitro* and *in vivo*. Additionally, $\alpha_v\beta_3$ tended to increase with tumorigenic potential both *in vitro* and *in vivo* (Figure 2.3C-D). It is possible that the degree of $\alpha_v\beta_3$ expression is not only dependent on the extent of

www.manaraa.com

vascularization within tumors, but also on the tumorigenic potential of the cells. We also found that NTSR1 mRNA expression increased with increasing tumorigenic potential both *in vitro* and *in vivo* yet, NTSR1 protein expression was inversely related to tumorigenic potential *in vitro*, reflecting our first main finding above. In the future, it may also be worthwhile to compare membrane receptor expression changes that may or may not occur when the cell deposits are instead implanted in the prostate or bone of immunocompromised mice.

Taken together, our data demonstrate that the membrane receptor expression profiles are altered with analogous changes in tumorigenic potential and that these alterations may comprise signatures of the tumorigenic state. Moreover, these membrane receptor signatures were altered for *in vitro* and *in vivo* models. We conclude that targeting nanoparticles, diagnostics, and therapeutics with multiple antibodies or peptides against PSMA as well as $\alpha_v\beta_3$, NTSR1, and/or PSCA may be more beneficial in diagnosing and treating early stage prostate cancer and CRPC than PSMA targeting alone. In addition, a major finding is that cell lines that do not express certain receptors, such as PSCA, *in vitro*, may very well express these receptors *in vivo* and prove to be useful receptors for targeting novel agents in humans.

Conclusions

PSMA is the membrane receptor most frequently used for targeting prostate cancer cells (23,30,36-38), and we conclude that LNCaP and the castration resistant and more tumorigenic C4-2 cells are ideal cell models for

www.manaraa.com

PSMA directed targeting, as these cell lines display relatively high and persistent PSMA protein expression *in vitro* and *in vivo*. However, we provide evidence that additional targeting motifs exist that could increase the specificity and efficacy of imaging and treatment schemes, as shown by the expression of $\alpha_v\beta_3$, NTSR1, and PSCA in relevant cell and xenograft models of prostate cancer. In fact, co-targeting strategies may be necessary in light of the fact that membrane receptor signatures may change over time as the tumor progresses and that intra-tumoral heterogeneity may lead to variability in expression of any single membrane receptor, thereby hampering efficacy. Furthermore, we found that membrane receptor signatures change not only with alterations in tumorigenicity but are also modified in *in vitro* and *in vivo* models. We suggest that designing targeted diagnostics and/or therapeutics using cell models such as LNCaP, C4-2, and PC-3 should ideally include up-front *in vivo* measurements of the target membrane receptors, which may reveal optimal models under physiologically relevant conditions.

This study provides a novel comparison of expression signatures of prominent membrane receptors for prostate cancer targeting using widely used prostate cancer cells grown *in vitro* and *in vivo*. Knowledge reported herein should be helpful in guiding the development of targeting strategies for imaging and therapeutic agents using membrane receptor signatures rather than single membrane-bound targets. This approach should in turn overcome the difficulties often encountered when translating *in vitro* applications to pre-clinical models and when transitioning such applications towards clinical use.

www.manaraa.com

Acknowledgments

This research was supported by the National Institutes of Health grant 5RO1CA123194 to L.O.S. We acknowledge the use of the Keck-UNM Genomics Resource; a facility supported by the WM Keck Foundation, the State of New Mexico and the UNM Cancer Research and Treatment Center. We thank the UNM Flow Cytometry Shared Resource Center, which is supported by the University of New Mexico Health Sciences Center and the University of New Mexico Cancer Center. We also thank Tricore Reference Laboratory, Albuquerque, NM for their services in immunohistochemistry, and the UNM Department of Biochemistry and Molecular Biology for their vital administrative support.

www.manaraa.com

References

1. Jemal A, Bray F, Center MM, Ferlay J, Ward E, Forman D. Global cancer statistics. CA Cancer J Clin 2011.

2. Sardana G, Dowell B, Diamandis EP. Emerging biomarkers for the diagnosis and prognosis of prostate cancer. Clin Chem 2008;54(12):1951-1960.

3. Gupta A, Roobol MJ, Savage CJ, Peltola M, Pettersson K, Scardino PT, Vickers AJ, Schroder FH, Lilja H. A four-kallikrein panel for the prediction of repeat prostate biopsy: data from the European Randomized Study of Prostate Cancer Screening in Rotterdam, Netherlands. Br J Cancer 2010;103(5):708-714.

4. Studer UE, Collette L. What can be concluded from the ERSPC and PLCO trial data? Urol Oncol 2010;28(6):668-669.

5. Rabbani F, Stroumbakis N, Kava BR, Cookson MS, Fair WR. Incidence and clinical significance of false-negative sextant prostate biopsies. J Urol 1998;159(4):1247-1250.

6. Zarour L, Alumkal J. Emerging therapies in castrate-resistant prostate cancer. Curr Urol Rep 2010;11(3):152-158.

7. Di Lorenzo G, Buonerba C, Autorino R, De Placido S, Sternberg CN. Castration-resistant prostate cancer: current and emerging treatment strategies. Drugs 2010;70(8):983-1000.

8. Peng XH, Qian X, Mao H, Wang AY, Chen ZG, Nie S, Shin DM. Targeted magnetic iron oxide nanoparticles for tumor imaging and therapy. Int J Nanomedicine 2008;3(3):311-321.

9. Afnan J, Tempany CM. Update on prostate imaging. Urol Clin North Am 2010;37(1):23-25, Table of Contents.

10. Jadvar H. Molecular imaging of prostate cancer: a concise synopsis. Mol Imaging 2009;8(2):56-64.

11. Chellat F, Merhi Y, Moreau A, Yahia L. Therapeutic potential of nanoparticulate systems for macrophage targeting. Biomaterials 2005;26(35):7260-7275.

12. Adair JH, Parette MP, Altinoglu EI, Kester M. Nanoparticulate alternatives for drug delivery. ACS Nano 2010;4(9):4967-4970.

المنارة للاستشارات
www.manaraa.com

13. Sobel RE, Sadar MD. Cell lines used in prostate cancer research: a compendium of old and new lines--part 1. J Urol 2005;173(2):342-359.

14. Sobel RE, Sadar MD. Cell lines used in prostate cancer research: a compendium of old and new lines--part 2. J Urol 2005;173(2):360-372.

15. Emonds KM, Swinnen JV, Mortelmans L, Mottaghy FM. Molecular imaging of prostate cancer. Methods 2009;48(2):193-199.

16. McCabe NP, De S, Vasanji A, Brainard J, Byzova TV. Prostate cancer specific integrin alphavbeta3 modulates bone metastatic growth and tissue remodeling. Oncogene 2007;26(42):6238-6243.

17. Swift SL, Burns JE, Maitland NJ. Altered expression of neurotensin receptors is associated with the differentiation state of prostate cancer. Cancer Res 2010;70(1):347-356.

18. Saeki N, Gu J, Yoshida T, Wu X. Prostate stem cell antigen: a Jekyll and Hyde molecule? Clin Cancer Res 2010;16(14):3533-3538.

19. Thalmann GN, Anezinis PE, Chang SM, Zhau HE, Kim EE, Hopwood VL, Pathak S, von Eschenbach AC, Chung LW. Androgen-independent cancer progression and bone metastasis in the LNCaP model of human prostate cancer. Cancer Res 1994;54(10):2577-2581.

20. Aalinkeel R, Nair MP, Sufrin G, Mahajan SD, Chadha KC, Chawda RP, Schwartz SA. Gene expression of angiogenic factors correlates with metastatic potential of prostate cancer cells. Cancer Res 2004;64(15):5311-5321.

21. Gry M, Rimini R, Stromberg S, Asplund A, Ponten F, Uhlen M, Nilsson P. Correlations between RNA and protein expression profiles in 23 human cell lines. BMC Genomics 2009;10:365.

22. Gu Z, Thomas G, Yamashiro J, Shintaku IP, Dorey F, Raitano A, Witte ON, Said JW, Loda M, Reiter RE. Prostate stem cell antigen (PSCA) expression increases with high gleason score, advanced stage and bone metastasis in prostate cancer. Oncogene 2000;19(10):1288-1296.

23. Serda RE, Adolphi NL, Bisoffi M, Sillerud LO. Targeting and cellular trafficking of magnetic nanoparticles for prostate cancer imaging. Mol Imaging 2007;6(4):277-288.

24. Laidler P, Dulinska J, Lekka M, Lekki J. Expression of prostate specific membrane antigen in androgen-independent prostate cancer cell line PC-3. Arch Biochem Biophys 2005;435(1):1-14.

www.manaraa.com

25. Chang SS, Reuter VE, Heston WD, Hutchinson B, Grauer LS, Gaudin PB. Short term neoadjuvant androgen deprivation therapy does not affect prostate specific membrane antigen expression in prostate tissues. Cancer 2000;88(2):407-415.

26. Raff AB, Gray A, Kast WM. Prostate stem cell antigen: a prospective therapeutic and diagnostic target. Cancer Lett 2009;277(2):126-132.

27. Zhigang Z, Wenlu S. Complete androgen ablation suppresses prostate stem cell antigen (PSCA) mRNA expression in human prostate carcinoma. Prostate 2005;65(4):299-305.

28. Lakhan SE, Sabharanjak S, De A. Endocytosis of glycosylphosphatidylinositol-anchored proteins. J Biomed Sci 2009;16:93.

29. Hong H, Zhang Y, Sun J, Cai W. Positron emission tomography imaging of prostate cancer. Amino Acids 2010;39(1):11-27.

30. Stollman TH, Ruers TJ, Oyen WJ, Boerman OC. New targeted probes for radioimaging of angiogenesis. Methods 2009;48(2):188-192.

31. Schmieder AH, Winter PM, Caruthers SD, Harris TD, Williams TA, Allen JS, Lacy EK, Zhang H, Scott MJ, Hu G, Robertson JD, Wickline SA, Lanza GM. Molecular MR imaging of melanoma angiogenesis with alphanubeta3-targeted paramagnetic nanoparticles. Magn Reson Med 2005;53(3):621-627.

32. Liu Z, Wang F, Chen X. Integrin alpha(v)beta(3)-Targeted Cancer Therapy. Drug Dev Res 2008;69(6):329-339.

33. Almeida TA, Rodriguez Y, Hernandez M, Reyes R, Bello AR. Differential expression of new splice variants of the neurotensin receptor 1 gene in human prostate cancer cell lines. Peptides 2010;31(2):242-247.

34. Carraway RE, Plona AM. Involvement of neurotensin in cancer growth: evidence, mechanisms and development of diagnostic tools. Peptides 2006;27(10):2445-2460.

35. Carraway RE, Hassan S. Neurotensin receptor binding and neurotensin-induced growth signaling in prostate cancer PC3 cells are sensitive to metabolic stress. Regul Pept 2007;141(1-3):140-153.

36. Wang W, Mo ZN. [Advances in prostate-specific membrane antigen targeted therapies for prostate cancer]. Zhonghua Nan Ke Xue 2010;16(6):547-551.

www.manaraa.com

37. Elsasser-Beile U, Buhler P, Wolf P. Targeted therapies for prostate cancer against the prostate specific membrane antigen. Curr Drug Targets 2009;10(2):118-125.

38. Bander NH. Technology insight: monoclonal antibody imaging of prostate cancer. Nat Clin Pract Urol 2006;3(4):216-225.

www.manaraa.com

Chapter 3

Structural and Magnetic Characterization of Superparamagnetic Iron Platinum Nanoparticle Contrast Agents for Magnetic Resonance Imaging

Robert M. Taylor[1], Dale L. Huber[2], Todd C. Monson[3], Victor Esch[4], and Laurel O. Sillerud[1]

[1]University of New Mexico, Department of Biochemistry and Molecular Biology

[2]Sandia National Laboratories, Center for Integrated Nanotechnologies

[3]Sandia National Laboratories, Nanomaterials Sciences Department

[4]nanoMR

Manuscript published in Journal of Vacuum Science and Technology B; 30: Epub, 2012.

www.manaraa.com

Abstract

We report the synthesis, from simple salts, and the physical characterization of superparamagnetic iron platinum nanoparticles (SIPPs) suitable for use as contrast agents in magnetic resonance imaging. The properties of these particles were determined by means of transmission electron microscopy (TEM), thermogravimetric analysis (TGA), inductively coupled plasma-optical emission spectroscopy (ICP-OES), superconducting quantum interference device (SQUID) magnetometry, and nuclear magnetic resonance (NMR) relaxivity at 4.7 Tesla. TEM showed that the diameters of the particles ranged from 9.3 nm to 10 nm, depending on the mole ratio of iron to platinum precursors, and on the concentration of Octadecylamine (ODA) used in their preparation. The iron to platinum stoichiometry determined by ICP-OES varied from 1.4:1 to 3.7:1 and was similarly dependant on the initial mole ratios of iron and platinum salts, as well as on the concentration of ODA in the reaction. SQUID magnetometry showed that the SIPPs were superparamagnetic and had magnetic moments that increased with increasing iron content from 62 to 72 A m^2/kg Fe. The measured relaxivities of the SIPPs at 4.7 Tesla were higher than commercially available superparamagnetic iron oxide nanoparticles (SPIONs), suggesting that these particles may be superior contrast agents in T_2-weighted magnetic resonance imaging (MRI).

www.manaraa.com

Introduction

Ferromagnetic face-centered tetragonal (fct) iron platinum (FePt) nanoparticles have frequently been synthesized, for use in magnetic storage devices, by annealing superparamagnetic iron platinum particles (SIPPs) at elevated temperatures (1-7). The precursor SIPPs have also found a niche as contrast agents in magnetic resonance imaging (MRI) (8-10). Magnetic nanoparticles that cause larger perturbations in the relaxation times of water molecules in close proximity to the particles typically have higher magnetic moments and SIPPs have been reported to have extremely high volume magnetizations between 6 x 10^5 A/m and 1 x 10^6 A/m (10-13). These high volume magnetizations suggest that SIPP syntheses could be optimized to be superior MRI contrast agents. Once developed, biocompatible SIPP contrast agents will also need to go through animal toxicity studies, as this information is not currently available.

Iron pentacarbonyl, $Fe(CO)_5$, is a hazardous reagent that is frequently used in the synthesis of magnetic nanoparticles (4,6,14). We have previously described, along with others, a synthesis method to produce SIPPs that are ~ 9 nm in diameter using simple iron and platinum salts and the ligand Octadecylamine (ODA) as the stabilizing ligand (10,11). This synthesis tends to be a safer and environmentally friendlier method, as it uses less toxic reagents and ODA acts as both the solvent and the ligand, thus reducing the number of reagents needed. Here, we describe the synthesis of SIPPs using different concentrations of the salt precursors and ODA and show that the sizes and

www.manaraa.com

magnetic moments of these particles can be tailored by controlling both the initial mole ratios of the precursor metal salts and the concentration of ODA in the reaction mixture. The SIPPs described here were also refluxed for a shorter duration of time (30 minutes) and heated to a higher temperature (340 °C) than previously reported (10). Furthermore, we describe the physical and magnetic characterization of the nanoparticles resulting from these various syntheses and show that SIPPs are superior T_2-weighted contrast agents for MRI, when compared to superparamagnetic iron oxide nanoparticles (SPIONs).

Experimental

Materials

Iron nitrate nonahydrate ($Fe(NO_3)_3 \cdot 9H_2O$), Platinum (II) acetylacetonate ($Pt(Acac)_2$), and 1-Octadecylamine (ODA) were purchased from Fisher Scientific (Pittsburgh, PA). Nonylphenoxy propenyl polyethylate alcohol (RN-10) was a generous gift from Dai-Ichi Kogyo Seiyaku (Kyoto, Japan). The temperature controller (model 210-J) was purchased from J-KEM Scientific, INC (St. Louis, MO). Heating mantles were purchased from Glas-Col, LLC (Terre Haute, IN) and glassware was purchased from Quark Glass (Vineland, NJ). Superparamagnetic iron oxide nanoparticles (SPIONs) were purchased from Miltenyi Biotec as their μMAC product. All other chemicals and supplies were purchased from common manufacturers.

www.manaraa.com

SIPP Synthesis

Nanoparticles were synthesized using a modification of a procedure due to *Taylor et al. (10)* and *Zhao et al.* (11). For SIPP#1, 1.0 mmol $Fe(NO_3)_3 \cdot 9H_2O$ and 1.0 mmol $Pt(Acac)_2$ were added to 12.5 mmol ODA in a 25 mL 3 neck round bottom flask fitted with a reflux condenser. After the apparatus was assembled, the reaction was heated to 340 °C at a rate of 200 °C/hr. Refluxing at 340 °C was continued for 30 minutes at which point the reaction was removed from the heat and allowed to cool to room temperature. The resulting black particles were collected in hexane and subjected to repeated ethanol washes with centrifugation. SIPP#2 and SIPP#3 were prepared in the same manner as SIPP#1 except 1.0 mmol $Fe(NO_3)_3 \cdot 9H_2O$ and 1.0 mmol $Pt(Acac)_2$ were added to 25.0 mmol ODA for SIPP#2, while 2.0 mmol $Fe(NO_3)_3 \cdot 9H_2O$ and 1.0 mmol $Pt(Acac)_2$ were added to 12.5 mmol ODA for SIPP#3. The SIPPs were resuspended in hexane and stored at room temperature. A typical synthesis as described above produced ~20 mg of SIPPs.

Physical Characterization of SIPPs

Transmission electron microscopy (TEM) was used to determine the size and polydispersity of the particle populations. A drop of the hexane suspension of the SIPPs was applied to carbon-coated grids. After the solvent evaporated, the samples were imaged on a Hitachi 7500 transmission electron microscope with an acceleration voltage of 80 kV. Particle diameters were calculated using ImageJ Software (15). At least 1000 particles were counted and the mean Feret

www.manaraa.com

diameters and standard deviations were calculated. The compositions of the SIPPs were investigated with thermogravimetric analysis (TGA). Aliquots of SIPPs were evaporated in TGA sample cups (Robocasting Enterprises LLC, Albuquerque, NM) and allowed to evaporate. Weight loss profiles were measured with a SDT Q600 TGA/DSC (TA Instruments, New Castle, Delaware) under nitrogen flow. The ODA and FePt content were determined by measuring the mass change while the temperature was raised from room temperature to 1000 °C at a 20 °C/min heating rate. Inductively coupled plasma-optical emission spectroscopy (ICP-OES) was used to measure the metal content and iron to platinum stoichiometry of each synthesis. Prior to analysis, gentle refluxing with nitric and hydrochloric acids digested aliquots of SIPPs. After cooling, the samples were made up to volume, mixed and centrifuged. Samples were then analyzed using a PerkinElmer Optima 5300DV ICP-OES using the recommended wavelengths for each of the analytes. Analysis was performed in an axial mode to improve detection limits. A blank and set of calibration standards were used to establish a three-point calibration curve. Calibration verification samples (ICBV and ICV) were analyzed prior to analyzing the samples. Analyte peaks were examined and peak locations and background points were adjusted for optimum recoveries.

Magnetic Characterization of SIPPs

Superconducting quantum interference device (SQUID) magnetometry was used to measure the blocking temperatures and saturation magnetizations of the

www.manaraa.com

SIPPs. Aliquots (100 µL) of the hexane suspension of SIPPs were placed in 5 mm, economy 8-inch NMR tubes (Wilmad LabGlass, Vinelanad NJ, USA) and allowed to evaporate overnight. Magnetic measurements were made on a Quantum Design MPMS-7 SQUID magnetometer. Temperature sweeps between 0 and 400 K were performed by zero-field cooling the sample and then measuring the magnetic moment as a function of temperature under the influence of a weak magnetic field (1 mT) during warming and subsequent cooling. This procedure yields both a zero-field-cooled (ZFC) and field-cooled (FC) curve, respectively. Values of the blocking temperature (T_B) were recorded by determining the peak location in each ZFC curve. Saturation magnetizations were measured at human body temperature (310 K) by varying the applied field from -5 to 5 Tesla. Mass magnetizations were calculated with the known iron concentrations determined with ICP-OES. The iron to platinum ratio, determined with ICP-OES, was used to calculate the density of an fcc unit cell representing the naked SIPPs without ODA ligand. The weight percent of ODA on the particles, measured with TGA, was used with the density calculated for naked SIPPs to estimate the density of ODA coated SIPPs. Volume magnetizations were calculated using this calculated density for ODA coated SIPPs.

Magnetic Resonance Imaging and Relaxivities

Increasing concentrations of SIPPs (0.02 to 0.3 mM iron) or SPIONs (0.1 to 0.62 mM iron) were added to 1% agarose in 2.0 mL self-standing micro-centrifuge tubes (Corning, Corning, NY). Samples were imaged on a 4.7 Tesla Bruker

www.manaraa.com

Biospin (Billerica, MA) MRI system with Paravision 4.0 software. Samples were imaged with a 512 x 256 matrix, a variable TE, and TR = 10 sec. T_1 measurements were acquired by inversion-recovery with 15 interpulse delays. Spin- and gradient echo sequences were used to measure T_2, and T_2*, respectively. The MRI samples were then digested as above for ICP-OES and the iron concentration was determined. The relaxation rates, R_n, (= $1/T_n$) were calculated and plotted *versus* the ICP-OES-determined iron concentration of each sample. Linear regression was used to fit the data and the relaxivity (r_n) of each SIPP synthesis is given as the slope of the resulting line in units of Hz/mM Fe.

Results and Discussion

SIPPs were synthesized using two different mole ratios of iron to platinum precursors, and with two different amounts of ODA. Table 3.1 outlines the general synthetic parameters used for each of the three SIPP syntheses that we report. We began by producing SIPPs using a 1:1 mole ratio of the metal salt precursors and 12.5 mmol of ODA (SIPP#1).

Table 3.1 The parameters used in the synthesis of SIPPs.

Sample	Molar Ratio[a]	ODA (mmol)
SIPP#1	1	12.5
SIPP#2	1	25.0
SIPP#3	2	12.5

[a] Molar ratio of $Fe(NO_3)_3\ 9H_2O$:$Pt(Acac)_2$

www.manaraa.com

Since iron provides the magnetism for these nanoparticles, we expected that increasing the amount of iron precursor would generate SIPPs with a greater Fe:Pt mole ratio and thus a higher magnetic moment. For this reason, we also synthesized SIPPs with a 2:1 mole ratio of iron to platinum, while keeping the amount of ODA at 12.5 mmol (SIPP#3). Additionally, we expected that the amount of ODA in the reaction mixture would effect the formation and final characteristics of the SIPPs. To explore this possibility, we synthesized SIPPs with a 1:1 molar ratio of iron to platinum and increased the amount of ODA to 25.0 mmol (SIPP#2). TEM images of particles from each SIPP synthesis are shown in Figure 3.1. From the TEM images, it is seen that the nanoparticles are roughly spherical in shape. Using ImageJ software[9] to analyze the TEM images, we found that the SIPPs had average diameters that ranged from 9.3 ± 1.9 nm (SIPP#1) to 10 ± 3.4 nm (SIPP#3). This finding suggested that as the mole ratio of iron added to the reaction was increased, the size of the particles increased slightly. In addition, the size of the particles also increased as the concentration of ODA was increased in the reaction. To understand these trends, we used ICP-OES to determine the composition of the SIPPs and found that the iron to platinum stoichiometry increased with increasing iron precursor and ODA. Also of note, is that the polydispersity of the SIPPs increased with increasing size and Fe:Pt stoichiometry, as was evident by the increase in the standard deviation in the diameter describing the size distribution of the particles. Table 3.2 summarizes the physical and magnetic characteristics of the three SIPP

www.manaraa.com

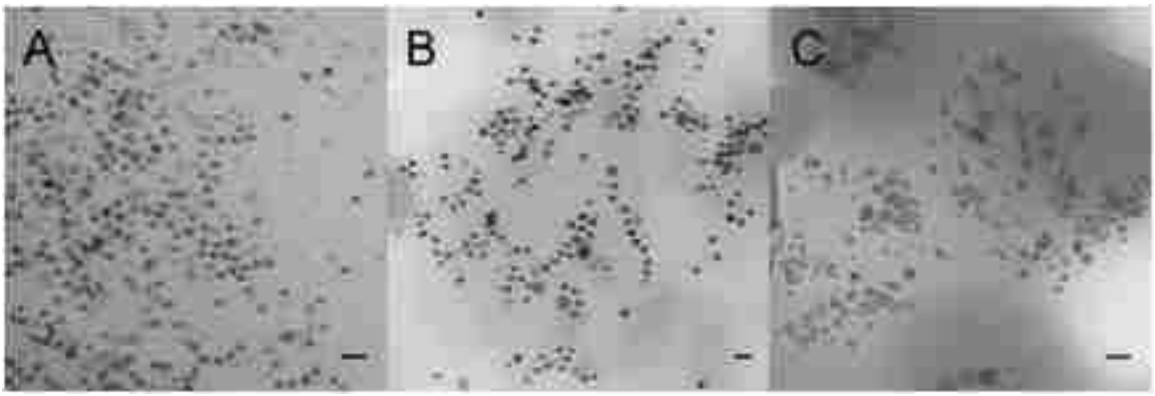

Figure 3.1 Images of SIPPs acquired using transmission electron microscopy. Drops of SIPPs were applied to carbon-coated grids and the samples were imaged at an acceleration voltage of 80 kV. (A) SIPP#1, (B) SIPP#2, (C) SIPP#3. Scale bars = 20 nm.

www.manaraa.com

Table 3.2 Physical and magnetic characteristics of SIPPs and SPIONs.

	Variable	Units	SIPP#1	SIPP#2	SIPP#3	SPIONs[a]
R	Fe:Pt ratio	---	1.44	2.35	3.67	---
D	Diameter of particle	nm	9.28	9.98	10.03	50[b]
σ	Standard deviation in diameter	nm	1.94	2.90	3.43	---
ρ	Density	g/cm^3	5.2	5.2	5.2	2.5[c]
M	Mass of iron per particle	pg	1.5×10^{-6}	2.2×10^{-6}	2.6×10^{-6}	1.6×10^{-5}
C_{Fe}	Fe concentration of solution	g/mL	1.2×10^{-3}	1.9×10^{-3}	2.8×10^{-2}	2.7×10^{-4} [c]
C_p	Particle concentration	Particles/mL	8×10^{14}	9×10^{14}	1×10^{16}	2×10^{14} [c]
T_b	Blocking temperature	Kelvin	170	210	195	155[c]
K	Effective anisotropy energy	J/m^3	1.4×10^5	1.4×10^5	1.3×10^5	1.2×10^5 [c,d]
μ_M	Mass magnetization	A m^2/kg Fe	61.7	69.2	71.8	82.0[c]
μ_V	Volume magnetization	A/m	7.4×10^5	7.4×10^5	6.8×10^5	2.0×10^5

[a] MACS® iron oxide particles from Miltenyi Biotec
[b] Hydrodynamic diameter according to manufacturer
[c] Taylor et al. (10)
[d] Calculated using a magnetic core diameter of 10 nm

www.manaraa.com

syntheses, compared with commercially available SPIONs. It is clear that the amount of ODA plays an important role in the formation of the FePt alloy and the resultant iron to platinum stoichiometry. Zhao *et al.* (11) previously suggested that an excess of ODA was needed in this particular synthetic method and that the initial decomposition of the iron and platinum salts led to three possible products; pure iron, iron oxides, or FePt nanoparticles. The excess ODA is thought to react with the iron oxides, forming an intermediate, $Fe(ODA)_3$ complex (11). The catalytic activity of the FePt nanoparticles then provides a pathway available to the pure iron. It appears that by increasing the amount of ODA to 25.0 mmol, twice the amount previously used (10,11), that more iron is deposited into the FePt alloy.

To further investigate the composition of the SIPPs, TGA was used to remove the organic layer on the particles and determine the weight percents of ODA and naked FePt. The TGA data for SIPP#1 is shown in Figure 3.2. ODA has a boiling point around 347 °C and, therefore, we suggest that the pronounced weight loss seen from ~ 300 to 400 °C is due to the removal of ODA from the SIPP surface. It is plausible that some of this weight loss could also be due to iron oxides in the samples. The thermal decomposition of naked SPIONs has been reported to occur from 300 to 400 °C (16). This overlap in the thermal decomposition temperatures of the ODA and iron oxides make it difficult to determine from the TGA data what percentage of the weight loss may or may not be due to iron oxide contaminants in the SIPPs. The TGA results suggest that the organic layer comprised approximately 20% of the particle mass, much less

www.manaraa.com

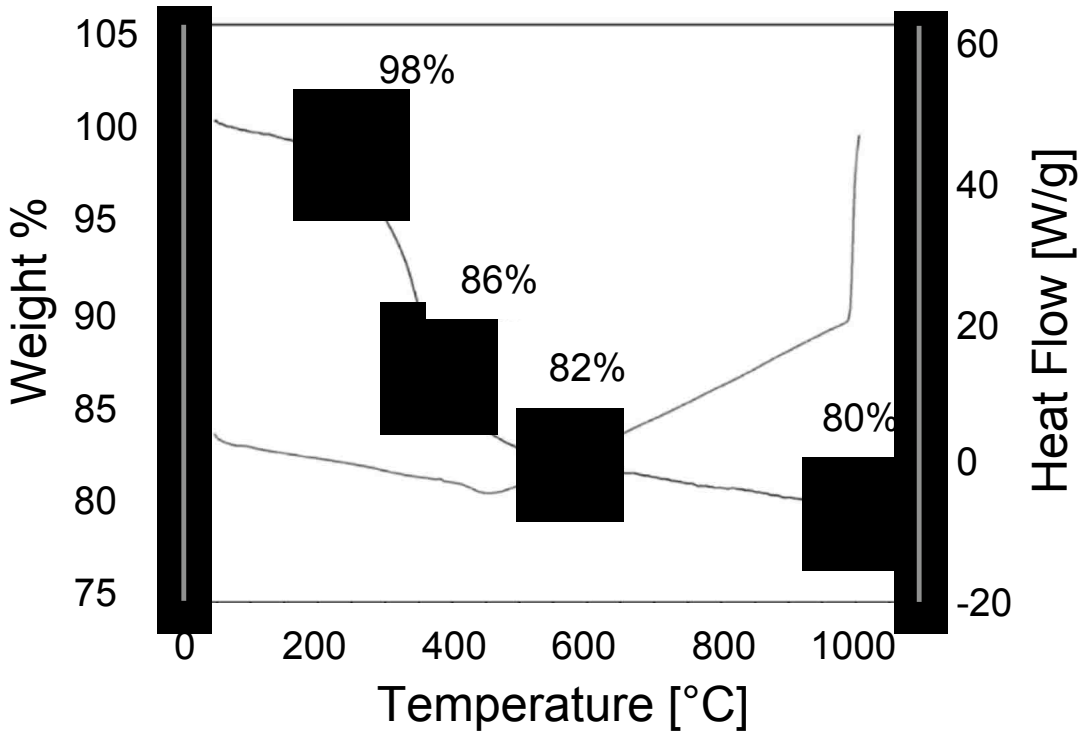

Figure 3.2 Weight loss and heat flow curves for SIPP#1. Dried SIPPs were added to TGA sample cups and heated at 20 °C/hr from room temperature to 1000 °C. The weight percent of organic coating and naked FePt was then extrapolated. The curve labeled with arrows shows the decrease in weight percent while the unlabeled curve shows the heat flow.

www.manaraa.com

than previously reported with lower temperature preparations that used increased reaction times (10,11). All of the syntheses showed similar decomposition curves and indicated that the SIPPS were between 18% and 22% ODA by mass.

We expected that increasing the concentration of iron per SIPP by increasing the mole ratio of iron to platinum in the reaction mixture would lead to a higher magnetic moment simply due to the larger amount of magnetic iron that would be present in each particle. We therefore determined the magnetic characteristics of the various SIPP syntheses using SQUID magnetometry. Figure 3.3 shows the mass magnetization as a function of the applied magnetic field for the three SIPP syntheses. In agreement with our expectations, both the mass magnetization and the volume magnetization increased with increasing iron content from SIPP#1 to SIPP#2. Once the iron to platinum ratio increased above 3.5, though, the volume magnetization began to decrease, while the mass magnetization continued to increase. We calculated the anisotropy of each SIPP synthesis based on the blocking temperature measured by SQUID magnetometry. The relationship between the anisotropy and the blocking temperature (K) is

(1)

where k is Boltzmann's constant, T_B is the blocking temperature of the individual SIPP synthesis, and V is the volume of a single particle in units of cm^3. The constant 25 is calculated using a relaxation time of 1 x 10^{-9} seconds and a measurement time of 100 seconds. Table 3.2 shows that the anisotropy remained fairly constant for all of the SIPP syntheses. This did not support the

www.manaraa.com

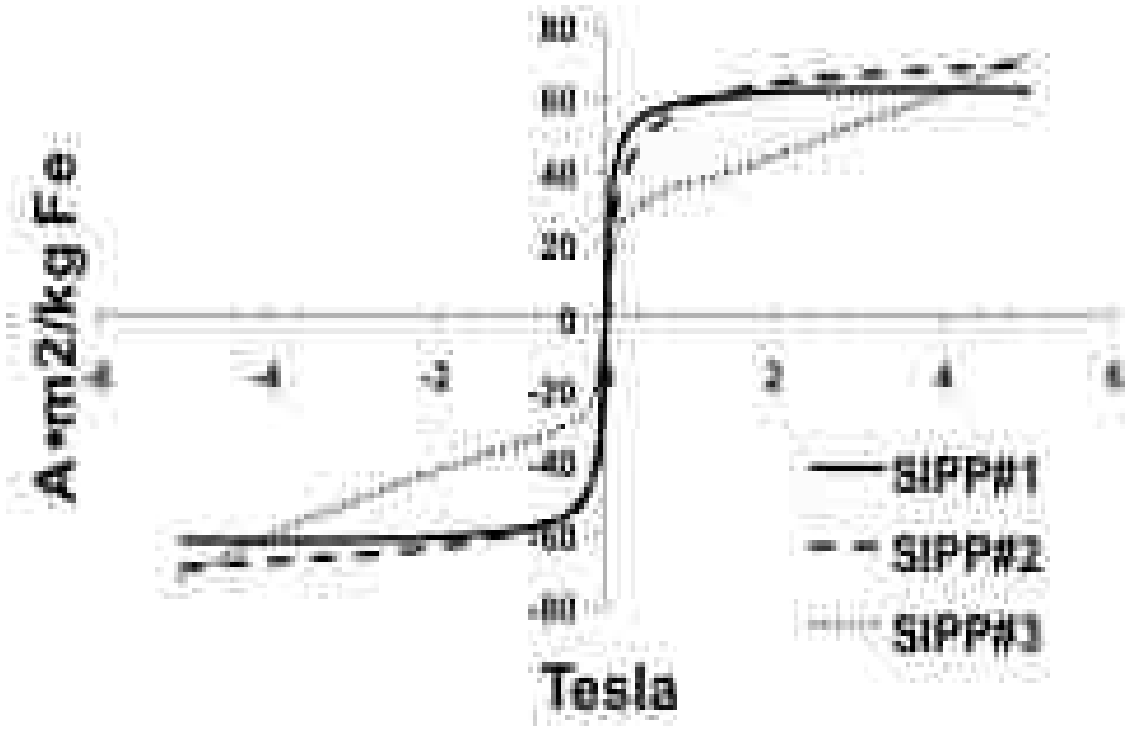

Figure 3.3 Mass magnetization of SIPPs measured using SQUID and ICP. 100 µL aliquots of SIPPs were evaporated in constricted NMR tubes and sealed. SQUID magnetometry data was collected at 310 Kelvin from -5 to 5 Tesla. Also, 100 µL aliquots of SIPPs were added to conical tubes and analyzed with ICP to determine the mass of iron in each SQUID sample. The solid line is for SIPP#1, the long dashed line is for SIPP#2, and the dotted line is for SIPP#3.

www.manaraa.com

idea that magnetic order increases with iron content. The effective anisotropy constants of the synthesized nanoparticles are in good agreement with magnetocrystalline anisotropy constants for SIPPs previously reported (8,17). Further studies using high-resolution TEM and X-ray diffraction methods may be able to increase our understanding of any crystalline differences in the SIPPs synthesized.

Finally, to test whether the SIPPs could be beneficial as MRI contrast agents, we chose to examine SIPP#2, since it had intermediate stoichiometry, size, and magnetic properties compared to the other SIPPs. Relaxivities were measured at 4.7 Tesla for SIPP#2 and compared with relaxivities of ~50 nm μMACs® (Miltenyi Biotec, Carlsbad, CA) SPIONs, also measured at 4.7 Tesla. We first imaged the μMAC particles using TEM and measured their magnetization using SQUID magnetometry.(10) Figure 3.4 shows a representative TEM image of the μMACs SPIONs showing a mean magnetic core diameter of ~20 nm, although the hydrodynamic diameters may be larger due to the fact that coatings on the particles are not visible using TEM. The manufacturer suggests that these dextran-coated SPIONs are 50 nm in diameter but that the magnetic cores are ~ 10 nm. This suggests that although the hydrodynamic diameter is larger for the SPIONs compared to the SIPPs, the magnetic cores are similar in size and, therefore, the SIPP and SPION magnetic properties can be compared. Table 3.2 summarizes our characterizations of the μMAC particles using TEM, SQUID, and ICP-OES. It is clear that the volume magnetization of the SPIONs is ~ 3.5 fold less than determined for our SIPPs. Next, we prepared μMAC relaxivity samples

www.manaraa.com

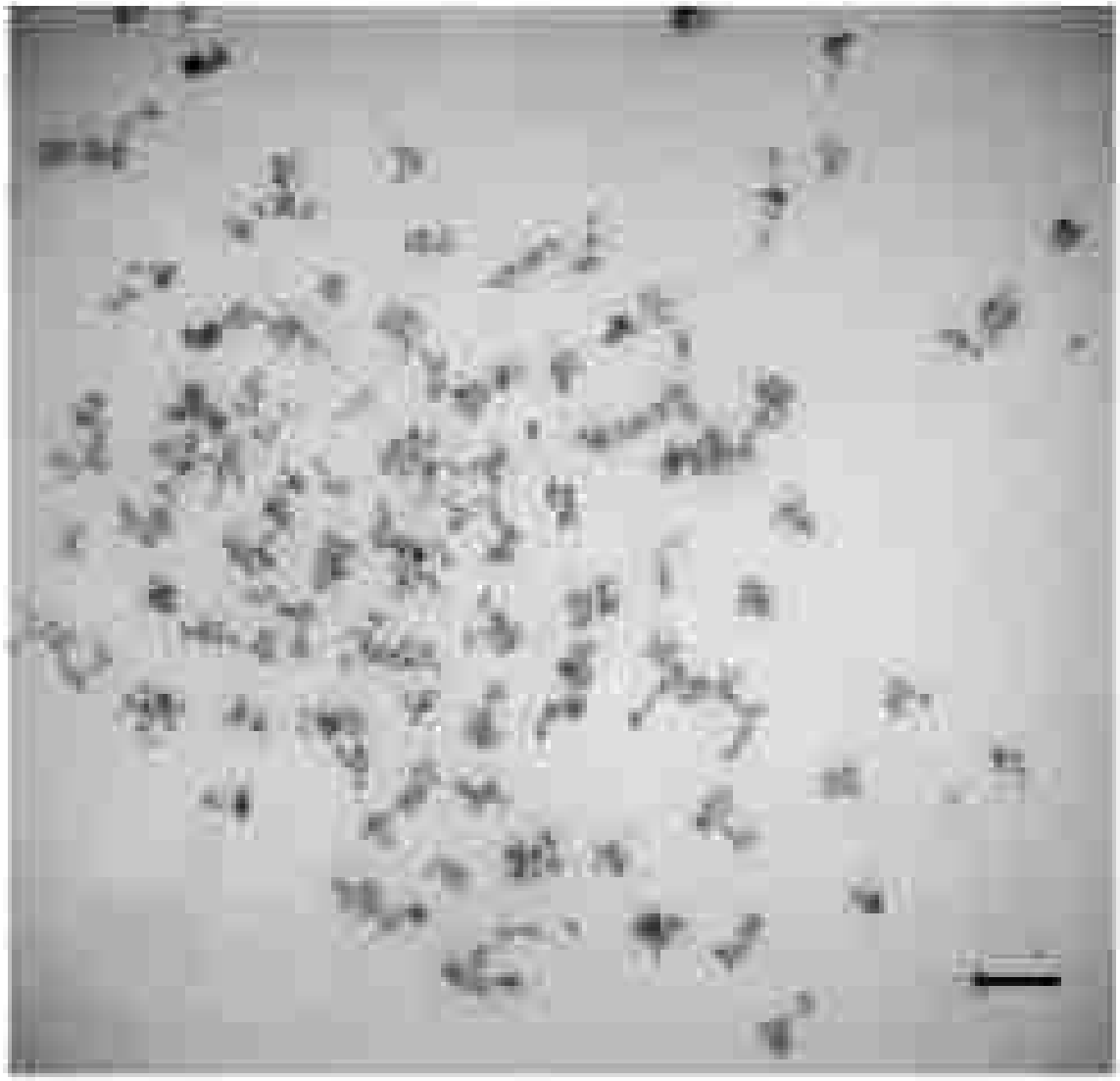

Figure 3.4 Image of μMAC SPIONs acquired using transmission electron microscopy. A drop of μMAC SPIONs was applied to a carbon-coated grid. The sample was imaged at an acceleration voltage of 80 kV. Scale bar = 50 nm.

www.manaraa.com

by adding increasing amounts of SPIONs to 1 % agarose (10). We also prepared SIPP#2 relaxivity samples by first magnetically separating the SIPPs and then suspending the particles in the initial volume of a strong surfactant, RN-10, to disperse the hydrophobic SIPPs in the aqueous agarose. Increasing amounts of the RN-10 stabilized SIPPs were then added to 1 % agarose in plastic sample tubes. Table 3.3 shows the relaxivities measured at 4.7 Tesla, while Figure 3.5 shows the longitudinal and transverse relaxation rates of the SIPPs and SPIONs as a function of iron concentration. It is apparent that the SIPPs have a 3 fold

Table 3.3 SIPP and SPION relaxivities measured at 4.7 Tesla

Variable	Unit	SPION[a]	SIPP#2
r_1	Hz/mM Fe	1.67[b]	1.18
r_2	Hz/mM Fe	21.37[b]	62.2
r_2^*	Hz/mM Fe	436[b]	253
r_2/r_1	---	13[b]	53

[a] MACS® iron oxide particles from Miltenyi Biotec
[b] Taylor et al.(10)

higher r_2 than the μMAC SPIONs and more than a 4-fold increase in the r_2/r_1 ratio. The higher measured r_2/r_1 ratio would be favorable for a T_2-lowering MRI contrast agent. The SIPP#2 sample had a lower mass magnetization compared with the μMAC SPIONs, yet a much larger volume magnetization of approximately 7.4 x 10^5 A/m. This volume magnetization is in good agreement with previously reported volume magnetizations of SIPPs (between 6 x 10^5 A/m and 1 x 10^6 A/m) (11-13). Our result is novel, though, in that we have used safer methods, less reagents, and different temperatures to synthesize the particles for an MRI application. This difference in the volume magnetizations for the SPIONs and SIPPs may be due to the fact that the SPIONs are encapsulated in dextran

www.manaraa.com

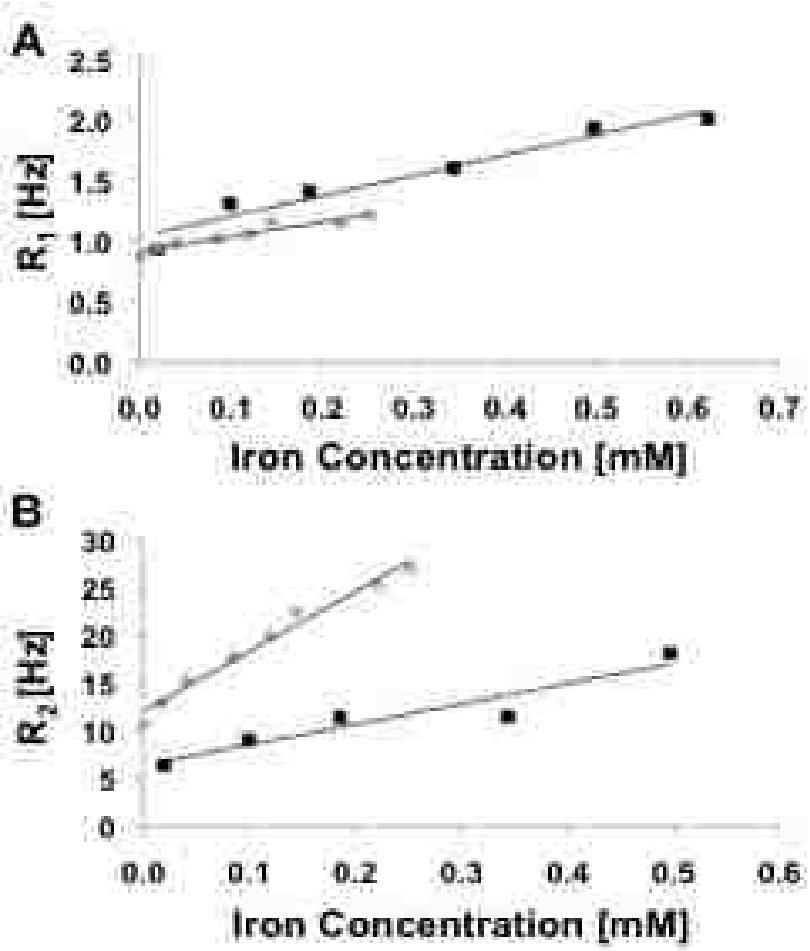

Figure 3.5 A comparison of SIPP and SPION relaxivities measured at 4.7 Tesla. Increasing concentrations of particles were added to 1% agarose and scanned at 4.7 Tesla with TR = 10 sec and TE = 40 ms. R_1 and R_2 values were calculated by taking the inverse of the T_1 and T_2 relaxation times. The relaxation rates (R_1 and R_2) were then plotted versus the iron concentration (mM Fe), measured using ICP-OES. The slope of the linear regression is the relaxivity of the specific particle at 4.7 Tesla. Squares = SPIONs and Circles = SIPPs. (A) longitudinal relaxation rates (B) transverse relaxation rates.

www.manaraa.com

and the SIPPs are stabilized with the strong surfactant, RN-10. It is possible that the dextran coating decreases the relaxivities of the particles by preventing the necessary close approach of water molecules. A current focus in our lab is to encapsulate the SIPPs in phospholipids and again measure the relaxivities of these particles compared with SPIONs (10). Overall, our data suggest that SIPPs can be tailored to optimize size and magnetic properties. In addition, SIPPs may be superior contrast agents in T_2-weighted imaging when compared to SPIONs.

Summary and Conclusions

Synthesis of SIPPs, from low-toxicity precursors, was performed producing spherical particles in the range of 9.3 nm to 10 nm. The synthesized SIPPs showed increasing size and increasing iron to platinum stoichiometry when the molar concentration of iron precursor increased and when the amount of ODA was increased. The TGA results suggested that the particles were 80% naked FePt and 20% organic ligand, by mass. The saturation magnetization of the particles increased with increasing iron concentration, as measured with SQUID magnetometry. Further studies are needed to elucidate the mechanism of initial FePt nucleation and the crystalline and stability changes as the Fe to Pt stoichiometry is increased. The synthesized SIPPs showed increased r_2 and r_2/r_1 when compared with SPIONs, suggesting that SIPPs may be superior contrast agents for T_2-weighted MRI. Only limited cytotoxicity studies have been reported for SIPPs and have focused on non-encapsulated SIPPs (18). Silica encapsulated SIPPs have also been reported (19) but, to our knowledge, the

www.manaraa.com

cytotoxicity of encapsulated SIPPs has not been established. Determining the cytotoxicity of encapsulated SIPPs would be an important future endeavor.

Acknowledgments

This research was supported in part by funding from NIH (5RO1CA123194 to Laurel O. Sillerud), the NCI New Mexico Cancer Nanotechnology Training Center (NIH R25CA153825 supporting Robert M. Taylor), and by nanoMR, Inc. (Victor Esch). Portions of this work were performed at the Center for Integrated Nanotechnologies, a US Department of Energy, Office of Basic Energy Sciences, user facility. Sandia National Laboratories is a multi-program laboratory operated by The Sandia Corporation, a Lockheed-Martin Company, for the US Department of Energy under Contract No. DE-AC04-94AL85000. MRI relaxivities were measured at the BRaIN Imaging Center, Albuquerque, NM. We gratefully acknowledge the assistance of Dr. Medhi Ali of the Earth and Planetary Sciences Department at UNM, for the ICP-OES analyses, and of Dr. Stephen Jett of the UNM Electron Microscopy Facility.

www.manaraa.com

References

1. Han L, Wiedwald U, Kuerbanjiang B, Ziemann P. Fe oxidation versus Pt segregation in FePt nanoparticles and thin films. Nanotechnology 2009;20(28):285706.

2. Antoniak C, Lindner J, Spasova M, Sudfeld D, Acet M, Farle M, Fauth K, Wiedwald U, Boyen HG, Ziemann P, Wilhelm F, Rogalev A, Sun S. Enhanced orbital magnetism in Fe(50)Pt(50) nanoparticles. Phys Rev Lett 2006;97(11):117201.

3. Antoniak C, Lindner J, Spasova M, Sudfeld D, Acet M, Farle M, Fauth K, Wiedwald U, Boyen HG, Ziemann P, Wilhelm F, Rogalev A, Sun S. Enhanced orbital magnetism in Fe(50)Pt(50) nanoparticles. Phys Rev Lett 2006;97(11):117201-117201 to 117201-117204.

4. Sun S, Murray CB, Weller D, Folks L, Moser A. Monodisperse FePt nanoparticles and ferromagnetic FePt nanocrystal superlattices. Science 2000;287(5460):1989-1992.

5. Kim JR, C.; Liu, P.; Sun, S. Dispersible Ferromagnetic FePt Nanoparticles. Adv Mater 2009;21:906-909.

6. Sun S. Recent Advances in Chemical Synthesis, Self-Assembly, and Applications of FePt Nanoparticles. Adv Mater 2006;18:403.

7. Varanda LC, Jafelicci M, Jr. Self-assembled FePt nanocrystals with large coercivity: reduction of the fcc-to-L1(0) ordering temperature. J Am Chem Soc 2006;128(34):11062-11066.

8. Maenosono S, Suzuki T, Saita S. Superparamagnetic FePt nanoparticles as excellent MRI contrast agents. J Magn Magn Mater 2008;320:l..79-l.83.

9. Morales MP, Bedard MF, Roca AG, Presa P, Hernando A, Zhang F, Zanella M, Zahoor AA, Sukhorukov GB, del Mercato LL, Parak WJ. Relaxation times of colloidal iron platinum in polymer matrixes. J Mater Chem 2009;19:6381-6386.

10. Taylor RM, Huber DL, Monson TC, Ali AM, Bisoffi M, Sillerud LO. Multifunctional iron platinum stealth immunomicelles: targeted detection of human prostate cancer cells using both fluorescence and magnetic resonance imaging. J Nanopart Res 2011;13(10):4717-4729.

11. Zhao F, Rutherford M, Grisham SY, Peng X. Formation of monodisperse FePt alloy nanocrystals using air-stable precursors: fatty acids as alloying

www.manaraa.com

mediator and reductant for Fe3+ precursors. J Am Chem Soc 2009;131(14):5350-5358.

12. Zeng H, Li J, Liu JP, Wang ZL, Sun S. Exchange-coupled nanocomposite magnets by nanoparticle self-assembly. Nature 2002;420(6914):395-398.

13. Xu C, Yuan Z, Kohler N, Kim J, Chung MA, Sun S. FePt nanoparticles as an Fe reservoir for controlled Fe release and tumor inhibition. J Am Chem Soc 2009;131(42):15346-15351.

14. Inomata K, Sawa T, Hashimoto S. Effect of large boron additions to magnetically hard Fe-Pt alloys. J Appl Phys 1988;64(5):2537-2540.

15. Rasband WS. ImageJ. US National Institutes of Health, Betesda, Maryland, USA, http//rsbinfonihgov/ij/ 1997-2009.

16. Shan Z, Yang W, Zhang X, Huang Q, Ye H. Preparation and Characterization of Carboxyl-Group Functionalized Superparamagnetic Nanoparticles and the Potential for Bio-Applications. J Braz Chem Soc 2007;18(7):1329-1335.

17. Salgueirino-Maceira V, Liz-Marzan LM, Farle M. Water-based ferrofluids from FexPt1-x nanoparticles synthesized in organic media. Langmuir 2004;20(16):6946-6950.

18. Maenosono S, Yoshida R, Saita S. Evaluation of genotoxicity of amine-terminated water-dispersible FePt nanoparticles in the Ames test and in vitro chromosomal aberration test. J Toxicol Sci 2009;34(3):349-354.

19. Aslam M, Fu L, Li S, Dravid VP. Silica encapsulation and magnetic properties of FePt nanoparticles. J Colloid Interface Sci 2005;290(2):444-449.

20. Artemov D, Mori N, Ravi R, Bhujwalla ZM. Magnetic resonance molecular imaging of the HER-2/neu receptor. Cancer Res 2003;63(11):2723-2727.

21. Artemov D, Mori N, Okollie B, Bhujwalla ZM. MR molecular imaging of the Her-2/neu receptor in breast cancer cells using targeted iron oxide nanoparticles. Magn Reson Med 2003;49(3):403-408.

www.manaraa.com

Chapter 4

Multifunctional Iron Platinum Stealth Immunomicelles: Targeted Detection of Human Prostate Cancer Cells Using Both Fluorescence and Magnetic Resonance Imaging

Robert M. Taylor[a,*], Dale L. Huber[b], Todd C. Monson[c], Abdul-Mehdi S. Ali[d], Marco Bisoffi[a], and Laurel O. Sillerud[a]

[a]*Department of Biochemistry and Molecular Biology, University of New Mexico*

[b]*Center for Integrated Nanotechnologies, Sandia National Laboratories*

[c]*Nanomaterials Sciences Department, Sandia National Laboratories*

[d]*Department of Earth and Planetary Sciences, University of New Mexico,*

Manuscript published in Journal of Nanoparticle Research; 13(10): 4717-4729, 2011.

www.manaraa.com

Abstract

Superparamagnetic iron oxide nanoparticles (SPIONs) are the most common type of contrast agents used in contrast agent-enhanced magnetic resonance imaging (MRI). Still, there is a great deal of room for improvement, and nanoparticles with increased MRI relaxivities are needed in order to increase the contrast enhancement in MRI applied to various medical conditions including cancer. We report the synthesis of superparamagnetic iron platinum nanoparticles (SIPPs) and subsequent encapsulation using PEGylated phospholipids to create stealth immunomicelles (DSPE-SIPPs) that can be specifically targeted to human prostate cancer cell lines and detected using both MRI and fluorescence imaging. SIPP cores and DSPE-SIPPs were 8.5 nm ± 1.6 nm and 42.9 nm ± 8.2 nm in diameter and the SIPPs had a magnetic moment of 120 A m^2/kg iron. J591, a monoclonal antibody against prostate specific membrane antigen (PSMA), was conjugated to the DSPE-SIPPs (J591-DSPE-SIPPs) and specific targeting of J591-DSPE-SIPPs to PSMA-expressing human prostate cancer cell lines was demonstrated using fluorescence confocal microscopy. The transverse relaxivity of the DSPE-SIPPs, measured at 4.7 Tesla, was 300.6 ± 8.5 s^{-1} mM^{-1}, which is 13-fold better than commercially available SPIONs (23.8 ± 6.9 s^{-1} mM^{-1}) and ~ 3-fold better than reported relaxivities for Feridex® and Resovist®. Our data suggest that J591-DSPE-SIPPs specifically target human prostate cancer cells *in vitro*, are superior contrast agents in T_2-weighted MRI, and can be detected using fluorescence imaging. To our knowledge, this is the first report on the synthesis of

www.manaraa.com

multifunctional SIPP micelles and using SIPPs for the specific detection of prostate cancer.

Introduction

In the United States, prostate cancer is the second most common reason for cancer death in men (1). Accurate detection methods are important for all aspects of the clinical management of prostate cancer, including diagnosis, risk assessment, staging, and prognosis. Such methods will result in individualized and efficacious treatments for patients at risk for prostate cancer or for its progression. Many of these tasks are currently managed by determination of the serum biomarker prostate specific antigen (PSA). For example, serum PSA levels are used to evaluate prostate cancer risk and progression, and justify confirmatory biopsies to diagnose the presence of malignancy. However, biopsies have inherent risks such as bleeding and infection (2), and cancer is not detected (false negative cases) in 30-50% of biopsies in patients with subsequently confirmed malignancy due to small and inconspicuous lesions (3). Another major issue is that ~25% - 40% of patients are over diagnosed using current detection methods leading to superfluous biopsies (2). These findings indicate that detection and staging of prostate cancer needs to be improved. Novel magnetic resonance molecular imaging methods promise to markedly increase the specificity of prostate tumor detection (4).

Our goal is to develop targeted magnetic resonance imaging (MRI) agents for the specific detection of prostate cancer. A unifying theme in the development

www.manaraa.com

of novel imaging and therapeutic modalities in recent years has been specifically targeting these agents to cells of interest (5). The targeting motifs are often antibodies against antigens expressed on cancerous cells but not healthy cells. The most promising target antigen expressed specifically on prostate cancer cells is prostate specific membrane antigen (PSMA), which is most strongly expressed in the prostate and expression has been found to increase as tumor grade and stage increases (6). Additionally, many nonprostatic tumors have been found to express PSMA in the neovasculature, but expression in healthy vasculature has not been reported (7,8), suggesting that PSMA may also be a general tumor antigen that could be used to detect numerous types of solid tumors. Thus, antibodies against PSMA are an appealing choice for use as targeting motifs for prostate cancer.

Superparamagnetic iron oxide nanoparticles (SPIONs) are the most common type of contrast agents used in contrast agent-enhanced MRI (9). Although SPIONs cause negative contrast in the MR images, the signal enhancement is still lower than other common imaging techniques (10). Therefore, novel nanoparticles with increased MRI relaxivities are needed in order to increase the signal enhancement in MRI and the detection of cancer, using lower doses of the contrast agents. Iron platinum (FePt) particles have been the focus of intense research in recent years due to their high magnetic anisotropy and high stability (11-15). Much of the interest in FePt has been placed on producing ferromagnetic face-centered tetragonal (fct) FePt particles, for use in magnetic storage devices, by annealing superparamagnetic face-

www.manaraa.com

centered cubic (fcc) nanoparticles at temperatures exceeding 500 °C (15-18). However, fcc superparamagnetic iron platinum particles (SIPPs) are of interest by themselves due to their possible use as contrast agents in MRI (19-21). For superparamagnetic MRI contrast agents, it is thought that a higher magnetic moment at a given magnetic field causes larger perturbations in the magnetic relaxation times of nearby water protons and, thus, higher moment particles should generate increased image contrast. SIPPs have previously been reported with volume magnetizations greater than 590 emu/cm^3 (6 x 10^5 A/m), with some preparations approaching 1,140 emu/cm^3 (1 x 10^6 A/m), the saturation magnetization of bulk FePt (22-25). These reported high magnetic moments suggested that SIPPs would be superior MRI contrast agents.

One obvious drawback to the synthesis of various types of nanoparticles is that toxic precursors are generally used to produce the particles (14,15,26). Often, iron pentacarbonyl, $Fe(CO)_5$, a very hazardous reagent (27), is used as the iron precursor in FePt syntheses (15). A number of different FePt syntheses are described by Sun (14). Recently, Zhao et al. (23) described a method for producing ~11 nm SIPPs using the hydrophobic surface ligand 1-Octadecylamine (ODA) along with iron and platinum salts that are much less hazardous than $Fe(CO)_5$. We report the synthesis of SIPP cores using modifications of this less hazardous method. In order to use hydrophobic core nanoparticles *in vivo*, the particles must first be made biocompatible. A plethora of methods for encapsulating drugs and hydrophobic imaging agents, to instill biocompatibility, have been reported and include encapsulation using hydrophilic or amphiphilic

www.manaraa.com

components such as monomers and phospholipids (28). Additionally, polyethylene glycol (PEG) groups on nanoparticles have been shown to increase solubility and circulation times and decrease immunogenicity (28,29). This decrease in immunogenicity imparts the nanoparticles with stealth capability *in vivo*. Furthermore, biocompatible contrast agents that also incorporate a fluorescent component offer the advantage of *in vivo* and *ex vivo* imaging using small animal fluorescence imagers and/or fluorescence microscopy for *in vivo* biodistribution studies and *in vitro* binding assays. Here, we describe the physical and magnetic characterization of SIPP cores encapsulated with a mixture of 1,2-distearoyl-sn-glycero-3-phosphoethanolamine-N-[amino(polyethylene glycol)-2000] (DSPE-PEG), DSPE-PEG with biotin conjugated to the head group (biotin-DSPE-PEG), 1,2-dimyristoyl-sn-glycero-3-phosphoethanolamine-N-[lissamine rhodamine B sulfonyl] (Liss-Rhod), and subsequent conjugation to a monoclonal antibody (J591) against PSMA (J591-DSPE-SIPPs). We also demonstrate the specific binding of J591-DSPE-SIPPs to PSMA-positive prostate cancer cells using confocal microscopy and measure the MR relaxivities of the DSPE-SIPPs at 4.7 Tesla. Compared to commercially available and clinically used SPIONs, the J591-DSPE-SIPPs are superior contrast agents in T_2-weighted MRI, specifically target PSMA-positive human prostate cancer cells, and can be detected with fluorescence microscopy. To our knowledge, this is the first report on the synthesis of multifunctional SIPP micelles and the first report of using SIPPs for the specific detection of prostate cancer cells.

www.manaraa.com

Experimental Details

Materials

Iron nitrate nonahydrate ($Fe(NO_3)_3 \cdot 9H_2O$), Platinum (II) acetylacetonate ($Pt(Acac)_2$), and ODA were purchased from Fisher Scientific (Pittsburgh, PA). Temperature controller (model 210-J) was purchased from J-KEM Scientific, INC (St. Louis, MO). Heating mantle was purchased from Glas-Col, LLC (Terre Haute, IN) and glassware was purchased from Quark Glass (Vineland, NJ). The phospholipids 1,2-distearoyl-sn-glycero-3-phosphoethanolamine-N-[amino(polyethylene glycol)-2000] (DSPE-PEG), DSPE-PEG with biotin conjugated to the head group (biotin-DSPE-PEG), and 1,2-dimyristoyl-sn-glycero-3-phosphoethanolamine-N-[lissamine rhodamine B sulfonyl] (Liss-Rhod) were purchased from Avanti Polar Lipids (Alabaster, AL). SPIONs were purchased from Miltenyi Biotec (Carlsbad, CA) as their MACS® Streptavidin MicroBeads product. RPMI cell culture media, fetal bovine serum, and Penicillin-Streptomycin Solution were purchased from Sigma (St. Louis, MO). All other chemicals and supplies were purchased from common manufacturers.

Synthesis of SIPP Cores

Nanoparticles were synthesized using a modification of a procedure due to Zhao et al. (23). Briefly, 1.0 mmol $Fe(NO_3)_3 \cdot 9H_2O$ and 1.0 mmol $Pt(Acac)_2$ were added to 12.5 mmol ODA in a 25 mL 3-neck round bottom flask fitted with a reflux condenser. The reaction was heated to 330 °C (200 °C/hr) with 10 °C

www.manaraa.com

recirculated cooling in the reflux condenser. Refluxing was continued for 45 minutes at which point the reaction was removed from the heat and allowed to cool to room temperature. The resulting black particles were collected in hexane and subjected to repeated washing by collecting particles in conical tubes with an external magnet, removing the supernatant, and resuspending in hexane.

Encapsulation of SIPP Cores

Phospholipid-encapsulated SIPP cores (DSPE-SIPPs) were prepared using a thin film method. 1.5 mL of SIPP cores (1.4% solids) in hexane was added to a 20.0 mL glass scintillation vial. A chloroform mixture of (56:1:1 mole ratio) DSPE-PEG, biotin-DSPE-PEG, and Liss-Rhod was then added to the SIPP cores. The mixture was further diluted in 1.5 mL of hexane and vortexed thoroughly. The vial was wrapped in aluminum foil and allowed to evaporate in the dark in a chemical fume hood overnight to produce a thin film. 5.0 mL of double-distilled water was heated to 67 °C and added to the thin film. Hydration of the thin film was then continued in a 67 °C water bath for 1.0 hour with vortexing every 15 minutes to produce liposomes containing SIPP cores. The liposomes were then extruded at 67 °C through an 80 nm nuclepore track-etch membrane filter using a mini-extruder (Avanti Polar Lipids, Alabaster, AL) to produce ~ 45 nm DSPE-SIPP micelles. The DSPE-SIPPs were then purified from SIPP-free micelles and excess phospholipids by collecting the magnetic particles using an LS magnetic column placed in a VarioMACS™ magnetic separator (Miltenyi Biotec, Carlsbad, CA). After the non-magnetic material had

www.manaraa.com

passed through the column, 8.0 mL of double-distilled water was added to the top of the column to wash the particles. The washing was then repeated a second time. The column was removed from the magnet and placed in a tube rack with a 2.0 mL glass vial placed underneath the column. 2.0 mL of either double-distilled water or phosphate buffered saline (PBS), pH 7.4, was used to elute the purified DSPE-SIPPs from the column.

Physical Characterization of SIPP Cores and DSPE-SIPPs

Transmission electron microscopy (TEM) was used to determine the size and polydispersity of the particle populations. For SIPP cores, a drop of the hexane suspension was applied to a carbon-coated grid and dried. For DSPE-SIPPs, a drop of the aqueous suspension was applied to a carbon-coated grid, dried for 10 minutes, and the excess was absorbed using a kimwipe. Adding a drop of 2% Uranyl Acetate solution followed by a 2-minute drying period negatively stained the grid. The excess was removed and the grid was allowed to dry for at least 5 minutes. The samples were imaged on a Hitachi 7500 transmission electron microscope with an acceleration voltage of 80 kV. Particle diameters were calculated using ImageJ Software (30). At least 1000 particles were counted and the mean Feret diameters and standard deviations were calculated. Diameters of the DSPE-SIPPs were additionally measured using Dynamic Light Scattering (DLS) with a Microtrac Nanotrac^{TM} Ultra DLS (Microtrac, Largo, FL). The compositions of the SIPPs, phospholipids, and DSPE-SIPPs were investigated with thermogravimetric analysis (TGA). Aliquots of ODA, SIPP cores,

www.manaraa.com

phospholipids, or DSPE-SIPPs were placed in the TGA sample cup and evaporated at 30 °C under an argon stream for at least 90 minutes until all solvent had been removed and the mass of the sample stabilized. Weight loss profiles were then measured with a Pyris™ 1 thermogravimetric analyzer (PerkinElmer, Waltham, MA) under argon flow. The ODA, phospholipid, and SIPP content were determined by measuring the mass loss profile while the temperature was raised from 30 °C to 1000 °C at a 10 °C/min ramp rate. Inductively coupled plasma-optical emission spectroscopy (ICP-OES) was used to measure the metal content and iron to platinum ratio of each synthesis. Prior to analysis, aliquots of the particles were digested at 180 °C with nitric and hydrochloric acids in a PDS-6 Pressure Digestion System (Loftfields Analytical Solutions, Neu Eichenberg, Germany). After cooling, the samples were made up to a known volume, mixed and centrifuged. Samples were then analyzed using a PerkinElmer Optima 5300DV ICP-OES. The recommended wavelengths for each of the analytes were used and analysis was performed in an axial mode to improve detection limits. A blank and set of calibration standards were used to establish a three-point calibration curve. Calibration and instrument verification samples were analyzed before and after analyzing the samples, as well as periodically throughout the measurements. Analyte peaks were examined and peak identification and background points were adjusted for optimum recoveries.

www.manaraa.com

Magnetic Characterization of SIPP Cores and DSPE-SIPPs

Superconducting quantum interference device (SQUID) magnetometry was used to measure the blocking temperatures of the SIPP cores, DSPE-SIPPs, and MACS® SPIONs and saturation magnetizations of the SIPPs and MACS® SPIONs. An aliquot (100 µL) of the samples were applied to the end of cotton Qtips® (Unilever, Englewood Cliffs, NJ). Magnetic measurements were then made on a Quantum Design MPMS-7 SQUID magnetometer. Temperature sweeps between 0 and 310 K were performed by zero-field cooling the sample and then measuring the magnetic moment as a function of temperature under the influence of a weak magnetic field (1 mT) during warming and subsequent cooling. This procedure yields both a zero-field-cooled (ZFC) and field-cooled (FC) curve, respectively. Values of the blocking temperature ( ) were recorded by determining the peak location in each ZFC curve. Saturation magnetizations were measured at 310 K (37 °C) by varying the applied field from -5 to 5 Tesla. Mass magnetizations were calculated from the known iron concentrations determined by ICP-OES.

Magnetic Resonance Relaxometry

Increasing concentrations of SPIONs (0.08 to 0.48 mM iron) or DSPE-SIPPs (0.04 to 0.20 mM iron) were added to 1% agarose in 2.0 mL self-standing micro-centrifuge tubes (Corning, Corning, NY). Samples were imaged on a 4.7 Tesla Bruker Biospin (Billerica, MA) MRI system with Paravision 4.0 software. Samples were imaged with a 256 x 256 matrix, a variable TE, and TR = 10 sec.

www.manaraa.com

T_1 measurements were acquired by inversion-recovery with 15 interpulse delays. Spin- and gradient echo sequences were used to measure T_2, and T_2*, respectively. The MRI samples were then digested as above and the iron concentration was determined with ICP-OES. The relaxation rates, [redacted], were calculated and plotted *versus* the ICP-OES-determined iron concentration of each sample. Linear regression was used to fit the data and the relaxivity ([redacted]) of each sample is given as the slope of the resulting line in units of s^{-1} mM^{-1} of iron.

Antibody Conjugation, Cell Culture, and Confocal Binding Assay

Humanized monoclonal antibody against PSMA (J591) (purchased from Neal Bander, Cornell College of Medicine) and polyclonal goat anti-rabbit IgG (Sigma, St. Louis, MO) were conjugated to streptavidin in an overnight reaction using a Lightning-Link™ Streptavidin Conjugation Kit (Innova Biosciences, Cambridge, UK) according to the manufacturers' instructions. Concentrations of streptavidin, antibodies, and streptavidin-antibody conjugates were quantitated using a NanoDrop™ 2000 Spectrophotometer (Wilmington, DE). Streptavidin-conjugated antibodies (~30 μg) were then incubated with DSPE-SIPPs (100 μg iron) overnight at 4 °C to conjugate the antibodies to the DSPE-SIPPs through the biotin groups of the biotin-DSPE-PEG. A Micro BCA™ Protein Assay (Thermo Scientific, Rockford, IL) was used to quantitate the antibody concentrations and the amount of antibody conjugated to the DSPE-SIPP surface using a BioSpec-mini Spectrophotometer (Shimadzu, Columbia, MD) at a wavelength of 562 nm. 20,000 C4-2 or PC-3 human prostate cancer cells in RPMI media containing 10%

www.manaraa.com

fetal bovine serum and 100 U/mL Penicillin-Streptomycin solution were seeded onto polylysine-coated cover slips in 6-well polystyrene plates (Corning, Corning, NY) and incubated at 37 °C, 5% CO_2 for 24 hours. The media was then exchanged with media containing J591-DSPE-SIPPs (20 µg iron), IgG-DSPE-SIPPs (20 µg iron), or PBS (20 µL). The cells were incubated with the particles for 10 minutes at 37 °C, 5% CO_2 and the media was then aspirated and 5.0 mL PBS was added to wash unbound particles away from the cells. Washing was repeated 3 times. Cover slips were mounted on slides containing a drop of ProLong® Gold Antifade Reagent with DAPI (Invitrogen, Eugene, OR). Confocal Images were acquired using a 60X oil objective with an Olympus IX-81 inverted spinning disk confocal microscope. Cells were also imaged by light microscopy, using a Zeiss Axiovert 25 CA inverted light microscope with a 63X phase-contrast objective.

Results and Discussion

SIPP cores and DSPE-SIPPs were prepared as described in the Experimental Details section. Figure 4.1 shows TEM images of the SIPP cores and DSPE-SIPPs. The TEM images indicate that both the SIPP cores and the DSPE-SIPPs are spherical in shape. Using ImageJ software to analyze TEM images of the SIPP cores and DSPE-SIPPs, we measured average diameters of 8.5 nm ± 1.6 nm and 44.2 nm ± 13.1 nm, respectively. DLS was also employed to measure the size of the DSPE-SIPPs and revealed diameters of 42.9 nm ± 8.2 nm, showing good agreement with the diameters measured with the TEM

www.manaraa.com

images. We also used ImageJ to analyze the number of SIPP cores per DSPE-SIPP. We analyzed 175 DSPE-SIPPs and found that there were 7.2 ± 6.8 SIPP cores per DSPE-SIPP. The TEM images suggest that the number of SIPP cores

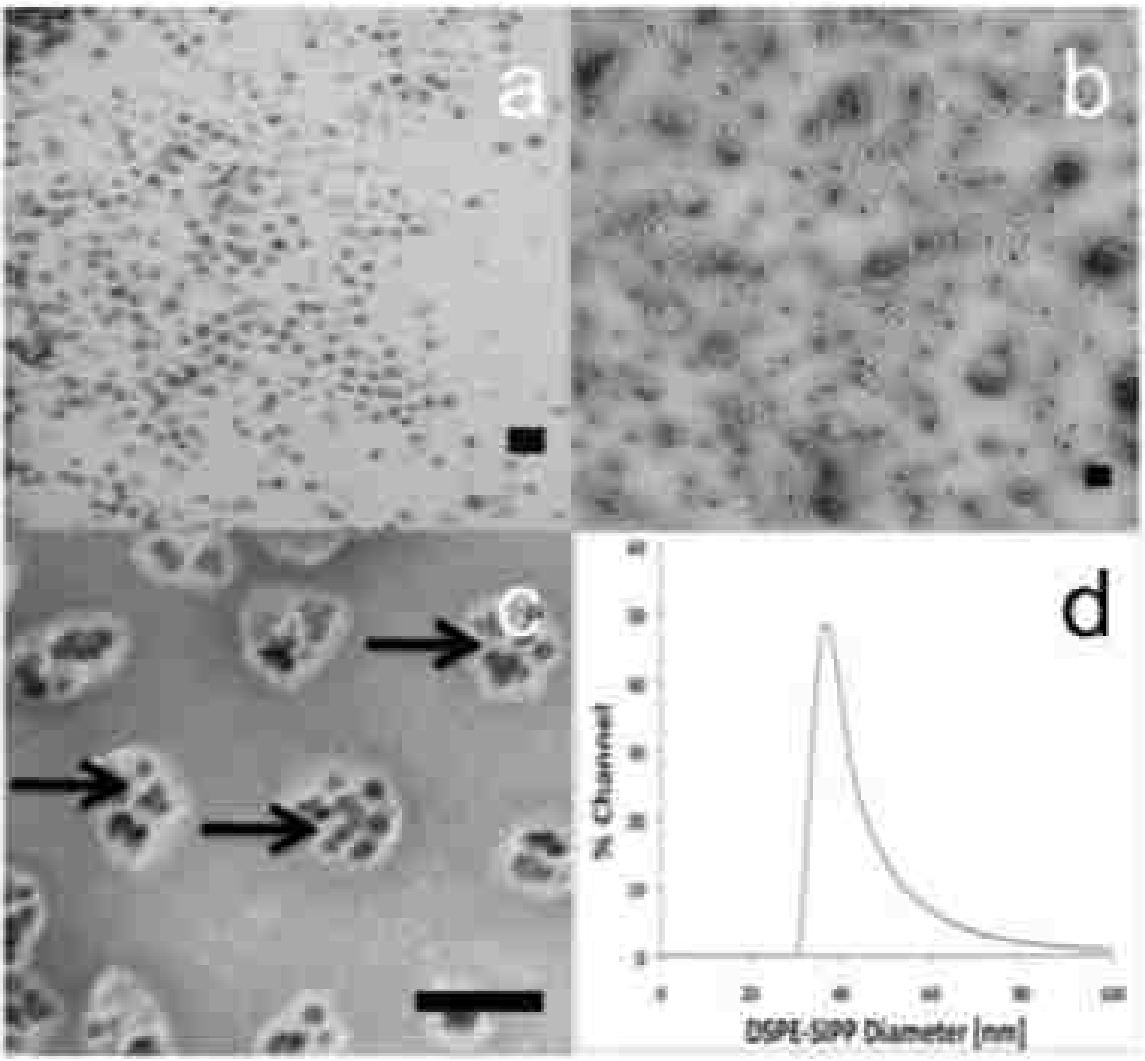

Figure 4.1 TEM and DLS of SIPP Cores and DSPE-SIPPs. TEM images of (a) SIPP cores and (b, c) DSPE-SIPPs. Scale bars are 20 nm, 50 nm, and 50 nm, respectively. Arrows denote internal areas of the DSPE-SIPPs where space can be seen between the hydrophobic SIPP cores. (d) DLS of DSPE-SIPPs in PBS.

www.manaraa.com

per DSPE-SIPP is quite variable even though the overall encapsulated population is quite monodisperse, as is evident from the DLS and TEM size distribution data. Considering that the SIPP cores were found to be 8.5 nm in diameter, 5 SIPP cores would encompass a diameter of 42.5 nm, which is approximately the diameter of the DSPE-SIPPs (42.9 nm) and, on average, the greatest number of SIPP cores we observed spanning the diameter of the DSPE-SIPPs in the TEM images. This suggests that the DSPE-SIPPs do not contain an inner aqueous layer characteristic of a liposome, but rather have a purely hydrophobic inner layer that contains the hydrophobic SIPP cores. DSPE-PEG phospholipid bilayers are reported to be ~ 5.0 nm in thickness (31). It is extremely unlikely that an 8.5 nm hydrophobic SIPP core would fit into a 5 nm bilayer. Moreover, the TEM images in Figure 4.1 show that there is space in between the hydrophobic SIPP cores in the inner layer of some of the DSPE-SIPPs. It is very unlikely that water would reside at this boundary between hydrophobic phospholipid tail and hydrophobic ODA on the SIPP core surface. Therefore, we suggest that the DSPE-SIPPs are not liposomes, but rather micellar contrast agents. Johnsson and Edwards (2003) analyzed particles prepared with increasing concentrations of DSPE and DSPE-PEG and found that concentrations >33 mole % DSPE-PEG resulted in micelle formation rather than liposomes. Our DSPE-SIPPs are prepared with ~ 98 mole % DSPE-PEG, and although liposomes and micelles reported by Johnsson and Edwards (2003) did not contain an additional hydrophobic superparamagnetic nanoparticle at the core, their results support the idea of micelle formation in our system. To

www.manaraa.com

investigate the stability of the DSPE-SIPP micelles, we also used TEM to image the DSPE-SIPPs up to 21 days post-synthesis. The particles were stored in PBS, pH 7.4 at 4 °C. The TEM images revealed no physical changes up to 12 days post-synthesis, at which point the DSPE-SIPPs began to merge and aggregate into larger particles (data not shown).

To investigate the composition of the SIPPs w e used ICP-OES and measured an iron to platinum ratio (Fe:Pt) of 1.24:1 for the SIPP cores. The encapsulation process did not appear to significantly affect the Fe:Pt stoichiometry. To further investigate the composition of the SIPPs and DSPE-SIPPs, TGA was used to thermally decompose the particles and determine the weight percents of ODA, phospholipid, SIPP core, and naked FePt. The thermograms of ODA, SIPPs, phospholipids, and DSPE-SIPPs are shown in Figure 4.2. ODA has a boiling point around 314 °C and both ODA and the SIPP core samples show pronounced weight loss from ~ 180 °C to 375 °C due to the removal of ODA from the SIPP surface. The hump in the middle of the curve in Figure 4.2A suggests the SIPP decomposition is a two-step process. It is possible that a portion of the ODA is not bound, but rather entrapped and being removed from the particles before the bound fraction. The TGA results suggest that the organic ODA layer comprised approximately 72% of the SIPP core mass and indicated that the SIPPs were 28% naked FePt by mass. The phospholipid and DSPE-SIPP samples showed similar weight loss profiles and continued to lose mass up to ~ 400 °C. The DSPE-SIPP thermogram revealed that the phospholipids comprised ~ 55% of the DSPE-SIPP mass, while SIPP cores

www.manaraa.com

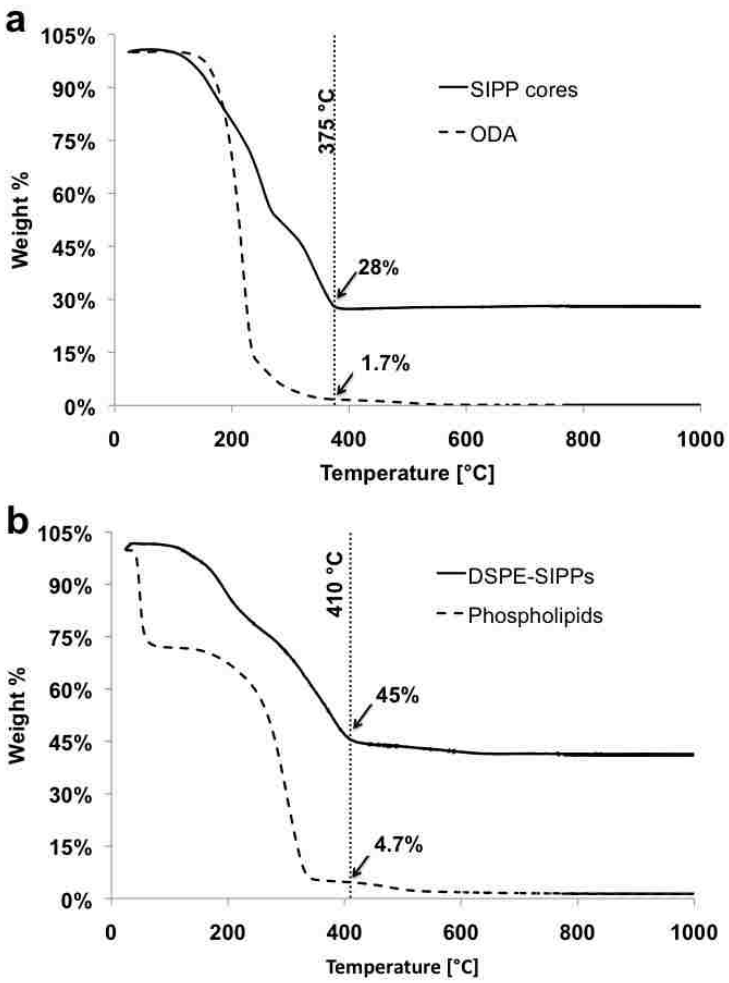

Figure 4.2 SIPP Core and DSPE-SIPP TGA. TGA thermograms of (a) SIPP cores (solid curve) and ODA (dashed curve) and (b) DSPE-SIPPs (solid curve) and phospholipids (dashed curve). Vertical dashed line denotes the temperature, reported to the left of the dashed line, at which the (a) SIPP cores and (b) DSPE-SIPPs stopped loosing significant mass. % values are the percent mass of each sample remaining at the temperature denoted by the vertical dashed line.

www.manaraa.com

made up the remaining ~ 45% of the DSPE-SIPP mass. The mass reduction seen in the thermogram of phospholipids (prepared in chloroform) at ~ 65 °C is likely due to release of residual chloroform which has a boiling point of 61.2 °C.

To characterize the magnetic properties of the SIPP cores and DSPE-SIPPs, we used SQUID magnetometry. Figure 4.3 shows the mass magnetization as a function of the applied magnetic field for the SIPP cores. Blank Qtips® were also scanned as controls but did not have any measureable effect in the SQUID (data not shown). The mass magnetization of the SIPP cores was 120 A m^2/kg Fe. As a comparison, we also measured commercially available SPIONs (~50 nm MACS® MicroBeads, Miltenyi Biotec) that we have previously used as an MRI contrast agent (32). The SPIONs had a mass magnetization of 82 A m^2/kg Fe, which is 1.5-fold lower than the SIPPs. SQUID magnetometry was also used to measure the blocking temperatures of the SIPPs (Figure 4.3), DSPE-SIPPs, and SPIONs, which were 210 K, 180-210 K, and 155 K (-63 °C, -93 to -63 °C, and -118 °C), respectively. All of these blocking temperatures are below body temperature and no hysteresis is seen in the magnetization curves confirming the SIPPs, DSPE-SIPPs, and SPIONs are superparamagnetic for biological applications. The broad blocking transition observed upon lipid encapsulation of the SIPPs is likely caused by the varying environments of the nanoparticles within the micelle, which alters the effective anisotropy energy of the particles. It has been shown that packing multiple magnetic cores into a single particle alters the measured anisotropy of the particles (33). Next, we calculated the effective anisotropy of the SIPPs and

www.manaraa.com

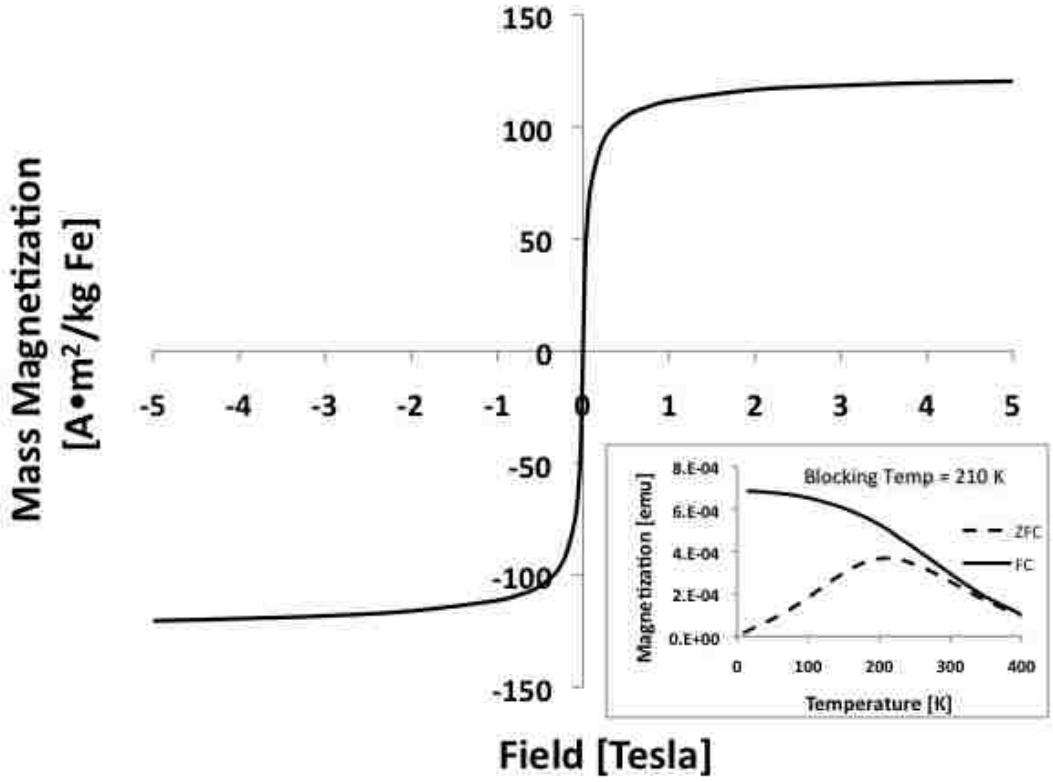

Figure 4.3 Magnetization of SIPPs. Saturation magnetization curves for the mass magnetization of SIPP cores versus the applied magnetic field from -5 to 5 Tesla. Inset shows the zero-field-cooled (ZFC) and field-cooled (FC) curves. Values of the blocking temperature (T_B) were recorded by determining the peak location in the ZFC curve.

www.manaraa.com

SPIONs based on the blocking temperatures. The relationship between the effective anisotropy energy and the blocking temperature is [redacted], where [redacted] is Boltzmann's constant, T_B is the blocking temperature, and V is the volume of the magnetic core in units of m^3. The constant 25 is calculated using a relaxation time of 1 x 10^{-9} seconds and a measurement time of 100 seconds. Table 4.1 summarizes the physical and magnetic characteristics of the SIPP cores, DSPE-SIPPs, and SPIONs and shows that the SIPPs effective anisotropy energy is ~ 2-fold greater than for the SPIONs. The effective anisotropy constants for the SIPPs and SPIONs are in excellent agreement with anisotropy constants for SIPP cores (21,35) and SPIONs (36,37) previously reported.

The DSPE-SIPPs are prepared from a 56:1:1 mole ratio of DSPE-PEG, biotin-DSPE-PEG, and Liss-Rhod, respectively. The biotin-labeled phospholipid allowed us to conjugate streptavidin-labeled J591 to the DSPE-SIPPs. We measured ~ 2 streptavidin per J591 antibody and after conjugation, we calculated ~ 6 J591 antibodies per J591-DSPE-SIPP. DSPE-SIPPs were also conjugated to rabbit IgG antibodies as a non-targeted control (IgG-DSPE-SIPPs). We also measured ~2 streptavidin per IgG antibody, but ~ 12 IgG antibodies were measured per DSPE-SIPP. To determine if our J591-DSPE-SIPPs could specifically target PSMA-expressing human prostate cancer cell lines, we incubated the J591-DSPE-SIPPs and IgG-DSPE-SIPPs with C4-2 and PC-3 human prostate cancer cells grown on polylysine-coated cover slips. C4-2 cells were used as our PSMA-positive cell line. C4-2 is an androgen-deprivation therapy resistant cell line that over-expresses PSMA (38,39). PC-3 cells were

www.manaraa.com

Table 4.1	Physical and Magnetic Characterizations of SIPPs, DSPE-SIPPs, and MACS®				
Symbol	**Variable**	**Units**	**SIPP Cores**	**DSPE-SIPPs**	**MACS®**
D	Mean Diameter	nm	8.5	42.9	[a]50
σ	Standard Deviation of Diameter	nm	1.6	8.2	---
S	Weight % Solids	%	1.4	1.1	1.0
ρ	Density	g/cm^3	5.2	2.5	2.5
R	Fe:Pt Ratio	---	1.24	1.27	---
C_{Fe}	Iron Concentration of Solution	g/mL	1×10^{-3}	5×10^{-5}	3×10^{-4}
C	Concentration of Particles	Particles/mL	3×10^{16}	3×10^{14}	2×10^{14}
T_B	Blocking Temperature	K	210	180 - 210	155
K	Effective Anisotropy Energy	J/m^3	2.5×10^5	2.5×10^5	[b]1.2×10^5
μ_M	Mass Magnetization	$A \cdot m^2/kg$ Fe	120	---	82

[a] Hydrodynamic diameter according to manufacturer and (34)

[b] Calculated using a magnetic core diameter of 10 nm (34)

www.manaraa.com

used as a PSMA-negative cell line. PC-3 cells originate from a bone metastasis, are androgen-deprivation therapy resistant, and do not express or only minimally express PSMA (39,40). Figure 4.4 shows the confocal microscopy images of C4-2 and PC-3 cells incubated with PBS (mock), J591-DSPE-SIPPs, and IgG-DSPE-SIPPs. Since the stealth immunomicelles are made with 1 mole % Liss Rhod, the particles fluoresce red in the confocal images. Both C4-2 and PC-3 cells lacked red fluorescence in the mock samples. Also, both cell lines only show minimal non-specific or IgG-specific uptake of the IgG-DSPE-SIPPs (non targeting control). The PSMA-negative cell line, PC-3, also only showed minimal non-specific or IgG-specific uptake of the J591-DSPE-SIPPs. The amount of non-specific J591-DSPE-SIPP uptake in the PC-3 cells appears to be comparable to the non-specific uptake of the IgG-DSPE-SIPPs. In stark contrast to the other images, significant uptake of the J591-DSPE-SIPPs can be seen in the C4-2, PSMA-positive cell line. Clearly, J591-DSPE-SIPPs are internalized only by the C4-2 cell line with only minimal non-specific pick up by the PC-3 cell line and only minimal non-specific pick up when IgG-DSPE-SIPPs were used. The confocal data demonstrates the successful targeting of the multifunctional DSPE-SIPPs and detection of PSMA-expressing human prostate cancer cells *in vitro* with no, or minimal, non-specific binding to cell lines that do not express PSMA.

Finally, to test whether the DSPE-SIPPs could be beneficial as MRI contrast agents, we measured the longitudinal (), transverse (), and T_2-star

www.manaraa.com

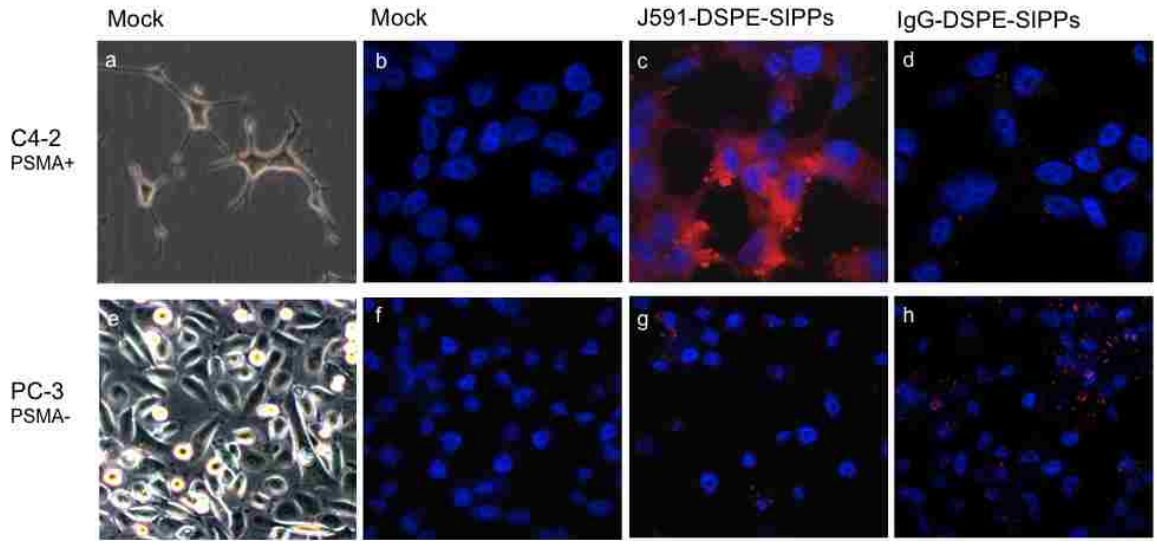

Figure 4.4 Specific Detection of PSMA-expressing Prostate Cancer Cells using J591-DSPE-SIPPs. C4-2 (top row), PSMA-positive, and PC-3 (bottom row), PSMA-negative, cell lines were imaged using phase-contrast light microscopy with a 63X objective (a, e). Cells were incubated for 10 minutes with either PBS (Mock) (b,f), J591-DSPE-SIPPs (c, g), or IgG-DSPE-SIPPs (d, h) and imaged using confocal microscopy with a 60X oil objective. Blue = DAPI nuclear stain and Red = Liss Rhod incorporated in the DSPE-SIPPs

www.manaraa.com

([redacted]) relaxation rates of the DSPE-SIPPs and commercially available SPIONs. Table 4.2 shows the relaxivities measured at 4.7 Tesla, while Figure 4.5 shows

Table 4.2 MR Relaxivities of DSPE-SIPPs and MACS® MicroBeads at 4.7 Tesla[a]

Sample	r_1	r_2	r_2^*	r_2/r_1
DSPE-SIPPs	17	300	831	18
MACS® MicroBeads	2	23	436	12

[a] Relaxivities are reported as s^{-1} mM^{-1}

the T_2-weighted MR image of the DSPE-SIPP agarose samples, as well as the transverse relaxation rates of the DSPE-SIPPs and SPIONs as a function of iron concentration. It is apparent that the DSPE-SIPPs have an ~ 13-fold higher [redacted] than the SPIONs, a measure of the particles ability to create negative contrast in the MR images, and a 1.5-fold increase in the r_2/r_1 ratio. As expected, the SIPPs had increased magnetizations compared with the SPIONs and far superior transverse relaxivities. Since the commercially available SPIONs had such low transverse relaxivities, we also compared relaxivities of the DSPE-SIPPs with relaxivities of the clinically used SPION contrast agents Feridex® and Resovist® that are reported in the literature (21,41-44). Table 4.3 shows the comparison of the relaxivities at 4.7 Tesla for the DSPE-SIPPs, Feridex®, and Resovist®. Compared to Feridex® and Resovist®, the DSPE-SIPPs produce superior negative contrast enhancement in MRI, as is evident from the 1.6- to 3-fold

www.manaraa.com

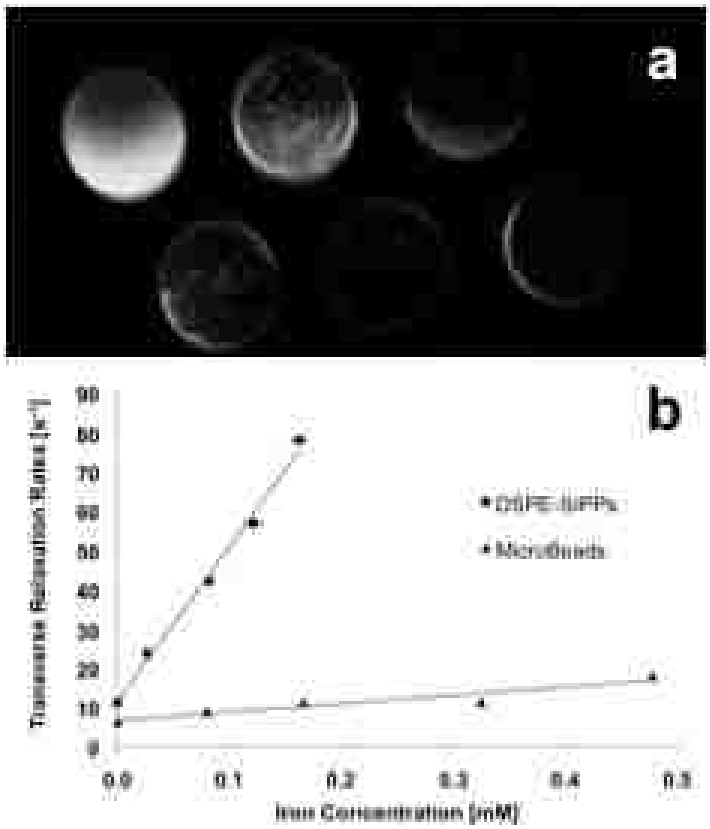

Figure 4.5 Magnetic Resonance Relaxometry of DSPE-SIPPs and MACS® MicroBeads at 4.7 Tesla. (a) T_2-weighted MRI of 1% agarose samples containing increasing concentrations of DSPE-SIPPs. Top left sample is agarose that did not contain DSPE-SIPPs. The other samples have increasing concentrations of DSPE-SIPPs going from left to right in the top row images and continuing from left to right in the lower row images. (b) Transverse relaxation rates (Hz) versus iron concentration (mM) for the DSPE-SIPPs (squares) and MACS® MicroBeads (triangles). Linear regression was used to fit the data (solid lines) and the transverse relaxivities (r_2) of the DSPE-SIPPs and MACS® MicroBead SPIONs, given as the slope of the resulting line, were 300.8 ± 8.5 s^{-1} $mM^{-1}$and 23.8 ± 6.9 s^{-1} mM^{-1}, respectively.

www.manaraa.com

Table 4.3 Contrast Agent Relaxivity Comparison at 4.7 Tesla[a]

Contrast Agent	Coating	Phantom	Diameter [nm]	r_1	r_2	r_2*	r_2/r_1	Reference
DSPE-SIPPs	Phospholipid	1% Agarose	42.9	17	300	831	18	Our Data
Feridex®	Dextran	2% Agarose	80-150[b]	---	148	215	---	(41)
Feridex®	Dextran	2% Agarose	80-150[b]	---	---	240	---	(44)
Feridex®	Dextran	2% Agarose	80-150[b]	2.5[c]	100[c]	---	33.3	(43)
Feridex®	Dextran	Water	80-150[b]	40	160	---	4.0	(21)
Feridex®	Dextran	Water	80-150[b]	2.3	105	---	45.7	(42)
Resovist®	Carbodextran	1% Agarose	60[b]	2.8	176	---	62.9	(42)
Resovist®	Carbodextran	Water	60[b]	19.4	186	---	9.6	(21)

[a] Relaxivities are reported as s^{-1} mM^{-1}
[b] (45)
[c] Relaxivities are estimated at 200 MHz from the graphs in the supplemental materials

www.manaraa.com

higher [redacted]. Overall, our data suggest that J591-DSPE-SIPPs are stable, superparamagnetic, specifically target PSMA-positive human prostate cancer cells, useful for fluorescence detection for *in vitro* binding applications, and superior contrast agents in T_2-weighted imaging when compared to both commercially available and clinically used SPIONs *in vitro*.

Summary and Conclusions

In 2009, more than 200,000 men were newly diagnosed with and over ~30,000 men died due to prostate cancer in the United States, making carcinoma of the prostate the second most lethal cancer in men in the United States (1). New detection methods are critically needed to achieve earlier diagnosis and better staging of the disease. SPION contrast agents have been used to enhance the contrast of tumors in MRI, but novel contrast agents with increased relaxivities could be useful in detecting smaller tumors earlier and with lower doses of the contrast agents. Additionally, the specific targeting of contrast agents and therapeutics to cells of interest is now widely accepted as a cornerstone to the development of individualized diagnosis and treatment. Here, we report the synthesis of SIPP core particles from simple salts and their subsequent encapsulation in a mixture of phospholipids and conjugation to a monoclonal antibody against PSMA to produce stable, water soluble, multifunctional contrast agents with targeting, fluorescent, and MRI capabilities for the specific detection of prostate cancer cells. To our knowledge this is the first report of the synthesis

www.manaraa.com

of multifunctional SIPP micelles and the first report of using SIPPs for the specific detection of prostate cancer.

The SIPP cores have a large effective anisotropy energy of 2.5 x 10^5 J/m^3 and magnetic moment of 120 A m^2/kg Fe. We expected that the particles with higher mass magnetizations would be better contrast agents for MRI. We found this to be true when comparing the different composition particles. Compared to the SPIONs, the SIPPs have a higher magnetization accompanied by an ~ 13-fold higher transverse relaxivity at 4.7 Tesla. TGA suggests that the particles are ~ 45% SIPP core and ~ 55% phospholipid. The TEM images show that the SIPP cores and DSPE-SIPPs have diameters of 8.5 nm ± 1.6 and 42.9 nm ± 8.2 nm, respectively. The DSPE-SIPPs are spherical and contain 7.2 ± 6.8 SIPP cores per DSPE-SIPP. These structural characterizations suggest that the DSPE-SIPPs are micellar contrast agents. Using fluorescence confocal microscopy, we determined that the J591-DSPE-SIPPs specifically bound to C4-2 human prostate cancer cells that over-express PSMA and did not bind to PC-3 cells that do not express PSMA. Additionally, IgG-DSPE-SIPPs did not accumulate in either cell line. This shows the specific detection of PSMA-expressing human prostate cancer cells using the fluorescent capabilities of the SIPP immunomicelles. Finally, we show that the DSPE-SIPPs were 13-fold better than commercially available SPIONs and 1.6- to 3-fold better than Feridex® and Resovist® at producing negative contrast in MRI, at 4.7 Tesla. Taken together, our data suggest that the multifunctional SIPP immunomicelles are superior contrast agents for T_2-weighted MRI, specifically target PSMA-expressing human

www.manaraa.com

prostate cancer cells, can be used to specifically detect human prostate cancer cells *in vitro* using fluorescence microscopy, and should be beneficial as MRI contrast agents. Future studies will include using MRI to specifically detect human prostate cancer cells *in vivo* using the SIPP immunomicelles. It is important to note that the DSPE-SIPPs could be conjugated to any antibody or peptide for selective targeting and non-invasive detection of other types of tumors, using MRI. An additional benefit to this multimodal platform is that the *in vivo* biodistribution of the nanoparticles could be measured by examining the tissues and tumors *in vivo* and/or *ex vivo*, using small animal fluorescent imagers and fluorescence microscopy. Overall, our data suggest that J591-DSPE-SIPPs specifically target human prostate cancer cells *in vitro*, can be easily detected using fluorescence microscopy, and are superior contrast agents in T_2-weighted MRI.

Acknowledgments

The authors acknowledge the support from the National Institutes of Health 5RO1CA123194. This work was performed, in part, at the Center for Integrated Nanotechnologies, a U.S. Department of Energy, Office of Basic Energy Sciences user facility at Los Alamos National Laboratory (Contract DE-AC52-06NA25396) and Sandia National Laboratories (Contract DE-AC04-94AL85000). TEM images were generated at the University of New Mexico Electron Microscopy Facility. Confocal images were generated in the University of New Mexico & Cancer Center Fluorescence Microscopy Shared Resource, funded as

www.manaraa.com

detailed on: http://hsc.unm.edu/crtc/microscopy/Facility.html. Some experiments used the facilities provided by the Keck-UNM Genomics Resource, a facility supported by a grant from the WM Keck Foundation as well as the State of New Mexico and the UNM Cancer Research and Treatment Center. We would like to thank Dr. Stephen Jett for TEM expertise and Dr. Rebecca Lee and Genevieve Phillips for their expert guidance with confocal microscopy.

www.manaraa.com

References

1. Jemal A, Siegel R, Xu J, Ward E. Cancer statistics, 2010. CA Cancer J Clin 2010;60(5):277-300.

2. Andrew W, Wender RC, Etzioni RB, Thompson IM, D'Amico AV, Volk RJ, Brooks DD, Dash C, Guessous I, Andrews K, DeSantis C, Smith RA. American Cancer Society Guideline for the Early Detection of Prostate Cancer. CA Cancer J Clin 2010;60(2):70-98.

3. Rabbani F, Stroumbakis N, Kava BR, Cookson MS, Fair WR. Incidence and clinical significance of false-negative sextant prostate biopsies. J Urol 1998;159(4):1247-1250.

4. Afnan J, Tempany CM. Update on prostate imaging. Urol Clin North Am 2010;37(1):23-25, Table of Contents.

5. Peng XH, Qian X, Mao H, Wang AY, Chen ZG, Nie S, Shin DM. Targeted magnetic iron oxide nanoparticles for tumor imaging and therapy. Int J Nanomedicine 2008;3(3):311-321.

6. Rajasekaran AK, Anilkumar G, Christiansen JJ. Is prostate-specific membrane antigen a multifunctional protein? Am J Physiol Cell Physiol 2005;288(5):C975-981.

7. Ghosh A, Heston WD. Tumor target prostate specific membrane antigen (PSMA) and its regulation in prostate cancer. J Cell Biochem 2004;91(3):528-539.

8. Chang SS, Gaudin PB, Reuter VE, O'Keefe DS, Bacich DJ, Heston WD. Prostate-Specific Membrane Antigen: Much More Than a Prostate Cancer Marker. Mol Urol 1999;3(3):313-320.

9. Zhang C, Liu T, Gao J, Su Y, Shi C. Recent development and application of magnetic nanoparticles for cell labeling and imaging. Mini Rev Med Chem 2010;10(3):193-202.

10. Lee JH, Huh YM, Jun YW, Seo JW, Jang JT, Song HT, Kim S, Cho EJ, Yoon HG, Suh JS, Cheon J. Artificially engineered magnetic nanoparticles for ultra-sensitive molecular imaging. Nat Med 2007;13(1):95-99.

11. Han L, Wiedwald U, Kuerbanjiang B, Ziemann P. Fe oxidation versus Pt segregation in FePt nanoparticles and thin films. Nanotechnology 2009;20(28):285706.

12. Kim JR, C.; Liu, P.; Sun, S. Dispersible Ferromagnetic FePt Nanoparticles. Adv Mater 2009;21:906-909.

www.manaraa.com

13. Antoniak C, Lindner J, Spasova M, Sudfeld D, Acet M, Farle M, Fauth K, Wiedwald U, Boyen HG, Ziemann P, Wilhelm F, Rogalev A, Sun S. Enhanced orbital magnetism in Fe(50)Pt(50) nanoparticles. Phys Rev Lett 2006;97(11):117201-117201 to 117201-117204.

14. Sun S. Recent Advances in Chemical Synthesis, Self-Assembly, and Applications of FePt Nanoparticles. Adv Mater 2006;18:403.

15. Sun S, Murray CB, Weller D, Folks L, Moser A. Monodisperse FePt nanoparticles and ferromagnetic FePt nanocrystal superlattices. Science 2000;287(5460):1989-1992.

16. Basit L, Nepijko SA, Shukoor I, Ksenofontov V, Klimenkov M, Fecher GH, Schonhense G, Tremel W, Felser C. Structure and magnetic properties of iron-platinum particles with y-ferric-oxide shell. Appl Phys A 2009;94:619-625.

17. Varanda LC, Jafelicci M, Jr. Self-assembled FePt nanocrystals with large coercivity: reduction of the fcc-to-L1(0) ordering temperature. J Am Chem Soc 2006;128(34):11062-11066.

18. Boyen HG, Fauth K, Branko S, Ziemann P, Kastle G, Weigl F, Banhart F, Hessler M, Schutz G, Gajbhiye NS, Ellrich J, Hahn H, Buttner M, Garnier MG, Oelhafen P. Electronic and Magnetic Properties of Ligand-Free FePt Nanoparticles. Adv Mater 2005;17(5):574-578.

19. Chen S, Wang L, Duce SL, Brown S, Lee S, Melzer A, Cuschieri A, Andre P. Engineered biocompatible nanoparticles for in vivo imaging applications. J Am Chem Soc 2010;132(42):15022-15029.

20. Morales MP, Bedard MF, Roca AG, Presa P, Hernando A, Zhang F, Zanella M, Zahoor AA, Sukhorukov GB, del Mercato LL, Parak WJ. Relaxation times of colloidal iron platinum in polymer matrixes. J Mater Chem 2009;19:6381-6386.

21. Maenosono S, Suzukia T, Saita S. Superparamagnetic FePt nanoparticles as excellent MRI contrast agents. J Magn Magn Mater 2008;320:L79-L83.

22. Xu C, Yuan Z, Kohler N, Kim J, Chung MA, Sun S. FePt nanoparticles as an Fe reservoir for controlled Fe release and tumor inhibition. J Am Chem Soc 2009;131(42):15346-15351.

23. Zhao F, Rutherford M, Grisham SY, Peng X. Formation of monodisperse FePt alloy nanocrystals using air-stable precursors: fatty acids as alloying

www.manaraa.com

mediator and reductant for Fe3+ precursors. J Am Chem Soc 2009;131(14):5350-5358.

24. Barmak K, Kim J, Lewis LH, Coffey KR, Toney MF, Kellock AJ, Thiele JU. Stoichiometry - Anisotropy Connections in Epitaxial L10 FePt(001) Films. Magnetism and Magnetic Materials Conference. Anaheim, CA, USA; 2004.

25. Zeng H, Li J, Liu JP, Wang ZL, Sun S. Exchange-coupled nanocomposite magnets by nanoparticle self-assembly. Nature 2002;420(6914):395-398.

26. Inomata K, Sawa T, Hashimoto S. Effect of large boron additions to magnetically hard Fe-Pt alloys. J Appl Phys 1988;64(5):2537-2540.

27. Bhalerao GM, Sinha AK, Srivastava AK. Synthesis of monodispersed gamma-Fe2O3 nanoparticles using ferrocene as a novel precursor. J Nanosci Nanotechnol 2009;9(9):5502-5506.

28. Serda RE, Godin B, Blanco E, Chiappini C, Ferrari M. Multi-stage delivery nano-particle systems for therapeutic applications. Biochim Biophys Acta 2010.

29. Pasut G, Veronese FM. PEGylation for improving the effectiveness of therapeutic biomolecules. Drugs Today (Barc) 2009;45(9):687-695.

30. Rasband WS. ImageJ. US National Institutes of Health, Betesda, Maryland, USA, http//rsbinfonihgov/ij/ 1997-2009.

31. Johnsson M, Edwards K. Liposomes, disks, and spherical micelles: aggregate structure in mixtures of gel phase phosphatidylcholines and poly(ethylene glycol)-phospholipids. Biophys J 2003;85(6):3839-3847.

32. Serda RE, Adolphi NL, Bisoffi M, Sillerud LO. Targeting and cellular trafficking of magnetic nanoparticles for prostate cancer imaging. Mol Imaging 2007;6(4):277-288.

33. Schaller V, Wahnstrom G, Sanz-Velasco A, Enoksson P, Johansson C. Determination of Nanocrystal Size Distribution in Magnetic Multicore Particles Including Dipole-Dipole Interactions and Magnetic Anisotropy: a Monte Carlo Study. In: Hafeli U, Schutt W, Zborowski M, editors; 2010. American Institute of Physics.

34. Miltenyi S, Muller W, Weichel W, Radbruch A. High gradient magnetic cell separation with MACS. Cytometry 1990;11(2):231-238.

www.manaraa.com

35. Salgueirino-Maceira V, Liz-Marzan LM, Farle M. Water-based ferrofluids from FexPt1-x nanoparticles synthesized in organic media. Langmuir 2004;20(16):6946-6950.

36. Demortiere A, Panissod P, Pichon BP, Pourroy G, Guillon D, Donnio B, Begin-Colin S. Size-dependent properties of magnetic iron oxide nanocrystals. Nanoscale 2010.

37. Sohn BH, Cohen RE, Papaefthymiou GC. Magnetic properties of iron oxide nanoclusters within microdomains of block copolymers. J Magn Magn Mater 1998;182(1-2):216-224.

38. Wolf P, Freudenberg N, Buhler P, Alt K, Schultze-Seemann W, Wetterauer U, Elsasser-Beile U. Three conformational antibodies specific for different PSMA epitopes are promising diagnostic and therapeutic tools for prostate cancer. Prostate 2010;70(5):562-569.

39. Sobel RE, Sadar MD. Cell lines used in prostate cancer research: a compendium of old and new lines--part 1. J Urol 2005;173(2):342-359.

40. Kuroda K, Liu H, Kim S, Guo M, Navarro V, Bander NH. Saporin toxin-conjugated monoclonal antibody targeting prostate-specific membrane antigen has potent anticancer activity. Prostate 2010;70(12):1286-1294.

41. Patel D, Kell A, Simard B, Xiang B, Lin HY, Tian G. The cell labeling efficacy, cytotoxicity and relaxivity of copper-activated MRI/PET imaging contrast agents. Biomaterials 2010.

42. Yang HM, Park CW, Woo MA, Kim MI, Jo YM, Park HG, Kim JD. HER2/neu Antibody Conjugated Poly(amino acid)-Coated Iron Oxide Nanoparticles for Breast Cancer MR Imaging. Biomacromolecules 2010.

43. Figuerola A, Fiore A, Di Corato R, Falqui A, Giannini C, Micotti E, Lascialfari A, Corti M, Cingolani R, Pellegrino T, Cozzoli PD, Manna L. One-pot synthesis and characterization of size-controlled bimagnetic FePt-iron oxide heterodimer nanocrystals. J Am Chem Soc 2008;130(4):1477-1487.

44. Hinds KA, Hill JM, Shapiro EM, Laukkanen MO, Silva AC, Combs CA, Varney TR, Balaban RS, Koretsky AP, Dunbar CE. Highly efficient endosomal labeling of progenitor and stem cells with large magnetic particles allows magnetic resonance imaging of single cells. Blood 2003;102(3):867-872.

45. Wang YX, Hussain SM, Krestin GP. Superparamagnetic iron oxide contrast agents: physicochemical characteristics and applications in MR imaging. Eur Radiol 2001;11(11):2319-2331.

www.manaraa.com

Chapter 5

Paclitaxel-Loaded, PSMA-Targeted Iron Platinum Stealth Immunomicelles are Potent Magnetic Resonance Imaging Agents that Prevent Prostate Cancer Growth.

Robert M. Taylor[1,2] and Laurel O. Sillerud[1,3]

[1]Department of Biochemistry and Molecular Biology,
[2]Cancer Nanoscience and Microsystems Training Center,
[3]Cancer Research and Treatment Center,
University of New Mexico School of Medicine,
915 Camino de Salud NE, Albuquerque, NM 87131

Manuscript submitted to Cancer Research, April 2012

www.manaraa.com

Abstract

Prominent and unresolved problems with the clinical management of prostate cancer include the lack of both specific detection methods and efficient therapeutic interventions. We report the encapsulation of superparamagnetic iron platinum nanoparticles (SIPPs) and paclitaxel (PTX) in a mixture of polyethyleneglycolated (PEGylated), fluorescent, and biotin-functionalized phospholipids to create multifunctional SIPP-PTX micelles (SPMs) that were conjugated to an antibody (J591) against prostate specific membrane antigen (PSMA) for the specific targeting, magnetic resonance imaging (MRI), and therapy of human prostate cancer xenografts in mice. These SPMs were 45.4 ± 24.9 nm in diameter and composed of 160.7 ± 22.9 μg/mL iron, 247.0 ± 33.4 μg/mL platinum, and 702.6 ± 206.0 μg/mL PTX. Drug release measurements showed that, at 37 °C, half of the PTX was released in 30.2 hours in serum and two times faster in saline. Binding assays suggested that PSMA-targeted SPMs specifically bound to C4-2 human prostate cancer cells *in vitro* and released the PTX into the cells. *In vitro*, PTX was 2.2 and 1.6 times more cytotoxic than SPMs to C4-2 cells at 24 and 48 hours incubation, respectively. After 72 hours of incubation, PTX and SPMs were equally cytotoxic as expected from the release kinetics. SPMs had MRI transverse relaxivities of 389 ± 15.5 Hz/mM iron and SIPP-micelles with and without drug caused MRI contrast enhancement *in vivo*. Only PSMA-targeted SPMs and PTX significantly prevented growth of C4-2 human prostate cancer xenografts in nude mice. Furthermore, mice injected with

www.manaraa.com

PSMA-targeted SPMs showed significantly more PTX and platinum in tumors, compared to non-targeted SPM and PTX injected mice.

Introduction

The continued prevalence, and resistance to treatment, of prostate cancer in the United States suggests that detection and therapeutic methods must be improved in order to combat this disease, especially in the deadly, advanced hormone refractory stage. As of 2011, prostate cancer remained the most commonly-detected male cancer in the United States and the second most common reason for cancer death in men (1). With over 200,000 newly diagnosed cases, and in excess of 30,000 mortalities, prostate cancer continued to be a major burden on the health and financial security of countless men and families (1-3). After a rapid increase in diagnosed cases in the 1990's, mostly due to prostate specific antigen (PSA) testing, the number of newly-diagnosed cases has plateaued over the past several years. Numerous new therapies have entered clinical trials in recent years, without a meaningful decline in the number of mortalities (1,3-7); nevertheless, innovative therapies are clearly required.

Over the past decade significant progress has been made with respect to the development of novel nanoparticles designed either for the detection or therapy of cancers (8-14). The most common types of nanoparticles used for the detection of cancer were fluorescent, radioactive, or superparamagnetic core nanoparticles that were rendered biocompatible by encapsulation with polymers or phospholipids (8,12,15,16). Similarly, chemotherapeutic drugs were added to

www.manaraa.com

the encapsulants with the expectation that more efficacious therapies, with reduced global toxicity, would result (17-19). These two types of nanoparticles were typically targeted to primary and/or metastatic tumors either passively by the enhanced permeation and retention (EPR) effect, which relied on the leaky vasculature often found in tumors, or through active targeting of specifically over-expressed, or highly-expressed, membrane antigens on the tumor cells or neovasculature. For this latter purpose, antibodies or peptides were often conjugated to the surface of the particles (20-22). The development of nanoparticles that combined these two functions, while highly desirable, had not received as much attention as was directed towards the synthesis of particles with separate functions.

Previously, superparamagnetic iron oxide nanoparticles (SPIONs) have been used as experimental MRI contrast agents to detect cancers (23-26). In fact, two SPION contrast agents, Resovist® and Feridex®, have been approved for use by the Food and Drug Administration (FDA) (26,27). Although SPIONs produce contrast enhancement in MRI, the signal enhancement was often weaker than that found in radioisotopic imaging modes such as positron emission tomography (PET) (28). Therefore, better MRI contrast agents were critically needed in order to increase signal enhancement for the non-invasive detection of cancer. We previously reported that SIPPs were superior MRI contrast agents compared to the more commonly used SPIONs (29,30). For this reason we chose to use SIPPs as our core magnetic particle for MRI. Additionally, we previously showed that these SIPP particles could be encapsulated into micelles

www.manaraa.com

using a mixture of PEGylated phospholipids and that these particles could be specifically targeted to prostate cancer cell lines, *in vitro*, using the J591 anti-PSMA antibody (30).

Here, we report the synthesis, characterization, and application of specifically-targeted, multifunctional, superparamagnetic iron platinum particles (SIPPs) (29) that were encapsulated in a mixture of functionalized phospholipids, and combined with the chemotherapeutic drug, paclitaxel (PTX). These SIPPs were subsequently conjugated to a humanized monoclonal antibody (J591) against prostate specific membrane antigen (PSMA) to produce targeted SIPP-PTX micelles (SPMs) for the combined magnetic resonance imaging (MRI) detection and therapy of prostate cancer. We measured the physical, magnetic, binding, and cytotoxic properties of the particles *in vitro*, and the MRI contrast enhancement, biodistribution, and efficacy *in vivo*, compared with PTX alone.

Materials and Methods

Materials

Iron nitrate nonahydrate ($Fe(NO_3)_3 \cdot 9H_2O$), Platinum (II) acetylacetonate ($Pt(Acac)_2$), and ODA were purchased from Fisher Scientific (Pittsburgh, PA). The temperature controller (model 210-J) was purchased from J-KEM Scientific, Inc. (St. Louis, MO). Heating mantles were purchased from Glas-Col, Llc, (Terre Haute, IN) and glassware was purchased from Quark Glass (Vineland, NJ). The phospholipids: 1,2-distearoyl-sn-glycero-3-phosphoethanolamine-N-[amino-

www.manaraa.com

(polyethyleneglycol)-2000] (DSPE-PEG), DSPE-PEG with biotin conjugated to the head group (biotin-DSPE-PEG), and 1,2-dimyristoyl-sn-glycero-3-phosphoethanolamine-N-[lissamine rhodamine B sulfonyl] (Liss-Rhod) were purchased from Avanti Polar Lipids (Alabaster, AL). RPMI cell culture media, fetal bovine serum, and Penicillin-Streptomycin Solution were purchased from Sigma (St. Louis, MO). The C4-2 human prostate cancer cell line was a generous gift from Dr. Marco Bisoffi (UNM). All other chemicals and supplies were purchased from common manufacturers.

Synthesis of SIPP cores

One mmol $Fe(NO_3)_3 \cdot 9H_2O$ and 1.0 mmol $Pt(Acac)_2$ were added to 12.5 mmol ODA in a 25 mL, 3-neck, round-bottom flask fitted with a reflux condenser. The reaction mixture was heated to 330 °C (at a rate of 200 °C/hr) with 10 °C recirculated cooling in the reflux condenser. Refluxing was continued for 45 minutes, at which point the reaction mixture was removed from the heat and allowed to cool to room temperature. The resulting black particles were collected in hexane and subjected to repeated washing by collecting the particles in conical tubes with an external magnet, removing the supernatant, and resuspending in hexane.

Encapsulation of SIPP cores and Paclitaxel

Phospholipid-encapsulated SIPP cores with and without Paclitaxel (SPMs and SMs respectively) were prepared using a thin film method. One-half mL of SIPP

www.manaraa.com

cores (1.4% solids) in hexane was added to a 20.0 mL glass scintillation vial. A chloroform mixture of (56:1:1 mole ratio) DSPE-PEG, biotin-DSPE-PEG, and Liss-Rhod was then added to the SIPP cores. In the SPM preparations, 0.4 mL of 8 mg/mL Paclitaxel in chloroform was also added to the reaction. The mixture was further diluted in 0.5 mL of methanol and vortexed thoroughly. The vial was allowed to evaporate under a gentle nitrogen stream in a chemical fume hood to produce a thin film. 5.0 mL of double-distilled water was heated to 90 °C and added to the thin film. Hydration of the thin film was immediate upon brief vortexing. The hydrated particles were then extruded at 67 °C through an 80 nm Nucleopore track-etch membrane filter using a mini-extruder (Avanti Polar Lipids, Alabaster, AL) to produce ~ 45 nm micelles. The SPMs and SMs were then purified from SIPP-free micelles, excess phospholipids, and drug by collecting the magnetic particles using an LS magnetic column placed in a VarioMACS™ magnetic separator (Miltenyi Biotec, Carlsbad, CA). After the non-magnetic material had passed through the column, 8.0 mL of double-distilled water was added to the top of the column to wash the particles. The column was removed from the magnet and placed in a tube rack with a 2.0 mL glass vial placed underneath the column. One mL of sterile saline was used to elute the purified SPMs and SMs from the column. For SPMs and SMs for injections into mice, the eluted particles were applied to smaller (0.5 mL) μColumns (Miltenyi Biotec, Carlsbad, CA) and eluted with 200 - 300 μL of sterile saline.

www.manaraa.com

Physical Characterization of SPMs

Transmission electron microscopy (TEM) was used to determine the size and polydispersity of the particle populations. For SIPP cores, a drop of the hexane suspension was applied to a carbon-coated grid and allowed to dry. For SPMs and SMs, a drop of the aqueous suspension was applied to a carbon-coated grid, allowed to dry for 10 minutes, and the excess was absorbed using a kimwipe. Adding a drop of 2% Uranyl Acetate solution followed by a 2-minute drying period negatively stained the grid. The excess solution was removed and the grid was allowed to dry for at least 5 minutes. The samples were imaged on a Hitachi 7500 transmission electron microscope with an acceleration voltage of 80 kV. Particle diameters were calculated using ImageJ Software (31). At least 100 particles were counted and the mean Feret's diameters and standard deviations were calculated. Diameters of the SPMs were additionally measured using Dynamic Light Scattering (DLS) with a Microtrac Nanotrac^{TM} Ultra DLS (Microtrac, Largo, FL). Inductively-coupled-plasma, optical-emission-spectroscopy (ICP-OES) was used to measure the metal content and iron to platinum ratio of each synthesis. Prior to analysis, aliquots of the particles were digested at 180 °C with nitric and hydrochloric acids in a PDS-6 Pressure Digestion System (Loftfields Analytical Solutions, Neu Eichenberg, Germany). After cooling, the samples were made up to a known volume, mixed and centrifuged. Samples were then analyzed using a PerkinElmer Optima 5300DV ICP-OES. The recommended wavelengths for each of the analytes were used and analysis was performed in the axial mode to improve detection limits. A

www.manaraa.com

blank and set of calibration standards were used to establish a three-point calibration curve. Calibration and instrument verification samples were analyzed before and after analyzing the samples, as well as periodically throughout the measurements. Analyte peaks were examined and peak identification and background points were adjusted for optimum recoveries.

Magnetic Resonance Relaxometry

Increasing concentrations of SPMs (0 to 400 μM iron) were added to 1% agarose in 2.0 mL self-standing micro-centrifuge tubes (Corning, Corning, NY). Samples were imaged on a 4.7 Tesla Bruker Biospin (Billerica, MA) MRI system with Paravision 4.0 software. Samples were imaged with a 512 x 256 matrix, a variable TE, and TR = 10 sec. T_1 measurements were acquired by inversion-recovery with 15 interpulse delays. Spin- and gradient-echo sequences were used to measure T_2, and T_2*, respectively. The MRI samples were then digested as above and the iron concentration was determined with ICP. The relaxation rates, $R_n = \frac{1}{T_n}$, were calculated and plotted *versus* the ICP-determined iron concentration of each sample. The relaxivity (r_n) of each sample is given as the slope of the linear regression line in units of s^{-1} mM^{-1} (Hz/mM) of iron.

Drug Loading Capacity and Drug Release Rates

The amount of Paclitaxel loaded into the particles was quantitated with a competitive elisa (Cardax Pharmaceuticals, Aiea, HI), according to the

www.manaraa.com

manufacturers instructions. Briefly, a 100 µL aliquot of the SPMs was added to 200 µL of a 1:1 (vol/vol) acetonitrile:methanol mixture. The mixture was incubated with occasional vortexing. After 30 minutes, the solution was centrifuged at 14,000 rpm for 5 minutes in a tabletop microcentrifuge. Ten-fold dilutions of the supernatant were prepared in BPT-M buffer (Phosphate buffered saline (PBS) with 0.25% (w/v) BSA, 0.05% (v/v) Tween-20, 0.02% (w/v) sodium azide) and 50 µL of each dilution was then subjected to the Elisa in triplicates to determine the amount of Paclitaxel loaded into the particles. For the drug release rate experiments, a 100 µL aliquot of the freshly prepared particles (~ 1.0 mL) was collected as the zero-hour time point. At various subsequent timed points, the particles were collected on an LS magnetic column placed in a VarioMACS™ magnetic separator (Miltenyi Biotec, Carlsbad, CA). The non-magnetic material flow through (released Paclitaxel) was collected for Elisa quantitation and the collected particles were then eluted in the original volume of serum or saline, an aliquot of particles was taken for the Elisa, and the collected particles were then incubated at 4 °C, 20 °C, or 37 °C until the next timed point. This routine was repeated until the completion of the experiment; at which time another 100 µL aliquot of the SPMs was collected. Finally, the zero-hour and final particle aliquots were added to an equal volume of 1:1 (vol/vol) acetonitrile:methanol mixture an allowed to incubate for 30 minutes prior to the PTX Elisa. The amount of Paclitaxel in each well was measured based on a baccatin III-protein standard curve.

www.manaraa.com

Antibody Conjugation, cell culture, and confocal binding assay

Humanized monoclonal antibody raised against the extracellular portion of PSMA (J591) (from Dr. Neal Bander, Cornell College of Medicine) and polyclonal goat anti-rabbit IgG (Sigma, St. Louis, MO) were conjugated to streptavidin in an overnight reaction using a Lightning-Link™ Streptavidin Conjugation Kit (Innova Biosciences, Cambridge, UK) according to the manufacturers instructions. Concentrations of streptavidin, antibodies, and streptavidin-antibody conjugates were quantitated using a NanoDrop™ 2000 Spectrophotometer (Wilmington, DE). Streptavidin-conjugated antibodies (~ 1.0 μg) were then incubated with SPMs or SMs (~ 150 μg iron) at 4 °C to conjugate the antibodies to the SIPP micelles through the biotin groups of the biotin-DSPE-PEG. A Micro BCA™ Protein Assay (Thermo Scientific, Rockford, IL) was used to measure the antibody concentrations and the amount of antibody conjugated to the micelle surface using a BioSpec-mini Spectrophotometer (Shimadzu, Columbia, MD) at a wavelength of 562 nm. Twenty thousand C4-2 human prostate cancer cells in RPMI 1640 medium containing 10% fetal bovine serum and 100 U/mL Penicillin-Streptomycin solution were seeded onto polylysine-coated cover slips in 6-well polystyrene plates (Corning, Corning, NY) and incubated at 37 °C, 5% CO_2 for 24 hours. The medium was then exchanged with medium containing J591-SPMs (~ 4.0 μg iron), IgG-SPMs (~ 4.0 μg iron), or PBS (40 μL). The cells were incubated with the particles for 10 minutes at 4 °C, the media were aspirated off, and 5.0 mL PBS was added to wash unbound particles away from the cells. Washing was repeated 3 times. Cover slips were mounted on slides containing a drop of

www.manaraa.com

ProLong® Gold Antifade Reagent with DAPI (Invitrogen, Eugene, OR). Confocal Images were acquired using an Olympus DSU spinning disk confocal microscope in the University of New Mexico & Cancer Center Fluorescence Microscopy Shared Resource: http://hsc.unm.edu/crtc/microscopy/Facility.html.

Cytotoxicity

Five thousand C4-2 cells in 100 µL of RPMI 1640 medium were cultured in 96 well plates. The following day, media were exchanged with 100 µL of media containing the treatment or controls in increasing concentrations of PTX and platinum (Pt), determined by measuring the PTX and Pt content of the preparations using a PTX Elisa and ICP, respectively (*vide supra*). A WST-1 cytotoxicity kit (a modified MTT Assay from Roche Applied Science) was used to quantitate the number of metabolically active cells at 24, 48, or 72 hours. The absorbencies of the samples were normalized to the no-treatment control. Dose response curves were generated as a function of increasing concentration of treatment/controls. The dose to inhibit the metabolic activity of 50% of the cells was determined by non-linear regression.

Animal Experiments

The University of New Mexico International Animal Care and Use Committee approved all experiments involving animals. 4-6 week old athymic nude mice had 3 x 10^6 C4-2 human prostate cancer cells in 50% (vol/vol) Matrigel® (BD Bioscience, Bedsford, MA) subcutaneously injected into the right flank. The mice

www.manaraa.com

were monitored and the length, width, and height of the tumors were measured using a digital caliper. The volumes of the xenografts were determined using the equation $V = \left(\frac{4}{3}\right)abc$. Where V is the tumor volume and a, b, and c are half the length, width, and height, respectively. Once the xenografts had reached volumes of 50-100 mm^3, they were subjected to MRI and injections of treatments or controls.

In vivo MRI and injections

Once the xenografts had reached the appropriate volume, mice were anesthetized using a nose cone that delivered an isoflurane and oxygen mixture and imaged on a 4.7 Tesla Bruker Biospin (Billerica, MA) MRI system with Paravision 4.0 software. Mice were imaged with a 256 x 256 pixel matrix with 156 mm pixels and a 40 mm field of view. T_1 measurements were acquired with a TE = 14 msec and a Rapid Acquisition with Relaxation Enhancement with Variable Repetition Time (RAREVTR) sequence. T_2 measurements were acquired with a TE = 12 msec and a Multi Slice Multi Echo (MSME) sequence. After the pre-injection imaging, the mice were injected retro-orbitally with 150 µL of treatments or controls. SIPP-containing injections contained ~200 µg of iron and 702.6 ± 206 µg of PTX, depending on the preparation. The PTX-only mice were injected with 400 µg of PTX in a total volume of 150 µL of castor oil and phosphate buffered saline (PBS). Additionally some mice were not injected with anything as a “no-injection” control group. After the pre-injection imaging and subsequent injections, the mice were once again imaged at various timed points

www.manaraa.com

ranging from 15 minutes to 24 hours post-injection. The T_1 and T_2 images were analyzed using ImageJ (30) software. Regions of interest in the tumor and muscle were selected and the mean pixel intensity and standard deviations were recorded at each timed point. Contrast was then calculated as $C = (\frac{I_t - I_m}{I_m})$, where C is the contrast and I_t and I_m are the pixel intensity in the tumor or muscle, respectively. The contrast was normalized to the pre-injection images to produce the contrast (%), calculated as $C\% = (\frac{C_t}{C_o}) \times 100$, where C_t and C_o are the contrast of the tumor at the timed point and initial contrast of the tumor in the pre-injection image, respectively. Contrast (%) was then plotted verses time post-injection.

Biodistribution and Therapeutic Efficacy

The mice were monitored for 20 days starting on the day of injection with treatments or controls. The tumor volumes were measured weekly and the mice were monitored for adverse reactions such as weight loss, infection, paralysis, and lethargy. On day 20 post-injection, the mice were euthanized using carbon dioxide-asphyxiation and the tumor and organs were collected and weighed. Portions of the tumor and organs were then sectioned and again weighed for ICP and PTX analysis of Pt and PTX content, respectively. The amount of Pt and PTX was then calculated as percent of the Pt or PTX in the original injection. The average and standard deviation of Pt and PTX in each group of mice was then calculated and plotted for each tissue or xenograft to determine the

www.manaraa.com

biodistribution and amount of targeting. The tumor volumes and mass of each tumor were compared between each of the groups of treatment and control mice. Efficacy was measured by decreases in tumor volume in the treatment versus control groups.

Results

Size and Composition of the SIPP Paclitaxel Micelles (SPMs). Figure 5.1 shows a TEM image of the SPMs. The synthesized SPMs had diameters of 45 ± 25 nm as determined using DLS. This large standard deviation was representative of the polydispersity that can be seen in the TEM images (Fig. 5.1). The SPMs appeared to fall into two morphological groups. Once group had multiple, ~9 nm diameter SIPPs (in agreement with our earlier data (23, 30)) encapsulated in the core and were larger in overall diameter (~ 50 nm), whereas the other group of particles had smaller diameters of 29 ± 2 nm, and appeared to contain only a single, crystalline 17 ± 2 nm SIPP core encapsulated in the center. It was important to note that all of these particles were first purified and separated with a magnetic column; this fact implies that all of the particles in the TEM image possessed a magnetic SIPP core. It is possible that the smaller micelles resulted from a reaction between the FePt alloy and PTX, which generated a crystalline complex between the drug and the alloy.

www.manaraa.com

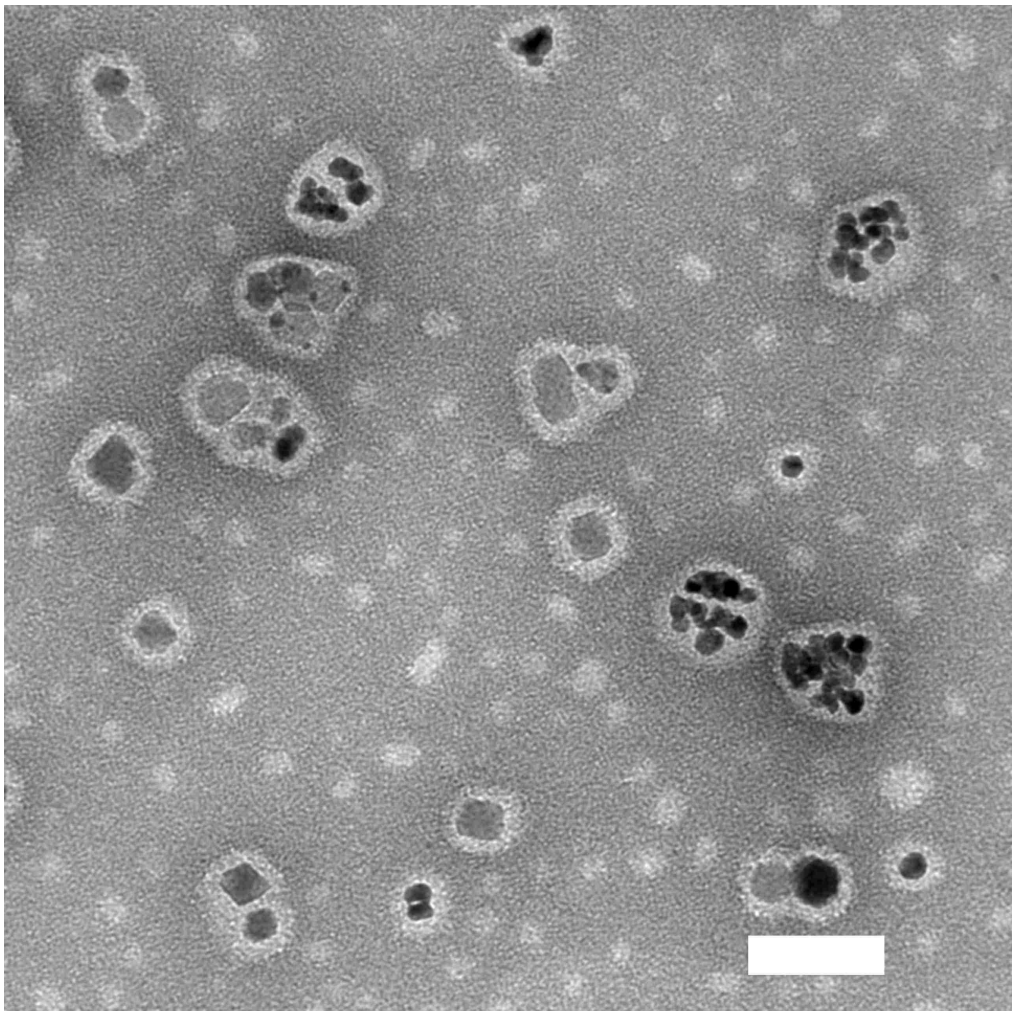

Figure 5.1 Transmission electron microscopy image of SPMs. A drop of SPMs was applied to a carbon-coated grid and allowed to dry. Adding a drop of 2% Uranyl Acetate solution followed by a 2-minute drying period negatively stained the grid. The excess stain was removed and the grid was allowed to dry for at least 5 minutes. The samples were imaged on a Hitachi 7500 transmission electron microscope with an acceleration voltage of 80 kV. The scale bar is 50 nm.

www.manaraa.com

The metal content of the SPMs was determined using ICP. We compared 4 separate preparations of the SPMs and found that they contained 161 ± 23 mg/mL of iron, 247 ± 33 mg/mL of platinum, and an iron to platinum stoichiometry of 2.3 ± 0.4, suggesting that our method for making SPMs provided good reproducibility.

Magnetic Relaxivities of the Micelles. We next compared the relaxivities of micelles with and without drug using magnetic resonance relaxometry. As expected from our previous characterizations of the SIPP cores (29,30), SIPP micelles without PTX (SMs) and SPMs had high transverse relaxivities of r_2 = 300 ± 12 and 389 ± 16 Hz/mM iron, respectively, making them superior contrast agents for T_2-weighted MRI compared to SPIONs that generally have transverse relaxivities between 30 and 180 Hz/mM iron (32-35).

PTX Loading of the Micelles. The amount of PTX encapsulated in the SPM preparations (drug loading capacity) was determined using a PTX competitive Elisa. The average drug loading capacity for seven preparations of particles was 703 ± 206 mg/mL PTX. The high standard deviation suggests that the amount of PTX incorporated into the micelles was subject to some unknown variation, perhaps due to phase fractionation, and that other methods of incorporating the drug into the particles, such as anchoring the drug to the micelles by conjugating a lipid chain to the drug, may be useful in the future.

www.manaraa.com

PTX Release from the Micelles. We next aimed to measure how fast the drug was released from the micelles (drug release rate) in different solutions and at different temperatures. Figure 5.2 shows the drug release rates for the particles in serum and saline at 4 °C and 37 °C.

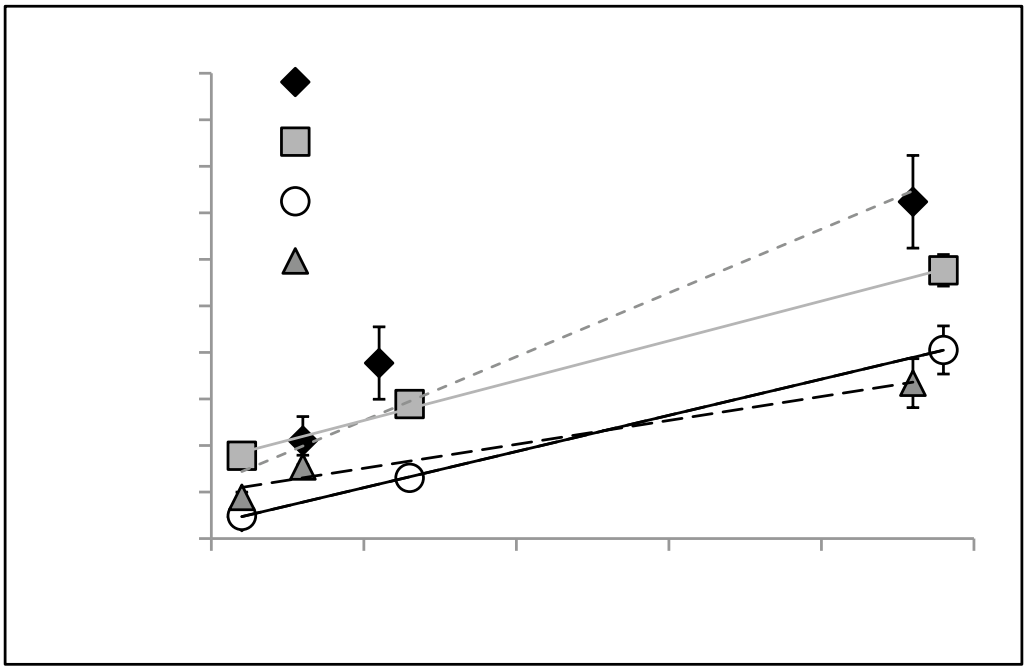

Figure 5.2 Temperature dependence of drug release rates for SPMs in serum and saline. A 100 µL aliquot of the freshly prepared particles was collected as the zero-hour time point. At various subsequent timed points, the particles were magnetically retained on a column and the amount of PTX in the non-magnetic flow-through and in the magnetic particles was measured using an Elisa. The amount of drug release is shown as the percent of drug released compared to the initial amount of drug loaded into the particles, as measured with an Elisa immediately after encapsulation. SPMs were incubated in saline at 20 °C (diamonds), saline at 37 °C (squares), serum at 37 °C (circles), or serum at 4 °C (triangles).

www.manaraa.com

The time at which half of the PTX had been released from the particles ($R_{0.5}$) under the different conditions was 19.4 and 14.0 hours for SPMs in saline at 20 °C and 37 °C, respectively. In contrast, the SPMs in serum at 4 °C and 37 °C had $R_{0.5}$ times of 38.9 and 30.2 hours, respectively. It was clear that the drug was released half as fast in serum ($R_{0.5}$ ~ 30 hours), compared to saline ($R_{0.5}$ ~ 14 hours) at 37 °C. It has previously been suggested that drugs were released at different rates from nanoparticles in the presence of different serum proteins (36-38) and, therefore, it is possible that serum proteins may be binding to our SPMs to some extent, causing the drug to be released more slowly due to an increase in the hydrodynamic diameter of the micelles when protein-bound. An interesting future study would be to determine what proteins and to what extent these proteins bind to our PEGylated micelles.

Specific Binding of Antibody-Conjugated Micelles to Prostate Tumor Cells. We conjugated a fully-humanized monoclonal antibody (J591), raised against the extracellular portion of PSMA, to our SPMs and measured the specific binding of the J591-SPMs to C4-2 human prostate cancer cells that express over one million PSMA receptors on the cell surface (39). Figure 5.3 shows that, compared to C4-2 cells incubated with non-targeted IgG-SPM control micelles, PSMA-targeted J591-SPMs specifically bound to C4-2 cells. Also of importance is that the green, fluorescent PTX can also be seen inside of the C4-2 cells that were specifically targeted and not in the cells that were incubated with IgG-SPMs,

www.manaraa.com

suggesting not only specific delivery of the contrast agent to the prostate cancer cells, but also the specific intracellular delivery of the chemotherapeutic drug.

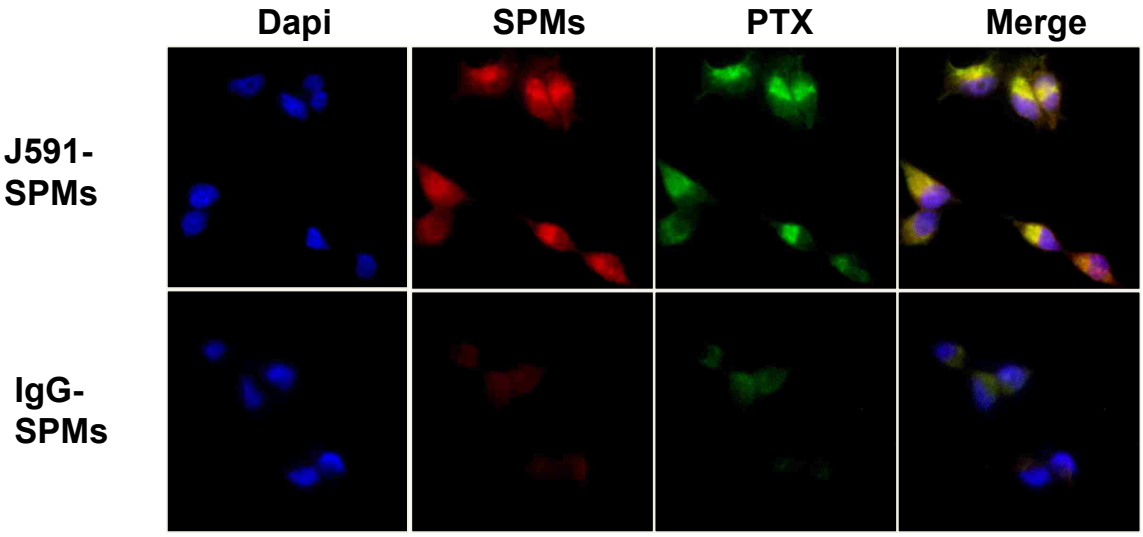

Figure 5.3 Specific binding of J591-SPMs to C4-2 prostate cancer cells. Confocal images of PSMA-targeted, rhodamine-red-containing SPMs containing fluorescent PTX (green) (Top Row) and control IgG-SPMs (Bottom Row) incubated with C4-2 human prostate cancer cells and stained with DAPI. The last column on the right shows the summed images, which displays all three colors for the J591-SPMs, and only shows DAPI staining for the IgG-SPMs.

www.manaraa.com

Comparison of the Cytotoxicity of the SPMs versus PTX Alone. Since the above results showed that the SPMs specifically bound to, and were taken up by prostate tumor cells, it was of considerable interest to determine if this intracellular delivery of the PTX was cytotoxic to the C4-2 cells and to compare the SPM's cytotoxicity with that of the SIPP micelles themselves. Figure 5.4 shows the cytotoxicity measurements for our SIPP micelles with and without drug over the course of 72 hours. The intracellular delivery of PTX by the micelles was equally cytotoxic to the cells compared to PTX alone after 72 hours of incubation. However, the PTX alone was somewhat more cytotoxic at 24 and 48 hours, compared to SPMs; the drug concentration to inhibit 50% of the cells metabolic activity (IC_{50}) at 24 hours was 22 and 50 μM for PTX alone and SPMs, respectively. At 48 hours the IC_{50}s for PTX and SPMs were 17 and 28 μM drug. In comparison, by 72 hours both PTX and SPMs had the same IC_{50} of 0.1 μM drug. Thus, *in vitro,* the PTX was 2.2 and 1.6 times more cytotoxic to the C4-2 prostate cancer cells at 24 and 48 hours, but were equally cytotoxic at 72 hours. This difference is most likely due to the fact that it takes ~ 30 hours for the drug encapsulated in the SPMs to escape (Figure 5.2), whereas the non-encapsulated PTX may begin binding to microtubules faster, in this *in vitro* setting. The SIPP micelles in the absence of drug were found to not be cytotoxic to the C4-2 cell line (Figure 5.4D) using platinum concentrations that were in the same range as those used in the SPM cytotoxicity experiments.

www.manaraa.com

SPMs and SIPPs as MRI Contrast Agents. We next produced C4-2 human prostate cancer xenografts in nude mice and performed MR imaging of the tumor both pre-injection and post-injection of treatments or controls. Figure 5.5 shows the T_1- and T_2-contrast enhancements measured in the tumors as a function of time, with representative images of an SPM injected tumor. The J591-SPMs and

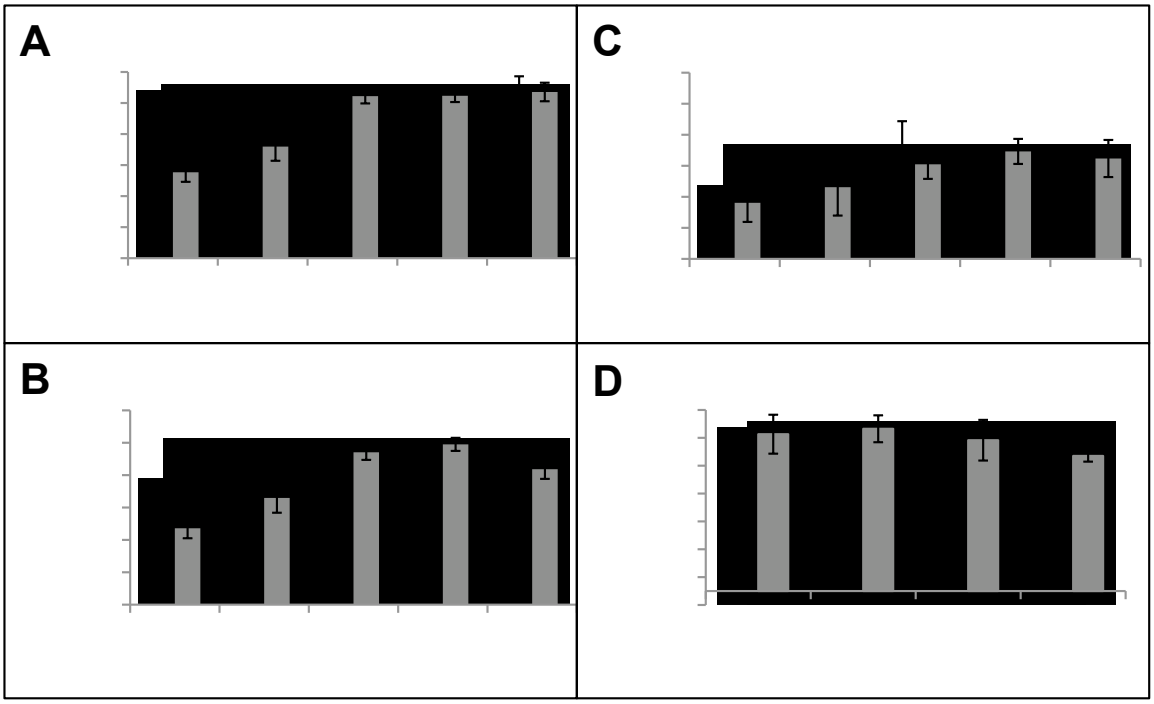

Figure 5.4 Cytotoxicity measurements of PTX, SPMs, and SMs in C4-2 prostate cancer cells. The graphs show C4-2 cell viability measured with a WST-1 assay after incubation with PTX or SPMs for (A) 24 hours, (B) 48 hours, and (C) 72 hours. Viability after incubation with SPMs (gray bars) and PTX (black bars) is shown as the percent of viable cells compared to control samples not incubated with particles or drug. Panel (D) shows the lack of cytotoxicity when C4-2 human prostate cancer cells were incubated with SIPP-micelles without drug (SMs) for 24 hours (black bars) and 48 hours (gray bars).

www.manaraa.com

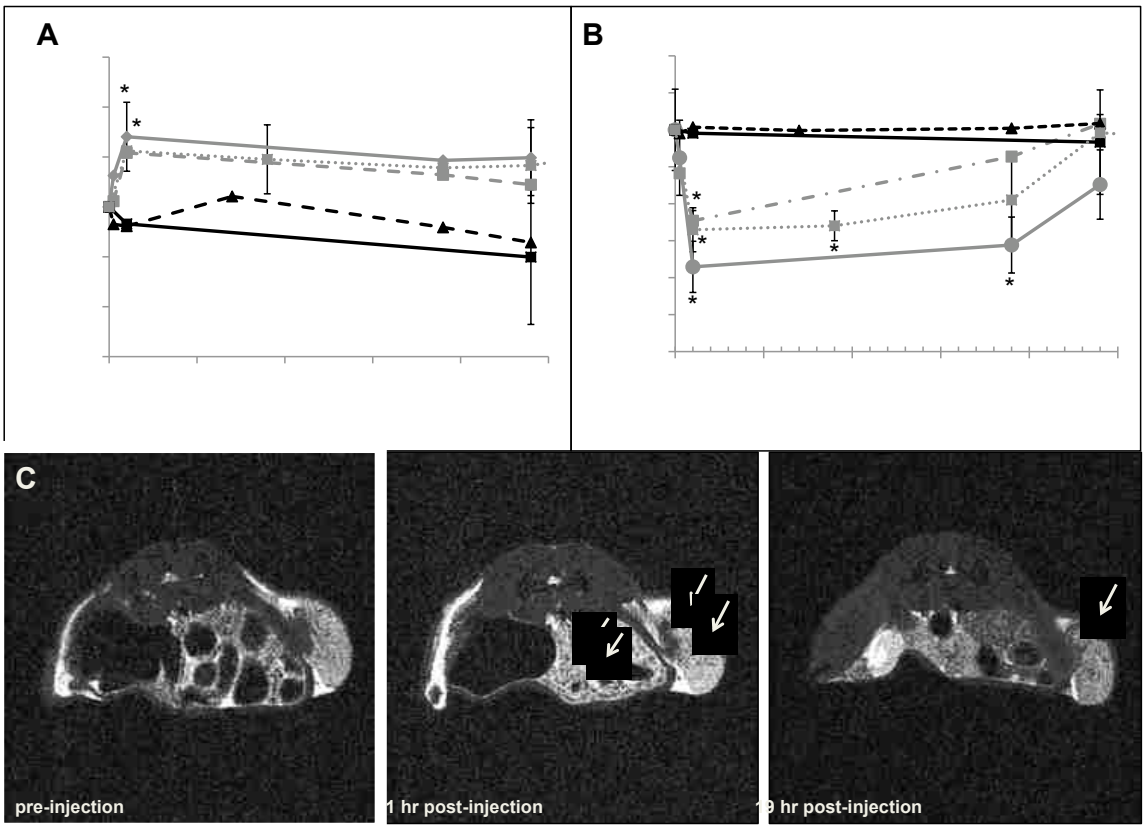

Figure 5.5 ***In vivo*** **MRI and contrast measurements of a mouse bearing a C4-2 xenograft.** Longitudinal (A) and transverse (B) contrast percent measured for mice bearing C4-2 xenografts and injected with either J591-SPMs (diamond, solid gray line), J591-SMs (square, dotted gray line), IgG-SPMs (square, dashed gray line), PTX only (triangle, dashed black line), or nothing (square, solid black line). Representative T_2-weighted MR images of a mouse injected with J591-SPMs are shown in (C). The arrows point to areas in the C4-2 xenograft that showed dark contrast enhancement at one hour post-injection in the middle frame and an area that still showed contrast enhancement 19 hours post-injection in the far right frame. * Corresponds to a significance of $p < 0.05$.

www.manaraa.com

the IgG-SPMs, as well as the J591-SMs, all showed contrast enhancement in T_1- and T_2-weighted MR images of the tumors after injection. The T_2 contrast was more pronounced and was retained in the tumors targeted with J591-SPMs and J591-SMs, whereas the contrast enhancement in the tumors of mice injected with non-targeted IgG-SPMs was lost more quickly.

Xenograft Growth Inhibition by SPMs. The tumor volumes of the mice were measured over time. The data in Figure 5.6 show that only the J591-SPMs and PTX were able to reduce the volume of tumors in the mice. The non-targeted IgG-SPMs did not significantly reduce the tumor burden in the animals, nor did the J591-SMs. None of the mice in the treatment or control groups showed significant differences in tissue weights or overall body weight over the course of the experiment (Figures 5.7 and 5.8). In contrast to the J591-SPM injected mice that showed no adverse effects of the treatment, PTX injected mice suffered from severe hemorrhaging around the tumor (Figure 5.9), two went blind, and one mouse was euthanized early due to neurological impairment that was evident because the mouse continuously circled in the cage and occasionally shook.

Twenty days after the injection of the treatments or controls (or at early exit timed points for the mice suffering from side effects) the mice were euthanized and the tumors and tissues were collected to quantify the amount of PTX and Pt in the tissues. From the data shown in Figure 5.10 it is evident that the significantly more PTX and Pt was found in the tumors from the J591-SPM

www.manaraa.com

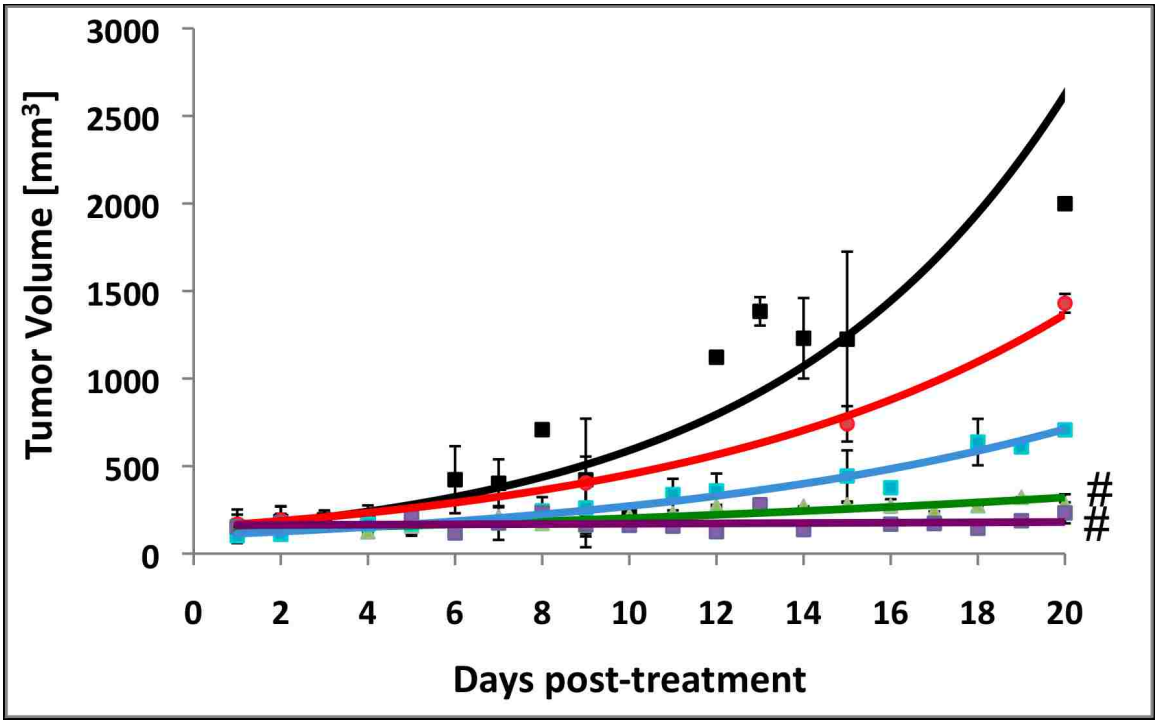

Figure 5.6 Tumor volume growth curves for nude mice bearing human C4-2 prostate cancer xenografts treated with various treatments or controls. (A) Black squares, no treatment controls. (B) Red squares, targeted SIPPs without drug, showing no effect on tumor growth. (C) Blue squares, SIPPs containing PTX conjugated to a control IgG antibody, showing no effect on tumor growth. (D) Green triangles, PTX alone, without SIPPs, showing the efficacy of this chemotherapeutic drug by itself. (E) Purple squares, SIPPs containing PTX, targeted to PSMA, showing that targeting specifically brings the drug to the tumors and prevents tumor growth. # corresponds to significance of $p < 0.05$.

www.manaraa.com

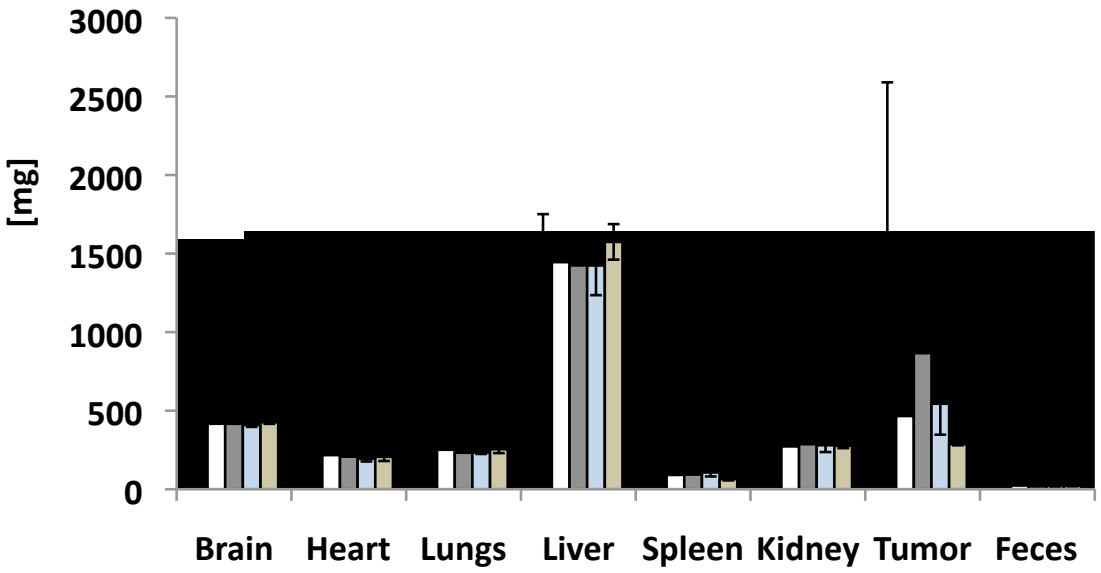

Figure 5.7 Tissue weights of mice bearing C4-2 xenografts that were injected with treatments or controls. Mice bearing C4-2 xenografts were injected with J591-SPMs (white bars), J591-SMs (gray bars), IgG-SPMs (blue bars), PTX alone (beige bars), or nothing (black bars) and 20 days later their tissues and tumors were collected and weighed. None of the mice showed significant differences in tissue weights post-mortem, although the mice injected with PTX alone, J591-SPMs, and IgG-SPMs showed decreased tumor mass compared to mice injected with SIPP-micelles without drug and mice that were not injected. * corresponds to significance of $p < 0.05$.

www.manaraa.com

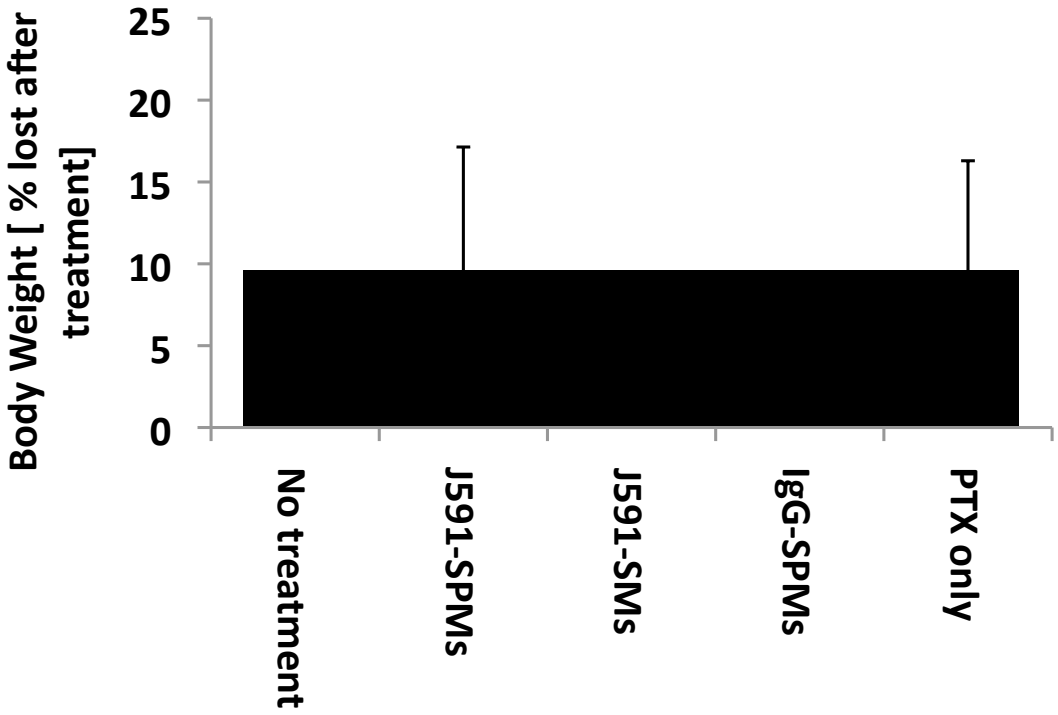

Figure 5.8 Body weights of mice bearing C4-2 xenografts that were injected with treatments or controls. Mice bearing C4-2 human prostate cancer cell xenografts were injected with the treatments or controls and weighed on the day of injection and on the day of euthanasia. None of the mice showed significant differences in loss of body weight over the 20 days.

www.manaraa.com

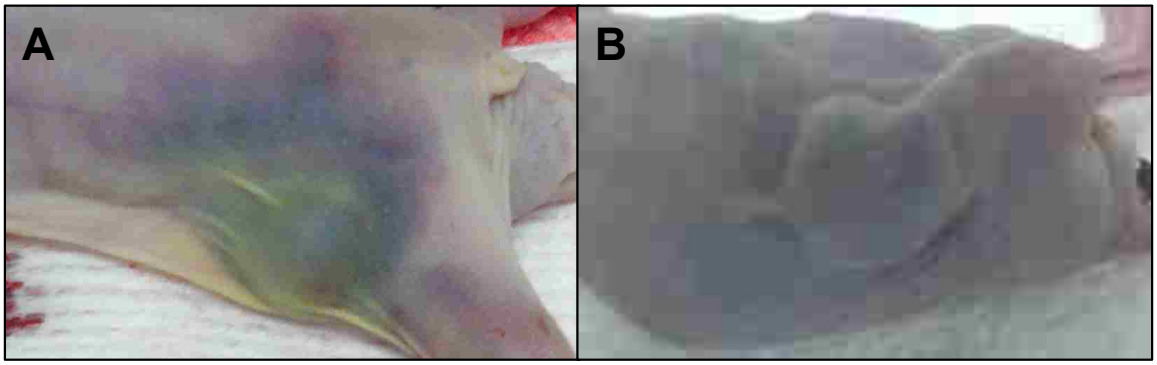

Figure 5.9 Hematoma around the tumors of mice injected with PTX alone. Representative images are shown for mice injected with PTX alone (A) and J591-SPMs (B) taken post-mortem. The mice injected with PTX alone clearly had extensive hematoma around the tumors and all along the right flanks, whereas the mice injected with J591-SPMs did not have this side effect, suggesting that in addition to targeting the drug, encapsulation of the drug also reduced side effects.

www.manaraa.com

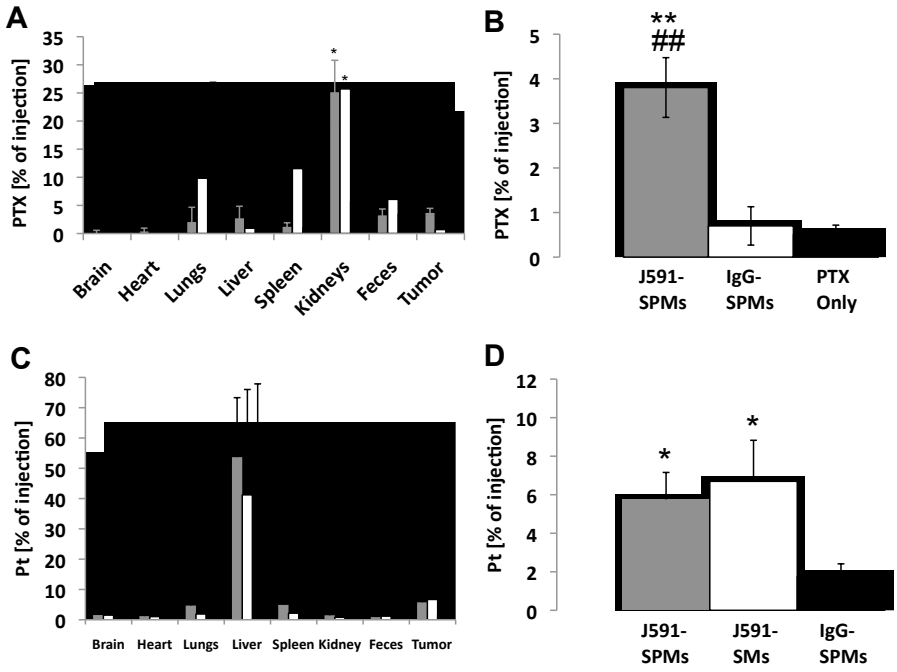

Figure 5.10 Tissue biodistribution of PTX and platinum in mice bearing C4-2 xenografts and injected with treatments or controls. Mice were injected with PTX alone (white bars), J591-SPMs (black bars), or IgG-SPMs (gray bars) and 20 days post-injection their various organs and tumors were collected and PTX was measured as percent of the injected dose (A). Significantly more PTX was measured in the tumors of mice injected with J591-SPMs, compared with non-targeted SPMs and PTX alone (B). Likewise, the biodistribution of platinum, from the SIPPs, in the tissues and tumors were measured, using ICP, as percent of the injected dose (C). Again, significantly more platinum was measured in the tumors of mice injected with J591-SPMs, compared with non-targeted SPMs and PTX alone (D).. * and # correspond to significance of $p < 0.05$ compared to PTX alone or IgG-SPMs, respectively. ** and ## correspond to significance of $p < 0.07$ compared to PTX alone or IgG-SPMs, respectively.

www.manaraa.com

injected mice compared to PTX alone or in the tumors from the IgG-SPM injected mice. Also, the J591-targeting appeared to have decreased the amount of drug and particles in the spleen, compared to the IgG-SPMs and additionally decreased the amount of drug measured in the brains of the mice, compared with PTX injected mice.

Discussion

Although superparamagnetic iron oxide nanoparticles (SPIONs) are the most common type of contrast agents used in contrast agent-enhanced magnetic resonance imaging (MRI), nanoparticles with increased MRI relaxivities are needed in order to increase the contrast enhancement in MRI applied to various medical conditions including cancer. We have previously reported that superparamagnetic iron platinum nanoparticles (SIPPs) are superior contrast agents for MRI (29,30). The next important step was to determine if the SIPPs could be beneficial as *in vivo* imaging agents and to measure any cytotoxicity of the particles. We have shown both *in vitro* (Figure 5.4) and *in vivo* (Figures 5.7, 5.8, 5.9) that the encapsulated iron platinum particles did not have any significant toxic effects on cells (over 48 hours) or mice (over 20 days). Platinum salts are known to be toxic (40-42), but the platinum in our particles is metallic and contained in a crystal structure alloyed with iron. Upon dissociation from the crystal, the Pt would still be metallic and not in the form of a salt. Pt metal is chemically inert.

www.manaraa.com

The biodistribution data (Figure 5.10) for our SIPPs suggested that, except for the tumors, the platinum was primarily retained in the kidney, spleen, liver, and lungs. An important point when considering further development of SIPPs and SPMs for clinical applications was that both platinum and PTX were found in the feces of the mice 20 days post-injection. This showed that the Pt and PTX were excreted from the mice in their feces and, although a large percentage of both metal and drug were retained in the body 20 days post-injection, the Pt and PTX were eventually eliminated. It would be of interest to perform biodistribution studies for at least a year to follow the complete excretion of platinum.

Interestingly, both the J591-targeted micelles and the non-targeted IgG-micelle controls caused contrast enhancement in the tumors (Figure 5.5). Nonetheless, It was clear that the tumors of mice injected with the J591-SPMs had a higher concentration of both PTX and Pt in the tumors (Figure 5.10). This, in addition to the fact the contrast enhancement in tumors of IgG-SPM injected mice was lost more quickly in comparison to J591-SPM mice (Figure 5.5), suggested that the EPR effect is adequate for bringing the contrast agent into the tumor for MR imaging. In contrast, the data in Figure 5.6 showed that these IgG-SPM injected mice did not undergo a therapeutic response to the non-targeted treatment. This suggested that, although the concentration of micelles in the tumors due to the EPR effect was high enough to generate MRI contrast enhancement, it did not lead to accumulation of enough micelles to prevent increases in tumor volume over time. It was also possible that the IgG-SPMs were not endocytosed and, therefore, the drug did not cause cell death because

www.manaraa.com

it did not reach the cytoplasm. Paclitaxel was a microtubule stabilizer that inhibited cell division, leading to cell death (43). The confocal images in Figure 5.3 showed that only the J591-SPMs were internalized into the C4-2 cells *in vitro*, whereas the IgG-SPMs were not. This strongly suggested that, *in vivo*, only the J591-targeted micelles were able to enter into the cells, where the drug was released.

In order to cause MRI contrast, the particles must only be attached to the vasculature and/or cells of the tumor, but in order to cause cell death, the particles must actually have been taken up by the cells. This could explain some of the discrepancies seen in the literature relating to the question of whether or not active targeting works (44). Our data suggested that an important distinction should be made between whether nanoparticles generated tumor contrast or were actually therapeutic. Importantly, the growth of the human prostate cancer xenografts in the nude mice was only inhibited in the mice treated with either PTX or J591-SPMs. In contrast to the PTX injected mice (Figure 5.9), the J591-SPM mice did not suffer from any noticeable side effects or complications over the 20 days that the mice were followed post-injection.

J591, a monoclonal antibody raised against PSMA, has been used in numerous clinical trials for prostate cancer (45-50). Our data showed that J591 conjugated to PTX-loaded micelles, specifically targeted the micelles to human prostate cancer cells and prevented tumor growth in a PSMA-dependent manner. PSMA is highly expressed in almost all prostate cancer primary and metastatic tumors (51). Our data suggested that drug-loaded micelles targeted to PSMA

www.manaraa.com

could successfully treat prostate cancer tumors while possibly reducing the side effects that commonly seen when using chemotherapeutics alone. Moreover, PSMA has been shown to be expressed in the neovasculature of almost all solid tumors, but not in healthy vasculature (51), supporting the idea that PSMA-targeting may be beneficial not only as a prostate cancer targeting motif but as a general cancer target. In addition to the specific, targeted killing of PSMA-positive prostate cancer cells, ours was also the first report on encapsulating SIPPs with a chemotherapeutic drug in a mixture of functionalized and fluorescent phospholipids to produce multifunctional, iron platinum, stealth immunomicelles for the specific MRI and therapy of cancer.

Acknowledgments

This research was supported in part by funding from NIH (5RO1CA123194 to Laurel O. Sillerud) and the NCI New Mexico Cancer Nanotechnology Training Center (NIH R25CA153825 supporting Robert M. Taylor). Portions of this work were performed at the Center for Integrated Nanotechnologies, a US Department of Energy, Office of Basic Energy Sciences, user facility. Sandia National Laboratories is a multi-program laboratory operated by The Sandia Corporation, a Lockheed-Martin Company, for the US Department of Energy under Contract No. DE-AC04-94AL85000. MRI relaxivities were measured at the BRaIN Imaging Center, Albuquerque, NM. TEM images were generated at the University of New Mexico Electron Microscopy Facility. Some experiments used the facilities provided by the Keck-UNM Genomics Resource, a facility supported

www.manaraa.com

by grants from the WM Keck Foundation, the State of New Mexico, and the UNM Cancer Research and Treatment Center. We gratefully acknowledge the assistance of Dr. Medhi Ali of the Earth and Planetary Sciences Department at UNM, for the ICP-OES analyses, of Dr. Stephen Jett of the UNM Electron Microscopy Facility, and of Dr. Dale Huber of the Center for Integrated Nanotechnologies.

References

1. Siegel R, Naishadham D, Jemal A. Cancer statistics, 2012. CA Cancer J Clin 2012;62(1):10-29.

2. Burke MA, Lowrance W, Perczek R. Emotional and cognitive burden of prostate cancer. Urol Clin North Am 2003;30(2):295-304.

3. Moul JW, Dawson N. Quality of life associated with treatment of castration-resistant prostate cancer: a review of the literature. Cancer Invest 2012;30(1):1-12.

4. Beltran H, Beer TM, Carducci MA, de Bono J, Gleave M, Hussain M, Kelly WK, Saad F, Sternberg C, Tagawa ST, Tannock IF. New therapies for castration-resistant prostate cancer: efficacy and safety. Eur Urol 2011;60(2):279-290.

5. Dayyani F, Gallick GE, Logothetis CJ, Corn PG. Novel therapies for metastatic castrate-resistant prostate cancer. J Natl Cancer Inst 2011;103(22):1665-1675.

6. Gomella LG, Gelpi F, Kelly WK. New treatment options for castrate-resistant prostate cancer: a urology perspective. Can J Urol 2011;18(4):5767-5777.

7. Petrylak DP. Current clinical trials in castrate-resistant prostate cancer. Curr Urol Rep 2011;12(3):173-179.

8. Abeylath SC, Ganta S, Iyer AK, Amiji M. Combinatorial-designed multifunctional polymeric nanosystems for tumor-targeted therapeutic delivery. Acc Chem Res 2011;44(10):1009-1017.

www.manaraa.com

9. Ho D, Sun X, Sun S. Monodisperse magnetic nanoparticles for theranostic applications. Acc Chem Res 2011;44(10):875-882.

10. Kievit FM, Zhang M. Surface engineering of iron oxide nanoparticles for targeted cancer therapy. Acc Chem Res 2011;44(10):853-862.

11. Koo H, Huh MS, Sun IC, Yuk SH, Choi K, Kim K, Kwon IC. In vivo targeted delivery of nanoparticles for theranosis. Acc Chem Res 2011;44(10):1018-1028.

12. Namiki Y, Fuchigami T, Tada N, Kawamura R, Matsunuma S, Kitamoto Y, Nakagawa M. Nanomedicine for cancer: lipid-based nanostructures for drug delivery and monitoring. Acc Chem Res 2011;44(10):1080-1093.

13. Shi J, Xiao Z, Kamaly N, Farokhzad OC. Self-assembled targeted nanoparticles: evolution of technologies and bench to bedside translation. Acc Chem Res 2011;44(10):1123-1134.

14. Yoo D, Lee JH, Shin TH, Cheon J. Theranostic magnetic nanoparticles. Acc Chem Res 2011;44(10):863-874.

15. Puri A, Blumenthal R. Polymeric lipid assemblies as novel theranostic tools. Acc Chem Res 2011;44(10):1071-1079.

16. Sawant RR, Torchilin VP. Multifunctionality of lipid-core micelles for drug delivery and tumour targeting. Mol Membr Biol 2010;27(7):232-246.

17. Arias JL, Clares B, Morales ME, Gallardo V, Ruiz MA. Lipid-based drug delivery systems for cancer treatment. Curr Drug Targets 2011;12(8):1151-1165.

18. Estella-Hermoso de Mendoza A, Campanero MA, Mollinedo F, Blanco-Prieto MJ. Lipid nanomedicines for anticancer drug therapy. J Biomed Nanotechnol 2009;5(4):323-343.

19. Florence AT, Jani PU. Novel oral drug formulations. Their potential in modulating adverse effects. Drug Saf 1994;10(3):233-266.

20. Peng XH, Qian X, Mao H, Wang AY, Chen ZG, Nie S, Shin DM. Targeted magnetic iron oxide nanoparticles for tumor imaging and therapy. Int J Nanomedicine 2008;3(3):311-321.

21. Akhter S, Ahmad Z, Singh A, Ahmad I, Rahman M, Anwar M, Jain GK, Ahmad FJ, Khar RK. Cancer targeted metallic nanoparticle: targeting

المنارة للاستشارات
www.manaraa.com

overview, recent advancement and toxicity concern. Curr Pharm Des 2011;17(18):1834-1850.

22. Hirsjarvi S, Passirani C, Benoit JP. Passive and active tumour targeting with nanocarriers. Curr Drug Discov Technol 2011;8(3):188-196.

23. Zhang C, Liu T, Gao J, Su Y, Shi C. Recent development and application of magnetic nanoparticles for cell labeling and imaging. Mini Rev Med Chem 2010;10(3):193-202.

24. Lin MM, Kim do K, El Haj AJ, Dobson J. Development of superparamagnetic iron oxide nanoparticles (SPIONS) for translation to clinical applications. IEEE Trans Nanobioscience 2008;7(4):298-305.

25. Shubayev VI, Pisanic TR, 2nd, Jin S. Magnetic nanoparticles for theragnostics. Adv Drug Deliv Rev 2009;61(6):467-477.

26. Mailander V, Landfester K. Interaction of nanoparticles with cells. Biomacromolecules 2009;10(9):2379-2400.

27. Gandhi SN, Brown MA, Wong JG, Aguirre DA, Sirlin CB. MR contrast agents for liver imaging: what, when, how. Radiographics 2006;26(6):1621-1636.

28. Tsukada H. [Application of pre-clinical PET imaging for drug development]. Nihon Shinkei Seishin Yakurigaku Zasshi 2011;31(5-6):231-237.

29. Taylor RM, Huber, D.L., Monson, T.C., Esch, V., and Sillerud, L.O. Structural and magnetic characterization of superparamagnetic iron platinum nanoparticle contrast agents for magnetic resonance imaging. J Vac Sci Technol B 2012;30(2).

30. Taylor RM, Huber DL, Monson TC, Ali AM, Bisoffi M, Sillerud LO. Multifunctional iron platinum stealth immunomicelles: targeted detection of human prostate cancer cells using both fluorescence and magnetic resonance imaging. J Nanopart Res 2011;13(10):4717-4729.

31. Rasband WS. ImageJ. US National Institutes of Health, Betesda, Maryland, USA, http//rsbinfonihgov/ij/ 1997-2009.

32. Gossuin Y, Gillis P, Hocq A, Vuong QL, Roch A. Magnetic resonance relaxation properties of superparamagnetic particles. Wiley Interdiscip Rev Nanomed Nanobiotechnol 2009;1(3):299-310.

www.manaraa.com

33. Huang J, Zhong X, Wang L, Yang L, Mao H. Improving the magnetic resonance imaging contrast and detection methods with engineered magnetic nanoparticles. Theranostics 2012;2(1):86-102.

34. Lee JH, Huh YM, Jun YW, Seo JW, Jang JT, Song HT, Kim S, Cho EJ, Yoon HG, Suh JS, Cheon J. Artificially engineered magnetic nanoparticles for ultra-sensitive molecular imaging. Nat Med 2007;13(1):95-99.

35. Carroll MR, Huffstetler PP, Miles WC, Goff JD, Davis RM, Riffle JS, House MJ, Woodward RC, St Pierre TG. The effect of polymer coatings on proton transverse relaxivities of aqueous suspensions of magnetic nanoparticles. Nanotechnology 2011;22(32):325702.

36. Diezi TA, Bae Y, Kwon GS. Enhanced stability of PEG-block-poly(N-hexyl stearate l-aspartamide) micelles in the presence of serum proteins. Mol Pharm 2010;7(4):1355-1360.

37. Kastantin M, Missirlis D, Black M, Ananthanarayanan B, Peters D, Tirrell M. Thermodynamic and kinetic stability of DSPE-PEG(2000) micelles in the presence of bovine serum albumin. J Phys Chem B 2010;114(39):12632-12640.

38. Lu J, Owen SC, Shoichet MS. Stability of Self-Assembled Polymeric Micelles in Serum. Macromolecules 2011;44(15):6002-6008.

39. Taylor RM, Severns V, Brown DC, Bisoffi M, Sillerud LO. Prostate cancer targeting motifs: Expression of alpha(nu) beta(3) , neurotensin receptor 1, prostate specific membrane antigen, and prostate stem cell antigen in human prostate cancer cell lines and xenografts. Prostate 2011.

40. Couraud S, Planus C, Rioufol C, Mornex F. [Platinum salts hypersensitivity]. Rev Pneumol Clin 2008;64(1):20-26.

41. Cristaudo A, Sera F, Severino V, De Rocco M, Di Lella E, Picardo M. Occupational hypersensitivity to metal salts, including platinum, in the secondary industry. Allergy 2005;60(2):159-164.

42. Touraine F, Sainte Laudy J, Boumediene A, Ndikumwenayo F, Decroisette C, Melloni B, Vergnenegre A, Bonnaud F. [Investigation of allergic reactions to platinum salts]. Rev Mal Respir 2006;23(5 Pt 1):458-462.

43. Zhao J, Kim JE, Reed E, Li QQ. Molecular mechanism of antitumor activity of taxanes in lung cancer (Review). Int J Oncol 2005;27(1):247-256.

www.manaraa.com

44. Nie S. Understanding and overcoming major barriers in cancer nanomedicine. Nanomedicine (Lond) 2010;5(4):523-528.

45. Akhtar NH, Pail O, Saran A, Tyrell L, Tagawa ST. Prostate-specific membrane antigen-based therapeutics. Adv Urol 2012;2012:973820.

46. Bander NH, Trabulsi EJ, Kostakoglu L, Yao D, Vallabhajosula S, Smith-Jones P, Joyce MA, Milowsky M, Nanus DM, Goldsmith SJ. Targeting metastatic prostate cancer with radiolabeled monoclonal antibody J591 to the extracellular domain of prostate specific membrane antigen. J Urol 2003;170(5):1717-1721.

47. Bayes M, Rabasseda X, Prous JR. Gateways to clinical trials. Methods Find Exp Clin Pharmacol 2007;29(6):427-437.

48. Nanus DM, Milowsky MI, Kostakoglu L, Smith-Jones PM, Vallabahajosula S, Goldsmith SJ, Bander NH. Clinical use of monoclonal antibody HuJ591 therapy: targeting prostate specific membrane antigen. J Urol 2003;170(6 Pt 2):S84-88; discussion S88-89.

49. Rice SL, Roney CA, Daumar P, Lewis JS. The next generation of positron emission tomography radiopharmaceuticals in oncology. Semin Nucl Med 2011;41(4):265-282.

50. Tagawa ST, Beltran H, Vallabhajosula S, Goldsmith SJ, Osborne J, Matulich D, Petrillo K, Parmar S, Nanus DM, Bander NH. Anti-prostate-specific membrane antigen-based radioimmunotherapy for prostate cancer. Cancer 2010;116(4 Suppl):1075-1083.

51. Chang SS, O'Keefe DS, Bacich DJ, Reuter VE, Heston WD, Gaudin PB. Prostate-specific membrane antigen is produced in tumor-associated neovasculature. Clin Cancer Res 1999;5(10):2674-2681.

www.manaraa.com

Chapter 6

Conclusions and future directions

In 2011, more than 200,000 men were newly diagnosed with and over 30,000 men died due to prostate cancer in the United States, making carcinoma of the prostate the second most lethal cancer in men in the United States (1,2). Accurate detection methods are important for all aspects of the clinical management of prostate cancer, including diagnosis, risk assessment, staging, and prognosis. Such methods will result in individualized and efficacious treatments for patients at risk for prostate cancer or for its progression. Many of these tasks are currently managed by determination of the serum biomarker prostate specific antigen (PSA). For example, serum PSA levels are used to evaluate prostate cancer risk and progression, and justify confirmatory biopsies to diagnose the presence of malignancy. However, biopsies have inherent risks such as bleeding and infection (3), and cancer is not detected (false negative cases) in 30-50% of biopsies in patients with subsequently confirmed malignancy due to small and inconspicuous lesions (4). Another major issue is that ~25% - 40% of patients are over-diagnosed using current detection methods leading to superfluous biopsies (3). These findings indicate that detection and staging of prostate cancer needs to be improved.

SPIONs are the most common type of contrast agents used in contrast agent-enhanced MRI (5). Although SPIONs cause negative contrast in the MR images, the signal enhancement is still lower than other common imaging

www.manaraa.com

techniques (6). Therefore, novel nanoparticles with increased MRI relaxivities are needed in order to increase the signal enhancement in MRI and the detection of cancer, using lower doses of the contrast agents. Additionally, the specific targeting of contrast agents and therapeutics to cells of interest is now widely accepted as a cornerstone to the development of individualized diagnosis and treatment.

The overarching hypothesis of this dissertation is that SIPPs and a hydrophobic chemotherapeutic drug, paclitaxel, encapsulated in a mixture of PEGylated, fluorescent-, and biotin-functionalized phospholipids and conjugated to a monoclonal antibody against PSMA would specifically target prostate cancer cells, be superior MRI contrast agents for prostate cancer detection (compared to SPIONs), and have increased therapeutic efficacy *in vivo* compared to Paclitaxel alone. This hypothesis was evaluated in four specific aims and the conclusions of these studies are summarized below, with some possible future directions.

In specific aim one (addressed in Chapter 2), expression differences in receptor signatures among several human prostate cancer cell lines and xenografts as a function of tumorigenicity were examined to determine the best receptor and cell line to use in the nanoparticle targeting studies, both *in vitro* and *in vivo*. Membrane receptors are frequent targets of cancer therapeutic and imaging agents. However, promising *in vitro* results often do not translate to *in vivo* clinical applications. Therefore, to better understand this obstacle messenger RNA and protein expression levels for integrin $\alpha_v\beta_3$, neurotensin receptor 1 (NTSR1), prostate specific membrane antigen (PSMA), and prostate

www.manaraa.com

stem cell antigen (PSCA) were measured in LNCaP, C4-2, and PC-3 human prostate cancer cell lines and in murine xenografts using quantitative reverse transcriptase polymerase chain reaction, flow cytometry, and immunohistochemistry. Stable expression patterns were observed for integrin α_v and PSMA in all cells and corresponding xenografts. Integrin β_3 mRNA expression was greatly reduced in C4-2 xenografts and greatly elevated in PC-3 xenografts compared with the corresponding cultured cells. NTSR1 mRNA expression was greatly elevated in LNCaP and PC-3 xenografts. PSCA mRNA expression was elevated in C4-2 xenografts when compared with C4-2 cells cultured *in vitro*. Furthermore, at the protein level, PSCA was re-expressed in all xenografts compared with cells in culture.

The regulation of mRNA and protein expression of the cell-surface target proteins $\alpha_v\beta_3$, NTSR1, PSMA, and PSCA, in prostate cancer cells with different tumorigenic potential, was influenced by factors of the microenvironment, differing between cell cultures and murine xenotransplants. Integrin $\alpha_v\beta_3$, NTRS1 and PSCA mRNA expression increased with tumorigenic potential, but mRNA expression levels for these proteins do not translate directly to equivalent expression levels of membrane bound protein.

Although, it was reasonable to expect that the efficacy of imaging and therapeutic agents could be improved by using multiple targeting motifs on a single nanoparticle, because this would markedly increase the affinity of the nanoparticles for their targets, we found that PSMA was, by far, the most highly expressed and consistent receptor useful for both *in vitro* and *in vivo* studies. As,

www.manaraa.com

the overarching hypothesis was to promote a novel agent from synthesis, through *in vitro* characterizations, all the way to *in vivo* studies; I determined that it was best to simply use a single PSMA-targeting motif. Furthermore, the C4-2 cell line had the highest number of PSMA receptors expressed, with over 1.4 million per C4-2 cell, *in vitro.* Additionally, xenografts produced using C4-2 human prostate cancer cells produced high amounts of PSMA mRNA and grew faster than the LNCaP xenografts. Therefore, the C4-2 cell line was chosen as our model cell line for the subsequent *in vitro* and *in vivo* specific aims.

In specific aim two (addressed in Chapters 3 and 4), the synthesis, from simple salts, and the physical characterization of SIPPs, suitable for use as contrast agents in MRI, was achieved. The properties of these particles were determined by means of TEM, TGA, ICP, SQUID magnetometry, and NMR relaxivity at 4.7 Tesla. TEM showed that the diameters of the particles ranged from 9.3 nm to 10 nm, depending on the mole ratio of iron to platinum precursors, and on the concentration of Octadecylamine used in their preparation. The iron to platinum stoichiometry determined by ICP varied from 1.4:1 to 3.7:1 and was similarly dependant on the initial mole ratios of iron and platinum salts, as well as on the concentration of ODA in the reaction. SQUID magnetometry showed that the SIPPs were superparamagnetic and had magnetic moments that increased with increasing iron content from 62 to 72 A m^2/kg Fe. The measured relaxivities of the SIPPs at 4.7 Tesla were higher than commercially available SPIONs, suggesting that the SIPPs were superior contrast agents for T_2-weighted MRI.

www.manaraa.com

In specific aim three (addressed in Chapters 4 and 5), synthesis of SIPPs and subsequent encapsulation using PEGylated phospholipids to create stealth immunomicelles (DSPE-SIPPs) that can be specifically targeted to human prostate cancer cell lines and detected using both MRI and fluorescence imaging was accomplished. The SIPP cores were optimized and SIPP cores and DSPE-SIPPs were 8.5 nm ± 1.6 nm and 42.9 nm ± 8.2 nm in diameter. The SIPPs had a magnetic moment of 120 A m^2/kg iron. J591, a monoclonal antibody against PSMA, was conjugated to the DSPE-SIPPs (J591-DSPE-SIPPs) and specific targeting of J591-DSPE-SIPPs to PSMA-expressing human prostate cancer cell lines was demonstrated using fluorescence confocal microscopy. The transverse relaxivity of the DSPE-SIPPs, measured at 4.7 Tesla, was 300.6 ± 8.5 s^{-1} mM^{-1}, which is 13-fold better than commercially available SPIONs (23.8 ± 6.9 s^{-1} mM^{-1}) and ~3-fold better than the reported relaxivities for Feridex® and Resovist®. Our data suggested that J591-DSPE-SIPPs specifically targeted human prostate cancer cells *in vitro*, were superior contrast agents in T_2-weighted MRI, and could be detected using fluorescence imaging. To our knowledge, this was the first report on the synthesis of multifunctional SIPP micelles and their use for the specific detection of prostate cancer.

Additionally (Chapter 5), I encapsulated the SIPPs with PTX in a mixture of PEGylated, fluorescent, and biotin-functionalized phospholipids to create multifunctional SIPP-PTX micelles (SPMs) that were conjugated to the anti-PSMA antibody for the specific targeting, MRI, and therapy of human prostate cancer xenografts in mice. SPMs were 45 ± 25 nm in diameter and composed of

www.manaraa.com

161 ± 23 μg/mL iron, 247 ± 33 μg/mL platinum, and 703 ± 206 μg/mL PTX. Drug release measurements showed that, at 37 °C, half of the PTX was released in 30.2 hours in serum and two times faster in saline. Binding assays suggested that PSMA-targeted SPMs specifically bound to C4-2 human prostate cancer cells *in vitro* and released the PTX into the cells. *In vitro*, PTX was found to be 2.2 and 1.6 times more cytotoxic than SPMs, to C4-2 cells, at 24 and 48 hours incubation, respectively. At 72 hours incubation PTX and SPMs were equally cytotoxic. SPMs had MRI transverse relaxivities of 389 ± 15.5 Hz/mM iron.

In specific aim four (Chapter 5), PTX alone or SIPP-micelles with and without drug were injected in athymic nude mice bearing C4-2 xenografts in their flanks. We showed, both *in vitro* and *in vivo,* that the encapsulated iron platinum particles did not have any significant toxic effects on cells (over 48 hours) or mice (over 20 days). Platinum salts were known to be toxic (7-9), but the platinum in our particles was contained in a crystal structure with iron. Very similar to previously reported data for SPIONs, the biodistribution data for our SIPPs suggested that the platinum that is not targeted to the tumor primarily resides in the kidney, spleen, liver, and lungs. A crucial point to the further development of SIPPs for clinical applications was that we found platinum in the feces of the mice 20 days post-injection. This suggested that the platinum was secreted from the mice in their feces and not retained for longer periods of time in the tissues.

Interestingly, both the J591-targeted micelles and the non-targeted IgG-micelle controls caused contrast enhancement in the tumors. It was clear that the tumors of mice injected with the J591-SPMs had a higher concentration of

www.manaraa.com

both PTX and Pt in the tumors, though. This, in addition to the fact the contrast enhancement in tumors of IgG-SPM injected mice was quickly lost in comparison to J591-SPM mice, suggested that the enhanced permeation and retention (EPR) effect was adequate for bringing the contrast agent into the tumor for MR imaging. In contrast, these same IgG-SPM injected mice did not show a therapeutic response to the non-targeted treatment. This suggested that although the concentration of micelles, due to EPR, was enough to cause MRI contrast enhancement, it did not lead to accumulation of enough micelles to cause tumor volume reduction. It was also possible that the IgG-SPMs were not endocytosed and, therefore, the drug could not cause cell death. Confocal images showed that only the J591-SPMs were internalized into the C4-2 cells *in vitro*, whereas the IgG-SPMs were not. This strongly suggested that, *in vivo*, only the J591-targeted micelles were able to enter into the cells, where the drug was released. In order to cause MRI contrast, the particles must only be attached to the vasculature and/or cells of the tumor, but in order to cause cell death, the particles must actually be taken up by the cells. This could explain some of the discrepancies in the literature of whether active targeting works. It is important to understand whether the authors were discussing contrast or therapy, as an important finding in this dissertation is that this is a critical distinction.

Importantly, the human prostate cancer xenografts in the nude mice were only reduced in mice treated with either PTX or J591-SPMs. In contrast to the PTX injected mice, the J591-SPM mice did not suffer from any noticeable side effects or complications over the 20 days that the mice were followed. Our data

www.manaraa.com

suggested that J591 conjugated to PTX-loaded micelles, specifically targeted the micelles to human prostate cancer cells and caused reduction in tumor volume in a PSMA-dependent manner. PSMA is highly expressed in almost all prostate cancer primary and metastatic tumors (10). Our data suggested that drug-loaded micelles targeted to PSMA could successfully treat prostate cancer tumors while possibly reducing side effects that are commonly seen when using chemotherapeutics alone. In addition to the specific, targeted killing of PSMA-positive prostate cancer cells, this dissertation research was novel in that it was the first report on encapsulating SIPPs with a chemotherapeutic drug in a mixture of functionalized and fluorescent phospholipids to produce multifunctional, iron platinum, stealth immunomicelles for the specific MRI and therapy of cancer.

The dissertation offers significant pre-clinical advancement of a new therapeutic modality for the treatment of early and advanced stage prostate cancer. In addition to the therapeutic aspect of the project, the superparamagnetic component would allow for the detection of prostate cancer cells, using MRI. This technology would allow for the extraordinary opportunity to begin treating a tumor at the very instant that it is detected. The interdisciplinary project was pre-clinical, but conclusions drawn from both the *in vitro* and *in vivo* specific aims provided a strong platform from which the diagnostic and therapeutic nanoparticles could be optimized for more efficient delivery and increased efficacy. This research, along with future optimization, should pave the way for a clinical trial of the therapeutic and diagnostic SIPP micelles. The ultimate goal in undertaking this pre-clinical research was to reduce death and

www.manaraa.com

suffering form prostate cancer by providing a non-invasive means to both detect and treat primary and metastatic prostate cancer.

Several ideas that have been born from this dissertation research warrant future studies. For one, longer biodistribution studies following the excretion of platinum are needed. Although, I followed the mice for 20 days post-injection of the SIPP-micelles without any noticeable side effects, it is plausible that toxic effects may be seen over a longer time course. Additionally, it is imperative to determine what amount of the platinum will be excreted and how long (i.e. months or years) the residual platinum will be retained in the organs. An interesting future endeavor would be to employ the resources of the Nanotechnology Characterization Laboratory (NCL). The NCL was developed by the National Cancer Institute (NCI) to perform preclinical efficacy and toxicity testing of nanoparticles (http://ncl.cancer.gov). The NCL would send the SIPP-micelles through a battery of *in vitro* and *in vivo* cytotoxicity and biocompatibility characterizations over the course of one year, greatly increasing the rate at which these particles could possibly be applied in clinical trials.

Another important future study would be to determine if a multifunctional approach might be required in order to detect and treat advanced tumors that are characterized by increased heterogeneity of target antigen expression (11). We have shown (Chapter 2) that the membrane receptor expression profiles of prostate cancer cells were altered with analogous changes in tumorigenic potential and that these alterations may comprise signatures of the tumorigenic state. Moreover, these membrane receptor signatures were altered for *in vitro*

www.manaraa.com

and *in vivo* models. Therefore, targeting nanoparticles, diagnostics, and therapeutics with multiple antibodies or peptides against PSMA as well as $\alpha_v\beta_3$, NTSR1, and/or PSCA may be more beneficial in diagnosing and treating early stage prostate cancer and CRPC than PSMA targeting alone. Imaging and therapeutic agents simultaneously directed to multiple targets expressed by cancer cells should show increased affinities, effectiveness, and specificities when compared with monofunctional agents. These targeting strategies could be tested in suitable prostate cancer cell models with well-characterized phenotypes, such as the human cell lines LNCaP, C4-2, and PC-3, which feature increasing tumorigenic potential and are widely-used in basic and pre-clinical research (12,13).

In summary, this research shows that SIPPs can be synthesized using safer methods than previously described and encapsulated with PTX in a mixture of PEGylated, fluorescent, and functionalized phospholipids to create multifunctional, iron platinum, stealth immunomicelles for the specific detection and therapy of prostate cancer. These SIPP-micelles were superior to SPIONs for T_2-weighted MRI and prevented prostate cancer xenograft growth, with comparable efficacy to PTX alone, in a PSMA-dependent manner without observable side effects.

www.manaraa.com

References

1. Jemal A, Siegel R, Xu J, Ward E. Cancer statistics, 2010. CA Cancer J Clin 2010;60(5):277-300.

2. Siegel R, Naishadham D, Jemal A. Cancer statistics, 2012. CA Cancer J Clin 2012;62(1):10-29.

3. Andrew W, Wender RC, Etzioni RB, Thompson IM, D'Amico AV, Volk RJ, Brooks DD, Dash C, Guessous I, Andrews K, DeSantis C, Smith RA. American Cancer Society Guideline for the Early Detection of Prostate Cancer. CA Cancer J Clin 2010;60(2):70-98.

4. Rabbani F, Stroumbakis N, Kava BR, Cookson MS, Fair WR. Incidence and clinical significance of false-negative sextant prostate biopsies. J Urol 1998;159(4):1247-1250.

5. Zhang C, Liu T, Gao J, Su Y, Shi C. Recent development and application of magnetic nanoparticles for cell labeling and imaging. Mini Rev Med Chem 2010;10(3):193-202.

6. Lee JH, Huh YM, Jun YW, Seo JW, Jang JT, Song HT, Kim S, Cho EJ, Yoon HG, Suh JS, Cheon J. Artificially engineered magnetic nanoparticles for ultra-sensitive molecular imaging. Nat Med 2007;13(1):95-99.

7. Couraud S, Planus C, Rioufol C, Mornex F. [Platinum salts hypersensitivity]. Rev Pneumol Clin 2008;64(1):20-26.

8. Cristaudo A, Sera F, Severino V, De Rocco M, Di Lella E, Picardo M. Occupational hypersensitivity to metal salts, including platinum, in the secondary industry. Allergy 2005;60(2):159-164.

9. Touraine F, Sainte Laudy J, Boumediene A, Ndikumwenayo F, Decroisette C, Melloni B, Vergnenegre A, Bonnaud F. [Investigation of allergic reactions to platinum salts]. Rev Mal Respir 2006;23(5 Pt 1):458-462.

10. Chang SS, O'Keefe DS, Bacich DJ, Reuter VE, Heston WD, Gaudin PB. Prostate-specific membrane antigen is produced in tumor-associated neovasculature. Clin Cancer Res 1999;5(10):2674-2681.

11. Sardana G, Dowell B, Diamandis EP. Emerging biomarkers for the diagnosis and prognosis of prostate cancer. Clin Chem 2008;54(12):1951-1960.

www.manaraa.com

12. Sobel RE, Sadar MD. Cell lines used in prostate cancer research: a compendium of old and new lines--part 1. J Urol 2005;173(2):342-359.

13. Sobel RE, Sadar MD. Cell lines used in prostate cancer research: a compendium of old and new lines--part 2. J Urol 2005;173(2):360-372.

www.manaraa.com